Topological Insulator-Superconductor Heterostructures and Devices

by

Lin Li

A thesis
presented to the University of Waterloo
in fulfillment of the
thesis requirement for the degree of
Doctor of Philosophy
in
Electrical & Computer Engineering
(Nanotechnology)

Waterloo, Ontario, Canada, 2019

AUTHOR'S DECLARATION

I hereby declare that I am the sole author of this thesis. This is a true copy of the thesis, including any required final revisions, as accepted by my examiners.

I understand that my thesis may be made electronically available to the public.

Abstract

A 3D topological insulator has fully gapped insulating bulk state but a conducting surface. Such conducting "surface" states are formed with helical Dirac fermions, with spin-momentum strictly locked by spin-orbital coupling. When coupled to a conventional *s*-wave superconductor, the surface state behaves just like the desired *p*-wave superconductor. It has been predicted that Majorana zero-modes obeying non-Abelian statistics can appear in such a system. Braiding operations on the Majorana zero-modes can realize topological quantum computing that is innately error-tolerant. Therefore, it has boosted extensive interest in the topological insulator-superconductor (TI-S) heterostructures. High quality TI-S heterostructures on wafer size scale is demanded for both fundamental studies as well as applications in the future.

The study in this thesis explored molecular beam epitaxy (MBE) growth of TI-S bilayer heterostructures by depositing 3D topological insulator $(Bi_{1-x}Sb_x)_2Te_3$ (BST) on superconductors including Nb and MgB_2. The BST-Nb heterostructure has been demonstrated to have high crystalline quality and clear interface. BST-MgB_2 heterostructure suffers from chemical reaction happening at its interface, which can be inhibited by lowering growth temperature and prevented by inserting a thin layer of Nb in between to form BST-Nb/MgB_2 structure.

In addition, by depositing a top layer of Nb on the bilayer heterostructures and proceeding to fabrication, we achieved vertical S-TI-S junctions that have seldomly been studied. Josephson coupling between the two superconducting electrodes and between proximity induced superconducting TI surfaces was observed on the Nb-BST-Nb and Nb-BST-Nb/MgB_2 junctions, giving two different critical current transitions on the I-V characteristics. In the Nb-BST-MgB_2 junction, tunneling effect through normal electrons was dominating without Josephson current being observed, which is due to an insulating layer formed at the BST-MgB_2 interface. Despite the difference in overall conductance features, a zero bias conductance peak (ZBCP) was observed on the dI/dV-V curves from all three kinds of junction. The origin of this ZBCP was discussed.

The thin film heterostructures obtained in this project can be good platforms to search for Majorana zero-modes through various approaches. We have also demonstrated the heterostructures are compatible with fabrication processes by patterning vertical junctions. Transport measurement results on these junctions could provide some insight into understanding the physical processes happening at the TI-S interfaces.

Acknowledgements

First and foremost, I would like to acknowledge my supervisor Professor Guo-Xing Miao, who provided me continuous support during these years. His friendly guidance and immense knowledge helped me throughout all stages of my PhD study. I also want to thank Professor Bo Cui for being my co-supervisor, who has been supportive and enthusiastic about my projects. I also thank Professors Dayan Ban, Jonathan Baugh, Zbigniew Wasilewski and Ke He for their time and interest to serve on my thesis committee.

Besides, I would like to take this chance to thank all my collaborators on this project. I want to mention Dr. Hui Zhang, who helped me through the early stage of my research career especially the training of experimental skills. He is always generous to share his experiences and ideas. I also need to acknowledge Xiaodong Ma who collaborated on the growth of topological insulators, Dr. Long Cheng for his help on device fabrications and measurements. I want to thank Dr. Deler Langenberg for his assistance on Omicron deposition system, Dr. George Nichols, Dr. Sangil Kwon and Peter Sprenger for assisting me on the low temperature systems. It is also a pleasure to thank Dr. Brian Goddard, Dr. Nathan Nelson Fitz-Patrick, and all the rest of the QNC NanoFab team for their training and assistance with fabrication.

Furthermore, I am grateful to many past and present students in this research group and the Institute for Quantum Computing which has a highly motivated and intellectual environment.

Last but not the least, I would express my gratefulness to my family. Special thanks to my husband Dr. Dongsheng Wang, who strongly supported me towards completion of the project. As a researcher, he is often able to provide me valuable suggestions when I had questions. I also would like to thank my parents for their understanding and support during these years of my PhD study. Thank my little one Niels for bringing endless inspirations into my life.

Table of Contents

List of Figures

Chapter1
Introduction

1.1 Introduction

Devices and materials with nontrivial topological features have been a popular research field in recent years. One of the seminal examples in the early days is the quantum Hall (QH) effect observed in 2D electron degenerate gas (2DEG) system in strong magnetic field [1], which shows insulating bulk but conducting edge states. About two decades later, people found an extension of QH state that does not require external magnetic field and instead, preserves the time-reversal (TR) symmetry, which is the famous quantum spin Hall (QSH) insulator, or 2D topological insulator (TI) [2-4]. Soon after that came out the theoretical predictions for 3D TI, which has been demonstrated by subsequent experimental observations. Since its discovery, TI has become an emerging field with profound impact and applications.

The unique feature of a TI is its conducting edge or surface state, which is supported by the topology of its bulk state according to the bulk-boundary correspondence. Experimental signatures of surface states of 3D TIs have been confirmed by the angle-resolved photoemission spectroscopy (ARPES) [5]. Furthermore, people soon realized that the surface states can bring exotic physics when TI is combined with magnetic or superconducting materials. For example, through doping with magnetic impurities or in proximity to magnetic layers, the conducting surface state of 3D TI can be gapped out, leading to quantum anomalous hall (QAH) effect [6] that has promising applications for non-dissipative electronics. Meanwhile, proximity effects on TI surfaces with *s*-wave superconductors have been shown to support the famous Majorana fermions [7, 8].

A Majorana fermion is a hypothetical particle that is identical to its own antiparticle, first suggested by Ettore Majorana in 1937. Mathematically this rule can be expressed in terms of the creation and annihilation operators as $\gamma^\dagger = \gamma$, where the creation operator ($\gamma^\dagger$) creates a Majorana fermion while the annihilation operator (γ) annihilates it. A Majorana fermion can be seen as half of the ordinary Dirac fermion in the sense that the Dirac operator (c) is expressed as $c = \frac{1}{2} (\gamma_1^\dagger + i\, \gamma_2)$. Along with the search for Majorana fermions in elementary particle physics, Majorana zero-mode, which follows the Majorana equation that describes Majorana fermions, has been predicted to emerge as a novel

excitation in some condensed matter systems. The localized Majorana zero-mode at a defect or a boundary is no longer a fermion as it obeys non-Abelian statistics and are useful for topological quantum computation [9, 10].

Superconducting system is a natural place to search for such Majorana zero-mode since a superconductor imposes particle-hole symmetry so that the quasiparticle creation operator $\gamma^{\dagger}(E)$ at energy E is equal to the annihilation operator γ (-E) at energy -E. The zero-energy (E = 0) state would manifest the Majorana equation. These Majorana zero-modes can be trapped at the ends of 1D *p*-wave superconductors or inside vortex cores of 2D *p*-wave superconductors. However, intrinsic *p*-wave superconductors are rare to come by and fragile in thin film formats due to broken time-reversal-symmetry in the pairing and are unlikely to be useful in practical devices. In 2008, The groundbreaking proposal by Fu and Kane brought the possibility to simulate 2D *p*-wave superconductors through proximity effect between a 3D TI and a conventional *s*-wave superconductor (S) and hence boosted the study on TI-S heterostructures from both theoretical and experimental sides.

Existence of Majorana zero-modes in the TI-S heterostructure can be observed as a zero bias conductance peak (ZBCP) in the tunneling spectroscopy to a magnetic vortex core [11-13]. It can also be signaled by a 4π periodic current-phase relation in an S-TI-S Josephson junction [14-17]. In either way the study would call for high quality TI-S heterostructures in experiments. At current stage, most TI-S heterostructures were built using TI flakes, which sets a limit on the scalability and flexibility for fabrication. The study in this thesis aims at growth of wafer size scale TI-S multilayer thin films with high quality interface. TI films with optimized stoichiometry have been grown on two different superconductors, one being Nb which is more stable and the other being MgB_2 which has higher superconducting transition temperature (T_c) [18, 19]. These thin film heterostructures are ready to be studied by different techniques such as scanning tunneling microscope (STM) or ARPES to look for the expected exotic physics. They can also be patterned into S-TI-S Josephson junctions in different ways to meet different needs. Based on the thin films, we further fabricated the rarely studied vertical S-TI-S Josephson junctions and performed transport measurements. Our experimental findings could provide some insight for understanding physical processes happening at the TI-S interfaces.

1.2 Thesis outline

The chapters of this thesis are organized as follows:

Chapter 2 briefly reviews the theoretical background to understand topological properties of materials. This includes topological insulators and topological superconductors. Afterwards, the proximity effect between TI and superconductor will be introduced.

Chapter 3 describes experimental techniques that are used in the study of this thesis, including growth and characterization tools. Molecular beam epitaxy (MBE) is employed as the main growth method. As one of the most important real time characterization techniques during MBE growth, reflection high energy electron diffraction (RHEED) will be explained. Fabrication process for the vertical junctions will also be shown in this chapter.

Chapter 4 starts from introducing the material property of the $(Bi_{1-x}Sb_x)_2Te_3$ (BST), which is a 3D TI, and shows the optimized growth results of BST film on different substrates by MBE. Both crystal and electrical transport properties of the BST films will be presented. The growth of BST-Nb and BST-EuS heterostructures will also be shown in this chapter.

Chapter 5 focuses on the Nb-BST-Nb vertical Josephson junctions, which are fabricated based on the heterostructures introduced in chapter 4. Transport measurement results will be presented and discussed. To understand the transport property of such junction, brief introduction to the processes related with the superconducting interfaces including Andreev reflection and Andreev bound states will be explained.

Chapter 6 presents the MBE growth of MgB_2 thin film, which is a superconductor with $T_c \sim 39K$. This higher T_c makes it promising to be combined with the BST film. Before moving on to BST-MgB_2 heterostructure, in this chapter we will focus on optimizing the growth condition of MgB_2 thin films. High quality MgB_2-MgO-MgB_2 heterostructures are also obtained and fabricated into Josephson junctions. General knowledge about Josephson effect will be reviewed when we discuss the MgB_2-MgO-MgB_2 Josephson junctions. An MgB_2-EuS heterostructure will also be presented in this chapter.

Chapter 7 focuses on the BST-MgB_2 heterostructure, which is more challenging than all other structures due to chemically active interface. The growth methods and characterization results will be

presented. Vertical Nb-BST-MgB_2 Josephson junctions are fabricated and measured. Comparison of their behavior with the Nb-BST-Nb junction will be discussed.

Chapter 8 summarizes the research achievements presented in the entire thesis.

Chapter 2
Background

2.1 Topological invariant and bulk boundary correspondence

The concept of topological invariant was first employed by mathematicians to classify different geometrical objects. Gauss-Bonnet theorem states that the integral of the Gaussian curvature over a closed surface is a quantized topological invariant, whose value is related to the genus g of the surface [32]. For example, g counts the number of holes on 2D surfaces. The surface of a sphere has no hole ($g = 0$) while the surface of a torus has one hole inside ($g = 1$), thus a sphere and a torus belong to different topological classes. All objects with the same g are topologically equivalent to each other regardless of other details and can be smoothly deformed into each other. However, an object cannot be smoothly deformed into a different topological class without breaking itself. For example, we cannot continuously deform a sphere into a torus unless we punch a hole on the surface and reconnect it.

When it comes to condensed matter system, one can also define such an invariant to topologically classify the electronic states. The integer Chern invariant (Ch) was introduced by Thouless, Kohmoto, Nightingale and Nijs (TKNN) in 1982 [20] to describe the topology of quantum Hall state [1]. Additionally, a Z_2 topological invariant (ν) can be used to characterize the quantum spin hall insulator or 2D topological insulator (TI), which was discovered in 2005 [2, 21], and then extended to 3D TI [22]. These quantized topological invariants can be expressed physically in terms of the Berry phase associated with the Bloch wave function. From the view point of topology, all conventional insulators, semiconductors as well as vacuum belong to the same class ($Ch = 0$) that is topologically trivial. They are equivalent to each other in the sense that one can change their energy gaps continuously by tuning the Hamiltonian without closing the gap. Although also being gapped systems, the quantum Hall state and 2D & 3D topological insulators belong to different topological classes. Their band structures cannot be continuously deformed into each other unless a gapless state is introduced at their boundary. *Bulk boundary correspondence* summarizes the unifying feature of such gapped systems: a gapless mode exists at the boundary where the topological structure of the bulk state changes. Specifically, the conducting surface states of topological insulators as well as the

Majorana edge modes of topological superconductors, which we will discuss later, manifest the bulk-boundary correspondence.

2.2 Topological insulators (TI)

In this section, we will review the insulating states with non-trivial topology and look at their exotic edge states.

2.2.1 Quantum Hall state

The integer quantum Hall (QH) state was observed in two dimensional electron system placed in strong perpendicular magnetic field $\mathbf{B} = B\hat{z}$ at low temperature [1], when the Hall conductance σ_{xy} took quantized values

$$\sigma_{xy} = Ne^2/h$$

where N is an integer and h is the Planck's constant. This phenomenon is caused by quantization of electrons' circular orbits in the magnetic field into Landau levels with energies $E_n = \left(n + \frac{1}{2}\right) h\omega_c/2\pi$, where $\omega_c = eB/m_e c$. At low temperature and when magnetic field $\mathbf{B}$ is strong enough, Fermi level can sit in between the discrete Landau levels so that N Landau levels are filled and the rest are empty, leading to a bulk insulating state. But different from an ordinary insulator, there is a conducting channel existing on the edge, giving rise to the quantized Hall conductance. This channel can be understood as electrons doing skipping motion when their cyclotron orbits bounce off the edge, and the motion is *chiral* in the sense that electrons can only propagate in one direction along the edge, shown in Figure 2-1.

A topological description of the QH state was first introduced by D. J. Thouless, M. Kohmoto, M. P. Nightingale, and M. den Nijs [20], who characterized the system with a topological number, known as TKNN integer. Then Kohmoto [23] derived the TKNN integer in the form of the Chern number Ch, which is an integral of the Berry flux performed on the 2D Brillouin zone. The total Chern number summed over all occupied bands is an invariant and is identical to the filling number N. A vanishing Ch usually represents a topologically trivial system. Time reversal symmetry breaking is required for a nonzero Ch, which is just the case in the QH state. For a system with time reversal symmetry, the calculation would require $Ch = -Ch$, leading to $Ch = 0$. This is the case for an

ordinary insulator or vacuum. At the boundary between a topologically trivial region (vacuum) and non-trivial region (QH system), the *Ch* must undergo a change. The conducting edge state of the QH state is a consequence of such change in topology, where the gap has to close.

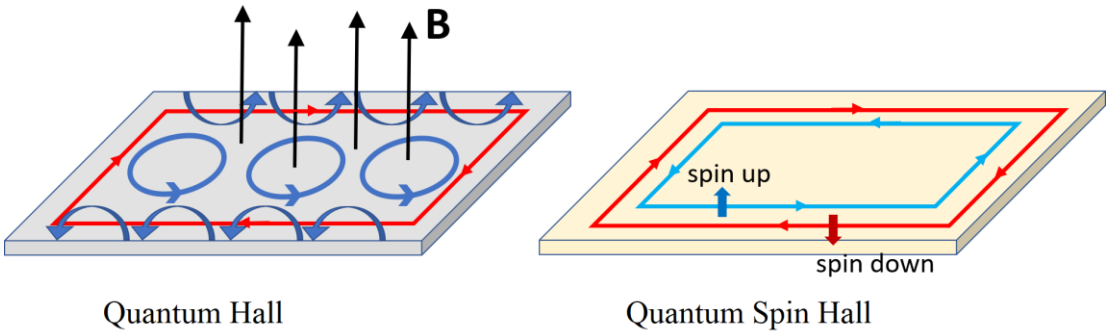

Figure 2-1: Illustration of the *chiral* edge channel in QH system (left) and *helical* edge channels in QSH system (right). The edge channels are indicated by red and blue arrowed lines. The arrowed circles represent orbitals of electrons doing cyclotron motion in magnetic field **B**.

2.2.2 2D TI - quantum spin Hall state

The 2D topological insulator, or quantum spin Hall (QSH) state, can be viewed as two copies of QH states. Different from the chiral edge channel of QH state which propagates in one direction only, the edge channels of QSH state are helical [2] where electrons with opposite spin counter propagate, see Figure 2-1. The two edge channels form a Kramers' pair as a result of time reversal symmetry. The QSH state was first proposed in the HgTe/CdTe quantum wells by Bernevig-Hughes-Zhang [3] and experimentally confirmed by König et al in 2007 [24]. Driven by strong spin-orbital coupling, the quantum well system will go through topological phase transition at a critical thickness $d_c = 6.3$ nm. When the thickness of HgTe layer is $d < d_c$, the 2D electron states bound in the quantum well have normal band structure similar to other semiconductors, i.e., it is a conventional insulator. For $d > d_c$, the 2D bands invert and the system becomes a QSH insulator with a pair of helical edge states. Each set of states associated with the top and bottom edge contributes a quantized conductance e^2/h and the quantum well exhibits a total conductance $2e^2/h$.

The QSH insulator does not break time reversal symmetry so the *Ch* invariant in this system is 0. However, there is an additional topological invariant ν with two possible values ν = 0 or 1 (referred as Z_2 invariant) that is used to characterize the topological property of QSH states. Constructing the Z_2 invariant is generally a difficult problem and there are several approaches explored in literature [25-31]. Here we are not giving a mathematical formulation for it but introduce an easy way to distinguish the topological features following Hasan and Kane [6]. As shown in Figure 2-2, if there are electronic states bound to the edge of a 2D insulator, Kramers' theorem requires them to be twofold degenerate at the time reversal invariant points $k_x = 0$ and π/a, labeled as Γ_a and Γ_b. Away from these points, spin-orbital coupling lifts the degeneracy. The way that the states at Γ_a and Γ_b connect determines how many times the Fermi level will cross the edge states. Figure 2-2 (a) and (b) shows the two possibilities. In case of Figure 2-2 (a), the crossing number is even; as a result, the edge states can be eliminated by continuously pushing the bound states out of gap. Oppositely, an odd number of crossing indicates a topologically nontrivial case, as shown in Figure 2-2 (b), in which there is no way to eliminate the edge states. The number of crossings N is related to the change in the Z_2 invariant v across the interface by bulk boundary correspondence, $N = \Delta v \bmod 2$.

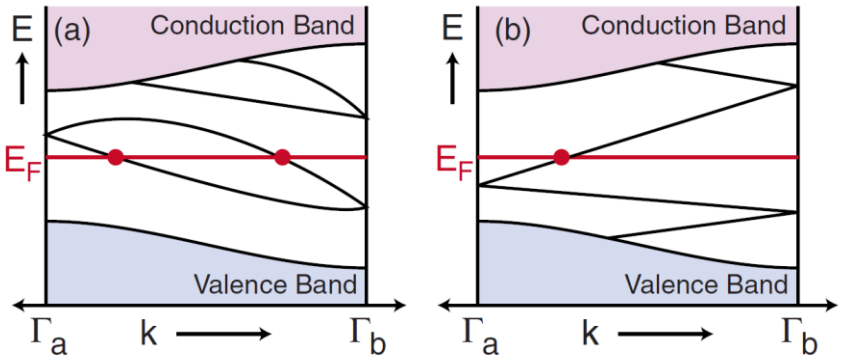

Figure 2-2: Dispersion of electronic states associated with the edges in a 2D insulator with two Kramers' degenerate points $\Gamma_a = 0$ and $\Gamma_b = \pi/a$ [32]. The number of crossings between these edge states and the Fermi energy E_F is even in (a), and is odd in (b).

2.2.3 3D TI

The above consideration can be generalized to 3D TI, which is characterized by four Z_2 invariants (ν_0; ν_1 ν_2 ν_3) [33-35]. The surface states of a 3D crystal have 2D Brillouin zone, where there are four time-reversal invariant points requiring the surface bands to be Kramers' degenerate. These degenerate points are referred as Dirac points. $\nu_0 = 1$ identifies a class of strong 3D topological insulators, whose surface Fermi circle encloses an odd number of Dirac points. For the simplest case, there is a single Dirac point at $k_x = 0$, $k_y = 0$, as shown in Figure 2-3. The electronic structure of the surface states is *helical.* In other words, the spin $\vec{s}$ and momentum $\vec{k}$ of an electron are locked together so that if an electron with $+\vec{k}$ on the Fermi level is spin-up, the one with $-\vec{k}$ must be spin-down. This spin helical feature is also shown in Figure 2-3.

The semiconducting alloy Bi_xSb_{1-x} was the first 3D topological insulator experimentally demonstrated by angle-resolved photoemission spectroscopy (ARPES) in 2008 by the group of Hasan [36]. However, its surface states are extremely complex, with at least five dispersion branches [37]. Later in 2009, a simpler surface spectrum with single Dirac cone was first observed by ARPES in Bi_2Se_3 [38]. At the same time, theoretical work based on *Ab initial* calculations showed that the family of stoichiometric crystals Bi_2Se_3, Bi_2Te_3 and Sb_2Te_3 are all 3D topological insulators having robust and simple surface states with a single Dirac cone at the Γ point [37]. In these materials, there is a band inversion transition at the Γ point driven by spin-orbit coupling (SOC), making the band gap to be topologically non-trivial and introducing a conducting surface state. Following the theoretical prediction, more experiments through ARPES confirmed the existence of the surface state with a Dirac cone in Bi_2Se_3 [37, 39], Bi_2Te_3 [27, 40] and Sb_2Te_3 [41]. Among them, spin-resolved ARPES results [42, 43] further demonstrated the helical spin texture on the Dirac cone.

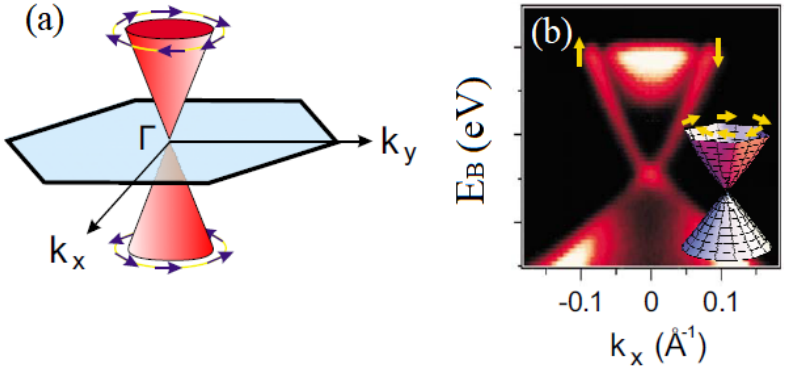

Figure 2-3: (a) Spin-momentum locked helical surface Dirac cone of a 3D TI. The arrows indicate spin directions. (b) A high resolution ARPES mapping of the topological surface state near the Dirac point of $Bi_{2-x}Ca_xSe_3$ with x = 0.01 [42].

In addition to the unique properties of the gapless surface state, there are some interesting new effects related to opening a gap on the surfaces through several ways. One of them is through coupling between two surfaces. When the thickness of a film is reduced to only several nanometers, there will be overlapping between the wavefunctions from the two surfaces, which can open a gap. The thickness dependence of the topological insulators has been studied [44, 45]. Furthermore, by breaking the time reversal symmetry through a magnetic field, magnetic doping or proximity to magnetic materials, an exchange gap can be opened at the Dirac point, leading to quantum anomalous Hall (QAH) state [6]. Alternatively, a superconducting energy gap can also be induced into the surface states through proximity to a superconductor (S), which mimics a topological superconductor, providing a platform to search for Majorana zero-modes [7]. Thus the proximity effect between TI and S has been an important topic in recent years [11-13, 46-53] and serves as the motivation for this thesis. In the following sections we are going to introduce the concept of topological superconductor and Majorana mode, then review how to artificially realize a topological superconductor through proximity effect on TI.

2.3 Topological superconductors and Majorana modes

In general, topological classification can be applied to all gapped systems. Considering that a superconducting gap corresponds to the band gap of an insulator, we can also topologically classify

superconductors. After discovery of topological insulators, the study was generalized to topological superconductors [54, 55]. Similarly, there exist gapless edge state at the boundary of a superconductor if it resides in the topologically non-trivial regime. The simplest models for a topological superconductor are established on spinless fermions in a 1D *p*-wave superconductor or a 2D chiral p_x+ip_y superconductor [56, 57]. Spinless fermion can be viewed as a spin polarized fermion, which is a toy model of the more complicated spinful case. We will briefly review the 1D case, where a pair of Majorana zero-modes can be localized at the two ends of a 1D spinless *p*-wave superconductor. Afterwards we will focus the discussion on a 2D chiral p_x+ip_y superconductor and show how to localize Majorana zero-modes in such system.

2.3.1 1D spinless *p*-wave superconductors and Majorana modes

A toy model for 1D spinless *p*-wave superconductor was introduced by Kitaev [58]. This model describes spinless fermions hopping on an N-site chain and exhibit long range ordered *p*-wave superconductivity. With operator c_j describing the fermion on *j*-site, the Hamiltonian is

$$H_{BdG} = \sum_j \left[-t\left(c_j^\dagger c_{j+1} + c_{j+1}^\dagger c_j\right) - \mu c_j^\dagger c_j + |\Delta|\left(c_{j+1}^\dagger c_j^\dagger + c_j c_{j+1}\right) \right]$$

where $t \geqslant 0$ is the nearest neighbor hopping strength, μ is the chemical potential, Δ is the *p*-wave pairing potential. Upon transforming to the momentum space, one can obtain the energy spectrum as

$$E_\pm(p) = \pm\sqrt{(2t\cos p + \mu)^2 + 4|\Delta|^2 \sin^2 p}$$

where *p* is momentum. For $|\Delta| \neq 0$, the energy gap vanishes at two critical points, one is $p = 0$ and $\mu_c = -2t$, the other is $p = \pi$ and $\mu_c = 2t$. The critical points separate the gapped superconducting phase into two regimes: (1) topological trivial phase when $\mu < -2t$ or $\mu > 2t$; (2) topological non-trivial phase when $|\mu| < 2t$. There are several ways that a topological invariant can be expressed to distinguish these two phases. Following [59], a Z_2 topological invariant is defined as

$$\nu = s_0 s_\pi$$

where s_0 and s_π represent the sign of the kinetic energy $\epsilon_p = (-2t\cos p - \mu)$ at $p = 0$ and π respectively. It is clear that $\nu = +1$ for the above case (1)-topological trivial phase and $\nu = -1$ for case (2)-topological non-trivial phase. The non-trivial topology will lead to a zero-energy Majorana mode residing at each end of the chain. To show this, we first rewrite the Hamiltonian using Majorana

representation, by replacing each c_j with two Majorana fermions γ_{2j-1} and γ_{2j} via $c_j = \frac{1}{2}(\gamma_{2j-1} + i\,\gamma_{2j})$, where the Majorana fermion operator γ_j satisfies

$$\gamma_j{}^{\dagger} = \gamma_j$$

This means the anti-particle of a Majorana fermion is itself. In this basis, the original Hamiltonian has the new form

$$H_{\mathrm{BdG}} = \frac{i}{2}\sum -\mu\gamma_{2j-1}\gamma_{2j} + (t + |\Delta|)\gamma_{2j}\gamma_{2j+1} + (-t + |\Delta|)\gamma_{2j-1}\gamma_{2j+2}$$

and the key difference between the topological trivial and non-trivial phases can be seen by looking at two simplifying limits.

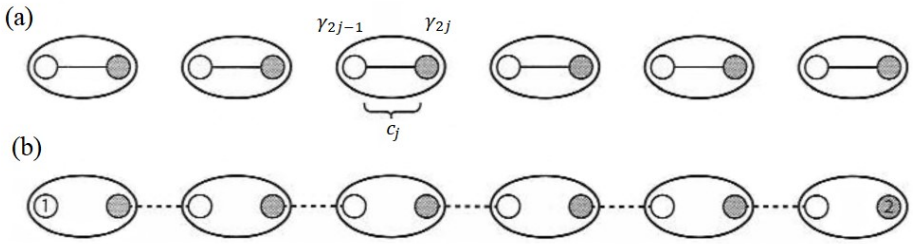

Figure 2-4: Schematic illustration of the Kitaev's chain model describing spinless fermions hopping on the lattice. The oval represents a physical site while the empty and filled circles represent the Majorana fermions occupying each site. Solid and dashed lines represent coupling between a pair of Majorana fermions. (a) In the trivial limit, the Majorana operators on each site are coupled to form a Dirac fermion and (b) In the nontrivial limit, there are two unpaired Majorana fermions left at the two ends of the chain, labeled as 1 and 2. [60]

(1) For the trivial phase, we choose $|\Delta| = t = 0$ and $\mu < 0$. Then the Hamiltonian reduces to

$$H = -\mu\frac{i}{2}\sum\gamma_{2j-1}\gamma_{2j}$$

In this case, the Majorana operators on each site are coupled, and Majorana operators between each site are decoupled, as illustrated in Figure 2-4 (a). This is just the atomic limit that one ordinary fermion occupies each physical site.

(2) For the topological non-trivial phase, we choose $|\Delta| = t > 0$ and $\mu = 0$, and the Hamiltonian will reduce to

$$H = i\,t \sum \gamma_{2j}\gamma_{2j+1}$$

In this case, the Majorana operators are paired in the way shown in Figure 2-4 (b), where γ_1 and γ_N are left unpaired with open boundary condition. We see two Majorana zero-modes are localized at the ends of the chain.

For the more general case where $|\Delta| \neq t$ and $\mu \neq 0$ but still within the topological non-trivial phase, there will be mixture of couplings between Majorana operators on the same sites and between different sites. However, as the Majorana zero-modes are localized at the ends of the chain, the coupling between them is exponentially small with respect to the length of the chain. These modes will not be destroyed unless the bulk gap closes. In other words, they are protected by the topology of the bulk.

2.3.2 2D spinless *p*-wave superconductors and Majorana modes

In two dimensions, the simplest system for a topological superconducting phase is based on the spinless p_x+ip_y fermions [57]. At a vortex core it holds Majorana zero-modes [61], which obeys non-Abelian statistics [57, 62] suitable for topological quantum computing [9]. To show that, we will go through the following analysis.

After generalizing the 1D lattice Hamiltonian into the case for 2D spinless p_x+ip_y fermions, in continuum limit, the energy spectrum can be solved as

$$E_{\pm}(p) = \pm\sqrt{(\frac{p^2}{2m}-\mu)^2 + 4|\Delta|^2 p^2}$$

where $p^2 = p_x^2 + p_y^2$ [59, 60]. With finite Δ, the spectrum is fully gapped for any $\mu \neq 0$. Similar to the 1D *p*-wave case, the gapped phases for $\mu > 0$ and $\mu < 0$ belong to different topological regimes. The topological invariant to distinguish them is in the form of Chern number *Ch* [63]. The topological trivial phase $\mu < 0$ has a vanishing *Ch*, while the non-trivial phase $\mu > 0$ has $Ch = -1$. At the boundary between them, there are chiral edge states with opposite propagation direction which are identified as chiral Majorana modes.

To understand the physical picture, we shall consider a spinless p_x+ip_y superconductor with annulus geometry having inner and outer edges at r = $R_{in/out}$, as shown in Figure 2-5. It is in the topological phase for R_{in} < r < R_{out}, and in the trivial phase elsewhere. The energies for the bound states at two edges are $E_{out} = \frac{n\Delta}{R_{out}}$ and $E_{in} = -\frac{n\Delta}{R_{in}}$, where n is a half-integer to ensure the anti-periodic condition which is essential for the p_x+ip_y superconductor [59]. Therefore, there is no state at zero energy for this case. However, when a magnetic flux quantum $\Phi = hc/2e$ is inserted through the hole, the boundary condition will be shifted to periodic, changing n to an integer number. As a result, we can get two modes with exact zero energy located at the inner and outer edges, which correspond to the pair of end modes in 1D p-wave wire. For a spinless p_x+ip_y superconductor with two holes in Figure 2-5 (e), the two inner boundaries exhibit periodic condition and thus hold two zero Majorana modes, while the outer edge recovers the anti-periodic condition and has bound states with finite energies. One can also solve the Hamiltonian in a cylindrical symmetry which will yield two zero-modes on the two boundaries of a cylinder [60].

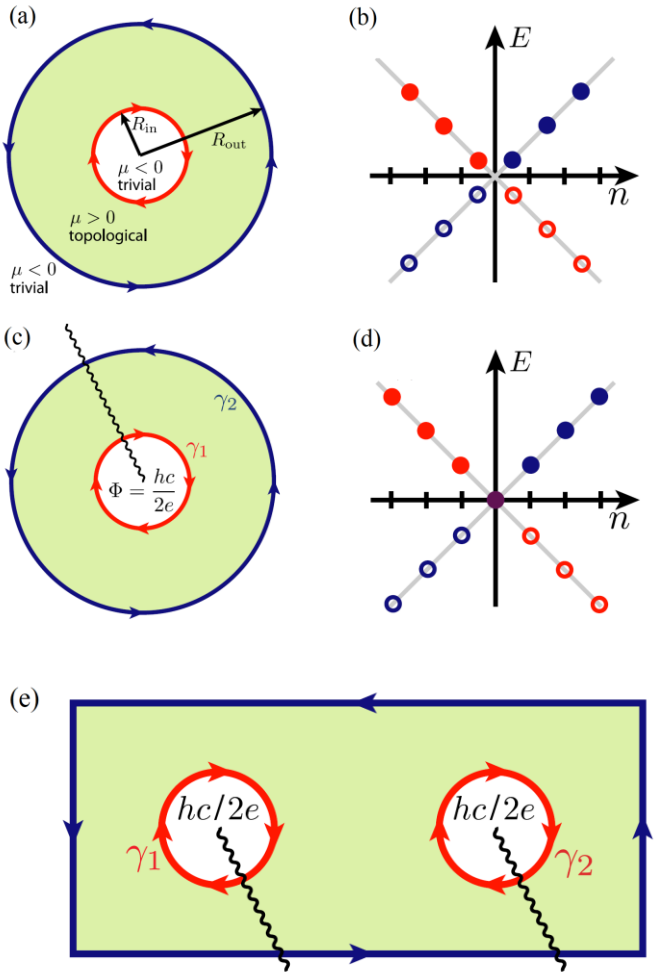

Figure 2-5: (a) A topological p_x+ip_y superconductor with annulus geometry supports chiral Majorana edge modes at its inner and outer boundaries. (b) Energy spectrum of the edge modes versus n for the inner (red circles) and outer (blue circles) edge, where n is a half-integer. (c) An $hc/2e$ flux through the center introduces a branch cut (wavy line) which, when crossed, leads to a sign change for the Majorana edge modes. The flux induces periodic boundary conditions and shifts n to integer values. This leads to the spectrum in (d), which includes Majorana zero-modes γ_1 and γ_2 localized at the inner and outer edges. (e) The two-vortex setup supports one Majorana zero-mode localized around each vortex while the outer edge remains gapped. [59]

The annulus picture can also be modulated in a vortex core when a magnetic flux threading the bulk of a 2D spinless p_x+ip_y superconductor. The vortex core with a size on the order of coherence length $\xi \sim v_F/(k_F\Delta)$ can be seen as a trivial gapped region with discrete quantized energies due to small size. The energies of the Majorana modes bound to the vortex are given by

$$|E_{vortex}| \sim \frac{|n|\Delta}{\xi} \sim \frac{|n|(k_F\Delta)^2}{E_F}$$

where n is an integer [59]. There is a zero-energy mode bound to the vortex, which is separated from the next excited state by $(k_F\Delta)^2/E_F$.

One import nature of the Majorana zero-modes is that they obey non-Abelian statistics: for a system with N Majorana zero-modes, if one exchanges them sequentially, the final state will depend on the order in which the exchanges are carried out [62, 64]. The exchange operation can be realized through braiding Majorana-carrying vortices in 2D or fusing and creating the end modes in 1D network [64]. The non-Abelian statistics of Majorana zero-modes enables them to be applied in quantum computation in the way that quantum information can be non-locally encoded hence avoids decoherence [9].

Although there exist candidates for intrinsic p-wave superconductivity such as Sr_2RuO_4 [65-68], $Cu_xBi_2Se_3$ [69-72] and UPt_3 [73-77], the pairing symmetry in these materials is still under debate. Furthermore, the p-wave pairing symmetry is fragile to any non-magnetic impurities. Thus, it is a challenging task to realize the 2D topological superconductor "intrinsically". Alternatively, Fu and Kane [78] proposed a way to artificially modulate this model through superconducting proximity effect on the 2D surface state of a 3D topological insulator, which will be introduced in next section.

2.3.3 Engineering a 2D *p*-wave superconductor using 3D TI and *s*-wave superconductor

Fu and Kane showed that one can obtain a Hamiltonian equivalent to a spinless p_x+ip_y superconductor when the surface states of a 3D TI are in proximity to an s-wave superconductor. The Dirac surface states of TI are spin-momentum locked, which means the spin freedom is frozen out. This property makes it an ideal system to access "spinless" regime. By adding the s-wave pairing term to the surface Hamiltonian, the hybrid system can mimic the p_x+ip_y system. It falls into the topological

phase as long as the chemical potential μ resides in the bulk gap. Also note that different from the spinless p_x+ip_y superconductor, this hybrid system is time reversal invariant which protects the induced superconducting gap from non-magnetic impurities. One can break the time reversal symmetry to look for the Majorana states in this system.

One way to break time reversal symmetry is introducing a Zeeman field. For example, by proximity to magnetic material or doping TI with magnetic impurities, the Zeeman energy will open a trivial gap on the Dirac cone. It has been suggested that the interface between a (nontrivial) region with superconducting gap and a (trivial) region with magnetic gap can host 1D chiral Majorana edges states, as schematically shown in Figure 2-6 (a). This configuration has been realized in a heterostructure consisting Cr doped TI and Nb [79]. Another way is to introduce an *hc*/2*e* vortex core. Similar as in an intrinsic spinless p_x+ip_y superconductor, the vortex core in the hybrid system also host a zero-energy Majorana bound state, experimentally studied by [12, 13]. While one can always induce the vortex core by applying a perpendicular magnetic field, Fu and Kane also proposed an alternative scheme to engineer and manipulate Majorana states using 3 linear junctions of superconductors on the surface of a TI [7], shown in Figure 2-6 (b). If the phases of three superconductor islands meeting at a tri-junction are arranged such that $\phi_1 = \pi - \epsilon_1, \phi_2 = \pi - \epsilon_2$, a Majorana zero-mode is predicted to exist as long as $\epsilon_1\epsilon_2 < 0$. The phase diagram for existence of a Majorana zero-mode is shown in Figure 2-6 (c). When the phase difference falls in the shaded area, there will be a Majorana zero-mode at the junction. To the special limits, the case $\phi_1 = \pm 2\pi/3, \phi_2 = \pm 4\pi/3$ simulates the situation of a vortex. If the phases are changed, the zero-mode cannot disappear until the energy gap along one of the three linear junctions goes to zero. This occurs when the phase difference across the junction is π. Therefore, adjusting the phase difference in a line junction terminated by two tri-junctions allows Majorana zero-modes to be created, manipulated, and fused.

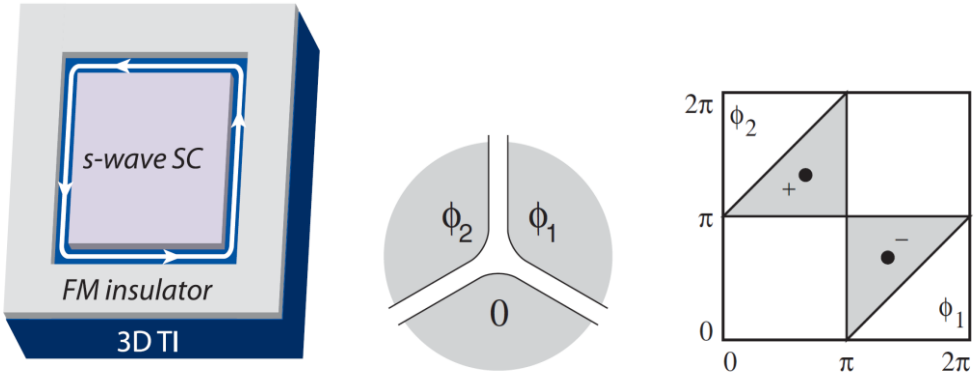

(a) (b) (c)

Figure 2-6: (a) 1D chiral Majorana formed on the surface of 3D TI at the boundary between a region with magnetic gap and a region with superconducting gap. [59] (b) A tri-junction of superconductors (shaded area) on the surface of a TI (c) Phase diagram of the tri-junction. When ϕ_1 and ϕ_2 reside in the shaded region, there will be a Majorana zero-mode localized at the tri-junction. [7]

2.4 Review of experimental studies on topological insulator-superconductor (TI-S) heterostructures

To realize Fu and Kane's proposal, one can combine TI and S to form heterostructures, which has been extensively studied in recent years. Several groups have succeeded in observing coexisting superconductivity and topological surface states in different kinds of heterostructures, such as Bi_2Se_3-$NbSe_2$ [80, 81], Bi_2Se_3-W [82], Bi_2Se_3-Sn [48], and Bi_2Se_3-$Bi_2Ca_2Cu_2O_{8+\delta}$ surfaces [83, 84]. More inspiringly, the signature of Majorana zero-mode in a vortex core has been reported as a zero bias conductance peak in the tunneling spectroscopy of Bi_2Se_3-$NbSe_2$ heterostructure by STM [12, 13]. The chiral Majorana edge modes were also detected as ½ e^2/h conductance edge current in Cr doped TI-Nb hybrid device [79].

In most of the work mentioned above, the topological insulator Bi_2Se_3 were used. Although Bi_2Se_3 has relatively large bulk gap (0.3 eV), it is easy to be doped with undesired bulk carriers due to Se vacancies, which will suppress the performance of surface states. On the other hand, either TI flakes were used or it was grown on flakes of superconductors. The *in situ* growth of TI-S heterostructure on the wafer size scale and in the meantime maintaining high quality of the interface will be preferred for

the sake of scalability in the future, however is still a challenge. In the following chapters of this thesis, we will show the achievements of MBE grown TI-superconductor heterostructures including $(Bi_{1-x}Sb_x)_2Te_3$-Nb and $(Bi_{1-x}Sb_x)_2Te_3$-MgB_2 on 2-inch whole wafers. In our study, the $(Bi_{1-x}Sb_x)_2Te_3$ compound was used as the topological insulator and we will show that it is bulk insulating by tuning the ratio between Bi and Sb. The wafer sized heterostructures provide more possibilities for device fabrication. Especially, the $(Bi_{1-x}Sb_x)_2Te_3$-MgB_2 could benefit from the large band gap and high transition temperature of MgB_2.

Chapter 3
Experimental methodology

The experimental part of this thesis focuses on two aspects. First, we optimized the molecular beam epitaxy growth conditions to achieve high quality thin films including $(Bi_{1-x}Sb_x)_2Te_3$ thin film, MgB_2 thin film and multilayer thin film heterostructures. Then we fabricated the heterostructures into micro-sized devices and conducted electrical transport measurements. In this chapter, we will introduce the experimental equipment and procedures used for thin film growth, characterization and device fabrication.

3.1 Molecular beam epitaxy (MBE)

MBE is considered to be the cleanest technique for growing crystalized thin films. It usually takes place in ultra high vacuum (UHV) with the pressure lower than 10^{-9} mbar, which significantly reduces surface contaminations. Molecular beams can be generated by the Knudsen effusion cells (K-cell) or electron beam evaporator. In UHV environment, the molecular beams will straightly reach the substrate without collisions and go through processes including adsorption, desorption, migration, diffusion and incorporation on the substrate before forming thin films. The beam fluxes can be precisely controlled by regulating the source temperature. Different elements have different absorption rate by the substrate, which also depends on the substrate temperature. Through fine tuning of the flux ratio and substrate temperature, it is convenient to get well controlled film composition. The typical growth rate is about 0.1~1 Å/s, allowing the films to grow epitaxially. The surface condition can be characterized *in situ* during growth by reflection high-energy electron diffraction (RHEED), which is an important tool in MBE.

3.2 Cluster deposition system

The thin films and heterostructures in this thesis were grown in an Omicron UHV cluster deposition system as shown in Figure 3-1. This is a complex thin film deposition system combining three MBE modules, two magnetron sputtering modules, and one surface analysis module. The system also contains a fast load-lock (FEL) chamber and a sample preparation chamber with Ar gun and RF Ar

plasma to clean sample surface. All chambers are interconnected through a linear transfer line. The vacuum in all growth and analysis modules is maintained under 10^{-10} mbar and in transfer line is under 10^{-9} mbar. MgB_2 and $(Bi_{1-x}Sb_x)_2Te_3$ films were grown in two different MBE chambers, and Nb thin film was grown in a magnetron sputtering chamber. In the case of heterostructure growth, after finishing one layer, sample can be transferred to another chamber under vacuum to grow next layer, which maintains the high quality of interface.

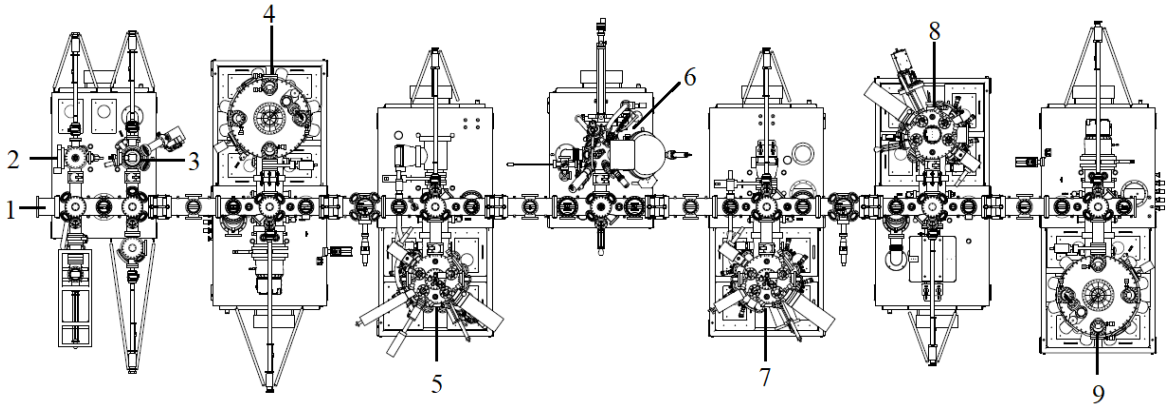

Figure 3-1: Configuration of the Omicron UHV cluster deposition system. (1) Vacuum transfer line (2) FEL (3) Sample preparation chamber (4) Magnetron sputtering module for superconductors, used to deposit Nb (5) MBE module for TI, used to grow $(Bi_{1-x}Sb_x)_2Te_3$ compound (6) Surface analysis module (7) MBE module for metal oxides (8) MBE and electron beam co-evaporation module, used to grow MgB_2 (9) Magnetron sputtering module for magnetic materials

3.2.1 MBE module for $(Bi_{1-x}Sb_x)_2Te_3$ growth

The MBE growth module dedicated for TI is used to grow $(Bi_{1-x}Sb_x)_2Te_3$ (BST) compound. The configuration of this chamber is shown schematically in Figure 3-2. This module is equipped with three K-cells and one valved cracker cell. High-purity Bi (99.999%) and Sb (99.999%) sources were evaporated by K-cells. There is one additional K-cell can be used to evaporate Cr, Mn or Gd, in order to introduce magnetic dopants into TI as needed. The valved cracker cell is used for Te. A mixture of large clusters of Te is first produced within the reservoir. Then the gaseous clusters are dissociated within the thermal cracker stage (1000 ºC) and broken into smaller molecules. The beam flux and

growth rate for each individual source is calibrated beforehand by the beam flux monitor (BFM) and quartz crystal monitor (QCM) respectively. Reflection high energy electron diffraction (RHEED) is used for real-time monitoring during growth. Sample can be heated through thermal radiation from a tungsten filament heater from the backside.

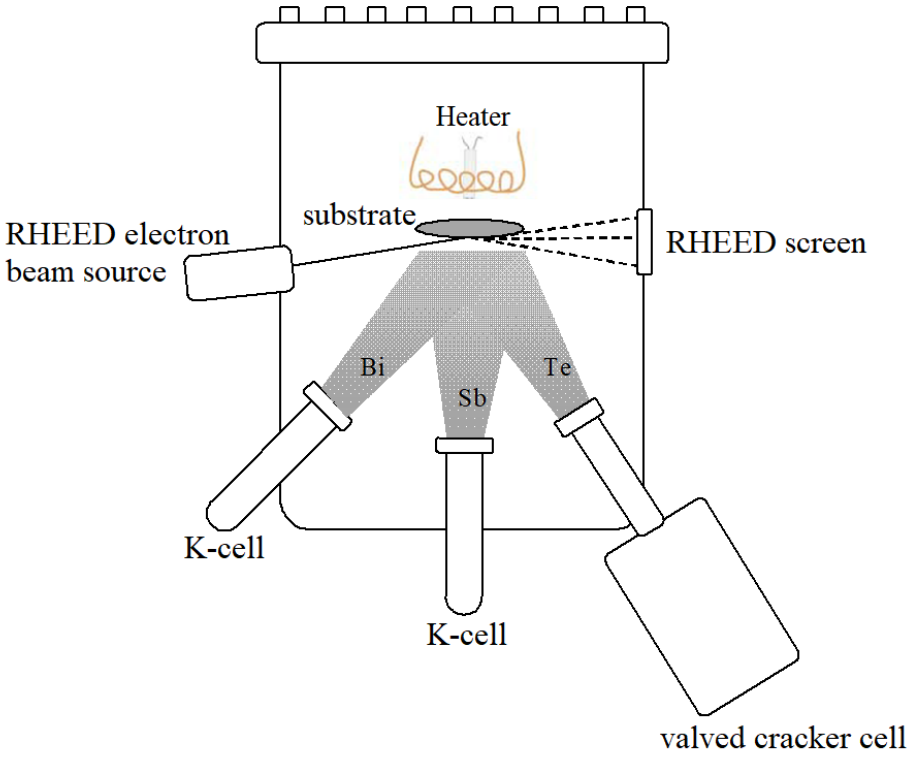

Figure 3-2: Schematic picture of the MBE module for $(Bi_{1-x}Sb_x)_2Te_3$ deposition.

3.2.2 MBE and electron beam co-evaporation module for MgB_2 growth

The module for MgB_2 growth is shown schematically in Figure 3-3. In addition to K-cells, QCMs and RHEED, this module is also equipped with an electron-beam evaporation source, which allows co-evaporation for MgB_2 with B coming from the e-beam source and Mg evaporated by the K-cell. The e-beam evaporation source contains six spots. In addition to B, it can also be used to evaporate other materials requiring high evaporation temperature. In this project, MgO, Al_2O_3, EuS and Au are loaded

for various purposes including growing barriers, capping layers and electrodes. Sample is heated by radiation from a noncontact SiC heater.

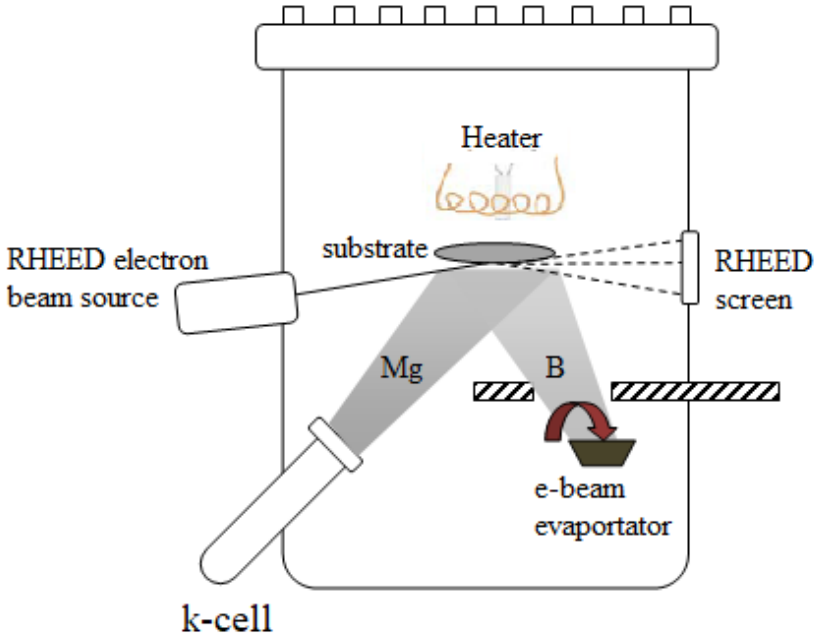

Figure 3-3: Schematic picture of MBE module for MgB_2 deposition.

3.3 Characterization tools

In this section, we will review the tools that are used to characterize thin films and heterostructures.

3.3.1 *In-situ*: RHEED

Each of our three MBE growth modules is equipped with a RHEED system to monitor the growth in real-time. The main parts of a RHEED system consist of an electron gun, a fluorescent screen and a CCD camera. High energy electrons (10 KeV~30 KeV) generated by the electron gun are incident into sample surface at a glancing angle (1º ~ 5º). Diffraction patterns are formed by the reflected electrons on the fluorescent screen and collected by the camera. Because of the small incident angle, electrons can only penetrate through 1 nm ~2 nm on the surface of sample, thus RHEED provides information about the surface instead of the bulk. Figure 3-4 illustrates the diffraction principle from

a 3D view. Similar to the analysis for diffraction from bulk crystals, the Ewald's sphere is constructed. However, instead of the reciprocal lattice for a 3D material, we will have reciprocal rods transformed from a 2D lattice sheet because only atoms at the sample surface contribute to the RHEED pattern. A constructive diffraction pattern will form wherever the reciprocal rods intersect the Ewald's sphere but the screen is setup so that only low orders of diffraction can be detected. By rotating the sample azimuthally, we can get full information about the 2D surface lattice.

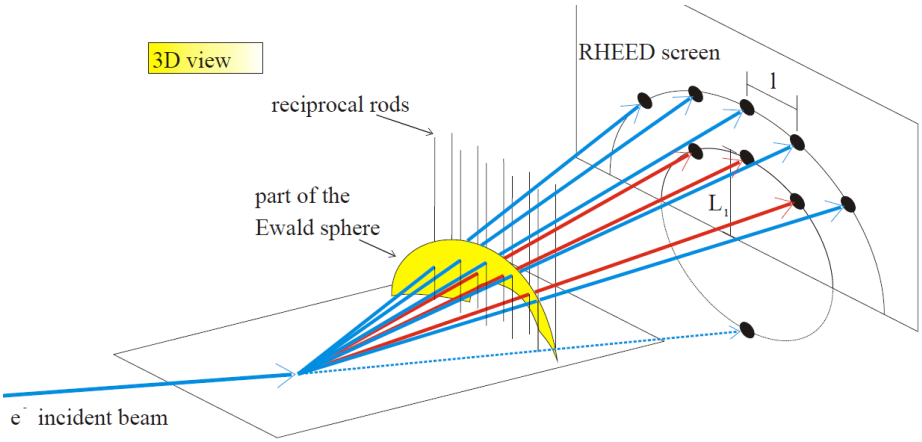

Figure 3-4: 3D illustration for RHEED, figure from [85].

To understand the qualitive information embedded in RHEED patterns, we discuss four kinds of typical RHEED patterns shown in Figure 3-5 (a). In the case of ideal 2D surface (a-1), the RHEED patterns are nice dots distributed on a series of Laue circles where the Ewald's sphere intersects the reciprocal planes. However, in real cases (a-2), we usually see streaky patterns for a qusi-2D sample surface. The steps or domains on the surface break the long-range order parallel to the surface and lead to finite 2D lattice size, thus the reciprocal rods will have certain thickness [86]. On the other hand, the radius of the Ewald's sphere is very large due to short electrons wavelength so that the low-order reciprocal rods are almost parallel to the sphere surface, and their intersections lead to elongated diffractions shown as streaks. In (a-3), a much rougher surface will show dotted RHEED patterns because electrons can transmit through the islands and form 3D diffraction patterns from the bulk. For a poly-crystal surface lattice, the RHEED patterns are a series of rings as shown in (a-4).

RHEED can be used to characterize the substrate surface condition before growth, to monitor the growth modes and signal us if the epitaxy collapses. In the case of layer-by-layer growth, the intensity

of RHEED signal depends on the coverage of atoms thus it oscillates as the film is growing. The oscillation can be used to characterize growth rate and film thickness. Figure 3-5 (b) illustrates one cycle of RHEED signal's oscillation in the formation of one single layer.

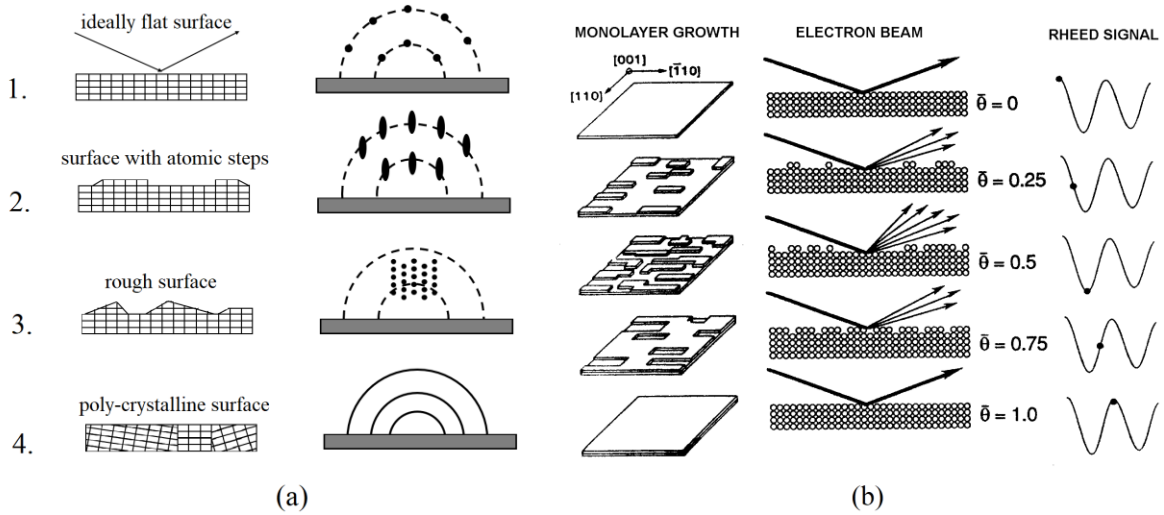

Figure 3-5: (a) Schematic illustration of RHEED patterns generated by different surface conditions. (b) RHEED signal oscillates as surface coverage changes.

3.3.2 *In situ*: XPS/AES/UPS

The surface analysis module connected to the growth system enables *in situ* post-growth analysis to be done without exposure to air. Equipped with X-ray source (Al - K_α 1486 eV and Mg - K_α 1253 eV), electron source (5000 eV) and ultraviolet photon source (21.4 eV), this chamber is able to do X-ray photoelectron spectroscopy (XPS), auger electron spectroscopy (AES) and ultraviolet photoelectron spectroscopy (UPS). There is also an Ar sputtering gun for depth profiling and a charge neutralizer used to neutralize charged surfaces.

XPS is useful to examine elemental composition of the surface and chemical or electronic state of each element on the surface. With the help of depth profiling, it can also be used to analyze the interface of heterostructures. AES can be used to determine electronic structure of the surface. UPS can be used to determine molecular orbital energies in the valence band and the work function in

solids. By rotating the sample in real space to get angle-resolved spectroscopy, UPS can also be an assistant tool to look at the Dirac point on the surface state of a TI film with limited resolution.

3.3.3 *Ex situ*: XRD

X-ray diffraction (XRD) is used to analyze the crystalline property of thin films and heterostructures. After the growth was fully accomplished and *in situ* characterizations were done, sample was taken out of vacuum for further analysis by a Bruker D8 Discover XRD system. The system consists of Cu X-ray source (λ = 1.54 Å), high resolution optics with a Ge 2-bounce monochromator and a centric Eulerian cradle with Chi/Phi rotations and X-Y-Z translations. θ-2θ scans were performed on all the films to examine their bulk crystallization and Φ scans were performed on epitaxial films. The system is also capable to do high-resolution XRD, grazing incidence diffraction and reflectometry for thickness calibration.

3.4 Fabrication

In addition to accomplishing the growth of different kinds of heterostructures, another aspect of this project involves fabricating them into vertical Josephson junctions. This section reviews the standard fabrication process using Nb-BST-Nb Josephson junction device as an example, which also applies to all other devices discussed in the following chapters of this thesis. The fabrication was conducted in the Quantum NanoFab and Characterization Facility (QNFCF) at the University of Waterloo.

Starting from multilayer thin film heterostructure with Au-Nb-BST-Nb grown on a 2-inch sapphire wafer, where the capping layer Au will be used as connecting electrodes in the final junctions, the sample is fabricated into micron-sized vertical Josephson junctions following standard photolithography and Ar ion milling techniques in three steps (Figure 3-6).

First, we defined the pattern of bottom electrodes which are isolated strips with two pads by photolithography. Shipley1811 photoresist was used as the photo-mask and MA6 mask aligner was used to define the pattern. Unprotected materials were removed by Ar ion milling with 90 º incidence. Secondary ion mass spectrometry (SIMS) was used during milling to monitor the time needed to finish etching each layer. The milling process was stopped after substrate was exposed. Then the photoresist was removed by acetone or PG remover.

Second, the junction areas were defined on the previously patterned strips. There are three junctions on each strip. The junction size varies from 1 μm to 8 μm. For junctions smaller than 4 μm, double layer resists of Shipley1805/PMGI can be used to improve resolution and lift-off yields. During the etching process of this step, because only a small amount of materials will be etched away, the SIMS signal is too weak to be read thus cannot be used in real time. However, with help of the information recorded by SIMS from the first step, etching can be stopped once BST was fully removed and bottom Nb was just exposed on wafer, thus in the unetched areas the top Nb and BST were left as three pillars standing on each bottom Nb strip. Another milling process at 0 º incident angle was performed to remove any side walls due to re-deposition. Afterwards, a passivation layer of SiO_2 was grown *in situ* by magnetron sputtering.

The last step was to define and grow top electrodes covering the junction areas. Photolithography defined three top strips with connection pads, forming cross geometry with bottom strips. Afterwards, Ti and Au were deposited as top electrodes. After the removal of photo-resist, the device was ready. Figure 3-7 (a) schematically illustrates the junction structure from a side view. An optical image of the device and illustration for electrical connection is shown in Figure 3-7 (b).

Figure 3-6: Illustration for fabrication process. The side views on left columns show detailed fabrication process step by step. During step 2, only one junction is shown while there are three junctions on the real device. The right column shows a top view of the pattern obtained at the end of each step.

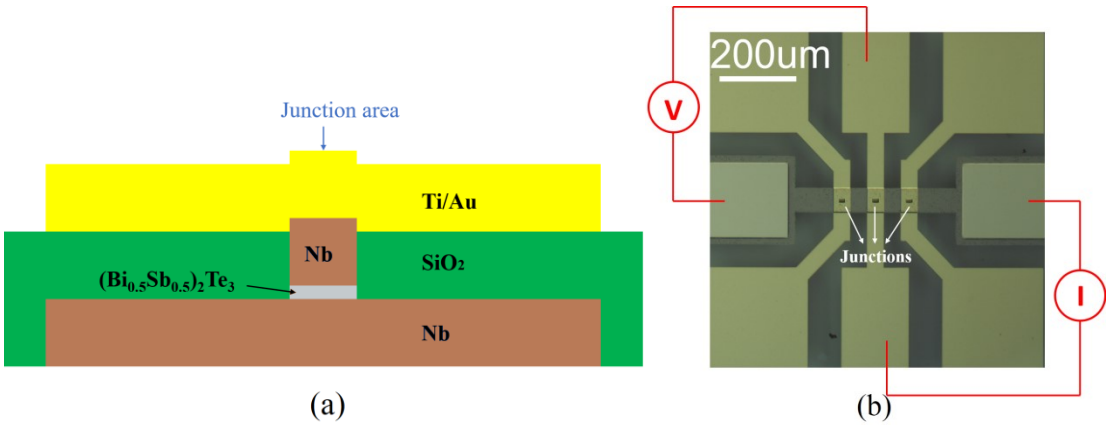

Figure 3-7: (a) A schematic layout of the junction area , which is a pillar standing on the Nb bottom strip and capped by a Au/Ti top strip. (b) An optical microscope image of the device, showing the top view of three junctions and the electrical connections on the middle junction.

Chapter 4
MBE growth of topological insulator $(Bi_{1-x}Sb_x)_2Te_3$ thin film and heterostructures

The ternary compound $(Bi_{1-x}Sb_x)_2Te_3$ is a kind of 3D TI and Nb is a widely used BCS superconductor. By growing $(Bi_{1-x}Sb_x)_2Te_3$ on Nb thin film, we will get one of the TI-S heterostructures to be studied in the following part of this thesis. This chapter mainly focuses on the MBE growth methods and characterization results. After a brief review of the material properties as well as the development history for the MBE growth of $(Bi_{1-x}Sb_x)_2Te_3$ thin films, we will show the optimized growth results of $(Bi_{1-x}Sb_x)_2Te_3$ thin films on different kinds of substrate in our MBE system. Afterwards, growth and characterization of the heterostructure $(Bi_{1-x}Sb_x)_2Te_3$-Nb will be discussed.

The growth part of this chapter was collaborated with Dr. Hui Zhang and Xiaodong Ma, who was a postdoc fellow in the group and an exchange student from the University of Science and Technology of China (USTC) respectively.

4.1 Introduction

The compound family of $(Bi, Sb)_2(Se, Te)_3$ had been known for decades as excellent thermal electrical materials. Most studies focused on their thermal electricity properties until the discovery of 3D TI. In 2009, the theoretical work [37] predicted Bi_2Se_3, Bi_2Te_3 and Sb_2Te_3 are topological insulators, which opened a new direction for the study on this class of materials. Soon after the prediction, the single Dirac cone surface states were confirmed by experiments in these materials [27, 38, 41]. In this project, we chose the tellurides TI instead of selenides because Te has relatively low vapor pressure compared with Se thus will help reduce vacancies which contribute undesired carriers in the bulk. By mixing Bi and Sb with arbitrary ratio x, the ternary telluride $(Bi_{1-x}Sb_x)_2Te_3$ is also a topological insulator with well-defined Dirac point in the band gap. The band structure of $(Bi_{1-x}Sb_x)_2Te_3$ can be engineered by fine tuning the ratio x to reduce bulk current leakage [87]. In the following part of this section, we will focus the discussion on the tellurides TI.

Bi_2Te_3 and Sb_2Te_3 share the same rhombohedral crystal structure as schematically shown in Figure 4-1 (a). Along the [0001] crystal direction, the unit cell contains five atomic layers with a stacking sequence of Te-Bi/Sb-Te-Bi/Sb-Te, forming a quintuple layer (QL) terminated by a Te atomic layer on both sides. For a hexagonal cell containing 15 atoms grouped in 3 QLs, the lattice constant is a_{BiTe} = 4.38 Å, c_{BiTe} = 30.487 Å and a_{SbTe} = 4.26 Å, c_{SbTe} = 30.458 Å [88]. The thickness of one QL is about 1 nm. The bond between two atomic layers within a QL is covalent bonding while the interaction between two adjacent QLs is a much weaker *van der Waals* type.

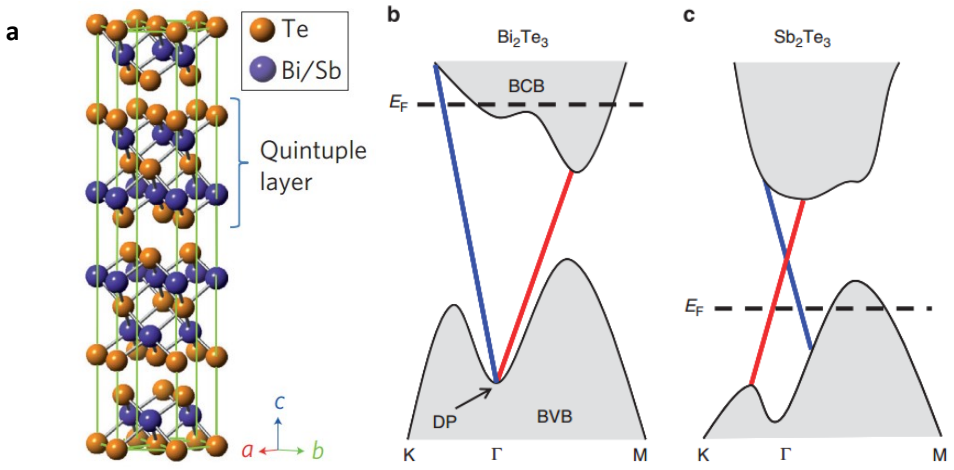

Figure 4-1: (a) Crystal structure of $(Bi/Sb)_2Te_3$. (b) Schematic electronic band structure of pure Bi_2Te_3 and pure Sb_2Te_3. Fermi level in pure Bi_2Te_3 is buried in conduction band and carriers are n-type. Fermi level in pure Sb_2Te_3 is buried in valence band and carriers are p-type.

Although binary compounds Bi_2Te_3 and Sb_2Te_3 have been verified to have exotic surface states, their bulk states are highly metallic, with the Fermi level (E_F) located deep inside the bulk conduction band (BCB) for Bi_2Te_3 (n type) and bulk valence band (BVB) for Sb_2Te_3 (p type) respectively, due to excessive carriers arising from crystal defects and vacancies. The schematic electronic band structure of pure Bi_2Te_3 and pure Sb_2Te_3 is shown in Figure 4-1 (b), (c) [87]. This high bulk conductivity will inhibit the performance of topological surface state. Another drawback of Bi_2Te_3 is its Dirac point is buried in BVB making it difficult to access the surface state by transport, whereas Sb_2Te_3 has well defined Dirac point in the bulk band gap. As Bi_2Te_3 and Sb_2Te_3 have the same crystal structure, Bi can be substituted by Sb with arbitrary ratio to form the ternary compound $(Bi_{1-x}Sb_x)_2Te_3$. By doping

Sb into Bi_2Te_3, one can simultaneously compensate the charge carriers and tune Dirac point to the bulk gap as desired. Systematic investigations on band structure engineering in $(Bi_{1-x}Sb_x)_2Te_3$ thin film have been done by ARPES, STM/STS as well as transport measurements [87, 89, 90]. The ARPES measurement [89] on $(Bi_{1-x}Sb_x)_2Te_3$ thin film with various x is shown in Figure 4-2. Clearly, when the concentration of Sb is increasing, there is a trend that E_F moves downward from the BCB to the BVB while the Dirac point moves upwards. The bulk insulating state was achieved around x = 0.5. In the meantime, the Dirac point was exposed in the bulk gap as desired. Once the carrier density is significantly reduced, relative position between E_F and Dirac point can be further tuned by applying gate voltage [90].

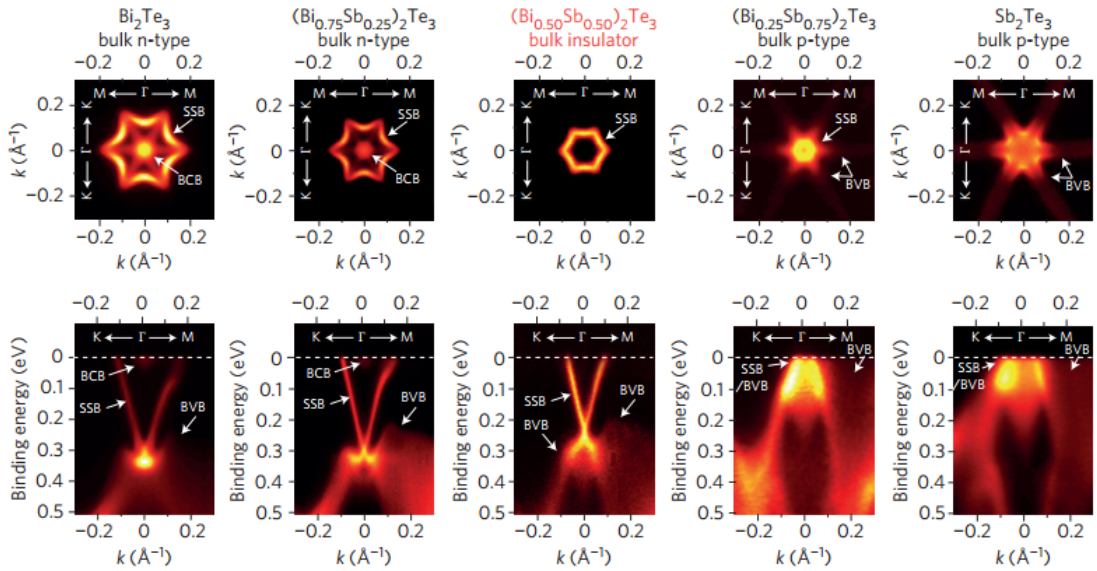

Figure 4-2: ARPES measurements on $(Bi_{1-x}Sb_x)_2Te_3$ with different concentration ratios. E_F is tuned from the BCB to the BVB by increasing the concentration of Sb. A bulk insulating state is achieved at $x \approx 0.5$ [89].

There are many ways to synthesis TI materials, including chemical vapor deposition (CVD) [91, 92], bulk Bridgman growth [27, 38, 93], wet chemical synthesis [94, 95], and molecular beam epitaxy (MBE) [44, 45, 96-98]. Among these methods, MBE is the most advanced technique to grow TI thin film with high crystal quality and controllable electronic properties. The MBE growth mechanism for

TI materials is different from that for conventional MBE growth because the bond between different QLs of TI is weak *van der Waals* interaction, which relaxes the lattice-matching condition required for most common epitaxial growth of covalent semiconductors [99]. Epitaxial TI films grown on different kinds of substrates have been reported [45, 100-107]. By carefully regulating the growth temperature and flux ratio, layer-by-layer MBE growth mode has also been realized [105-107].

Despite the reports of successful growth results in literature, it is not a trivial task to grow high quality TI films by just copying the same condition because there is subtle difference between individual growth systems and the growth window of TI is relative narrow thus sensitive to any difference. In addition, when this project started, our growth system was brand new which required calibration and optimization. Therefore, it was necessary to reproduce high quality TI films in our system before moving forward to growing heterostructures. In the following part of this chapter, first, by showing the characterization results of the $(Bi_{1-x}Sb_x)_2Te_3$ films grown on different substrates including (111)-Si, *c*-cut sapphire and (111)-$SrTiO_3$ (STO), we will demonstrate the BST films grown in our system have high crystalline quality and well controlled electronic band structure. Afterwards, we report the innovative growth of $(Bi_{1-x}Sb_x)_2Te_3$ on Nb thin film, which is a TI-S heterostructure on wafer size scale to realize superconducting proximity on TI surface states.

4.2 MBE growth of $(Bi_{1-x}Sb_x)_2Te_3$ thin film

4.2.1 Substrates preparation

Despite *van der Waals* epitaxy relaxes the requirement for lattice matching, the substrate's lattice and surface condition still affects the quality of TI films to some extent. We chose the substrates Si (111), *c*-cut sapphire and STO (111) because their hexagonal surface lattices are well matched with $(Bi_{1-x}Sb_x)_2Te_3$. Si and sapphire wafers are 2-inch which is the standard size in the Omicron growth system, and they will also be used to grow the heterostructures. The STO substrate is 5 cm × 5 cm and is used for gate tuning of $(Bi_{1-x}Sb_x)_2Te_3$ film because of its large dielectric constant. The substrates were prepared in the following ways to get a clean and flat surface which is critical in MBE growth, since any surface disordering or contamination would result in crystal defects or secondary phases in the epitaxial layers.

1. Si (111)

The Si (111) wafer was dipped in 10-1 buffered oxide etch (BOE) solution for 1 minute to remove the native oxide and form hydrogen passivated surface. It has been reported that hydrogen passivated Si (111) surface can promote *van der Waals* growth of TI materials because the hydrogen atoms will saturate dangling bonds on Si surface thus avoid reconstructions [108]. After rinsed with DI water, a water free surface indicates successful cleaning results. The substrate was then loaded into load-lock as soon as possible.

2. Sapphire

To ensure the transparent sapphire substrate can be heated effectively through thermal radiation from the non-contact heater, the backside of sapphire was deposited with 100nm metal, which can be Nb or Ti. Then the substrate was transferred to preparation chamber where top surface of sapphire was sputtered by RF Ar plasma at 50W for 5 minutes to remove surface contamination. During this step, the surface was damaged by the plasma and became amorphous. Afterwards, it was transferred to growth chamber and went through the following annealing process to recover good crystalline surface:

- Heat to 500 ℃ in 3 minutes, stay for 30 seconds then decrease to 300 ℃ and wait for 1 hour. Repeat twice more.
- Heat to 600 ℃ in 3 minutes, stay for 30 seconds then decrease to 300 ℃ and wait for 1 hour. Repeat twice more.
- Heat to 750 ℃ in 3 minutes, stay for 30 seconds then decrease to 300 ℃ and wait for 1 hour. Repeat twice more.
- Decrease to growth temperature and wait for at least 30 minutes for temperature to be stable.

3. STO

To obtain an atomic flat surface, the STO substrate was first etched by 10-1 BOE solution for 3 minutes and rinsed in DI water for 1 minute, then annealed in tube with mixture of 20% oxygen and 80% Ar gas flow at 1000 ℃ for 150 minutes.

4.2.2 Growth conditions

For simplicity, we started from growing binary compound Bi_2Te_3 to find the optimal growth conditions for high quality epitaxial film. High-purity Bi (99.999%) and Te (99.999%) sources were

evaporated by effusion K-cell and cracker source respectively. All fluxes and growth rates were calibrated by BFM and QCM in advance. During the growth, Te flux rate were fixed by keeping reservoir temperature at 400 ºC. Bi effusion cell temperature varied within 490 ºC - 530 ºC to adjust flux ratio. According to the phase diagram [109], a Te-rich environment is necessary for the nucleation of Bi_2Te_3. Therefore, the ratio of Bi:Te was maintained between 1:4 ~ 1:6. The optimal substrate temperature varied slightly for different substrates due to their difference in thermal radiation absorbent efficiency and in surface energy. The set values for the three substrates were T_{Si} = 270 ºC, $T_{Sapphire}$ = 210 ºC and T_{STO} = 300 ºC.

Following the optimal growth condition for Bi_2Te_3 film, Sb was doped without sacrificing crystalline quality. The ratio of Bi:Sb can be changed by regulating source temperatures. Sb temperature was changed within 390 ºC - 430 ºC to vary Bi:Sb from 2:1 to 1:3 (corresponding to x = 0.25 ~ 0.67).

4.2.3 Characterization results

The surface condition of samples was monitored by RHEED in real time during growth. Figure 4-3 (a-c) show the RHEED patterns of different substrates before growth and Figure 4-3 (d-e) are the patterns of 7 nm BST films grown on them. Streaky RHEED patterns indicate the films grown on all three substrates have atomic flat surfaces. RHEED intensity oscillations were also observed. The oscillation decayed after about 5 ~ 7 QLs, indicating the layer-by-layer growth mode collapsed as the film growing thicker due to weak *van der Waals* interaction between layers. However, streaky RHEED patterns were still preserved for thicker films up to 20 QLs.

In addition to RHEED, *ex situ* XRD was performed to characterize the bulk crystalline quality of the $(Bi_{1-x}Sb_x)_2Te_3$ films and the results were similar on all three substrates. Figure 4-4 shows the coupled θ-2θ scan of a $(Bi_{1-x}Sb_x)_2Te_3$ film grown on sapphire, where only the characteristic diffraction peaks from the plane family {0 0 0 1} can be seen, confirming the film was *c*-axis orientated. Figure 4-5 shows the 360º Φ scan of another film grown on Si (111), looking at the plane (0 1 $\bar{1}$ 5). The six fold symmetry further confirmed the $(Bi_{1-x}Sb_x)_2Te_3$ film was epitaxial with expected in plane orientation.

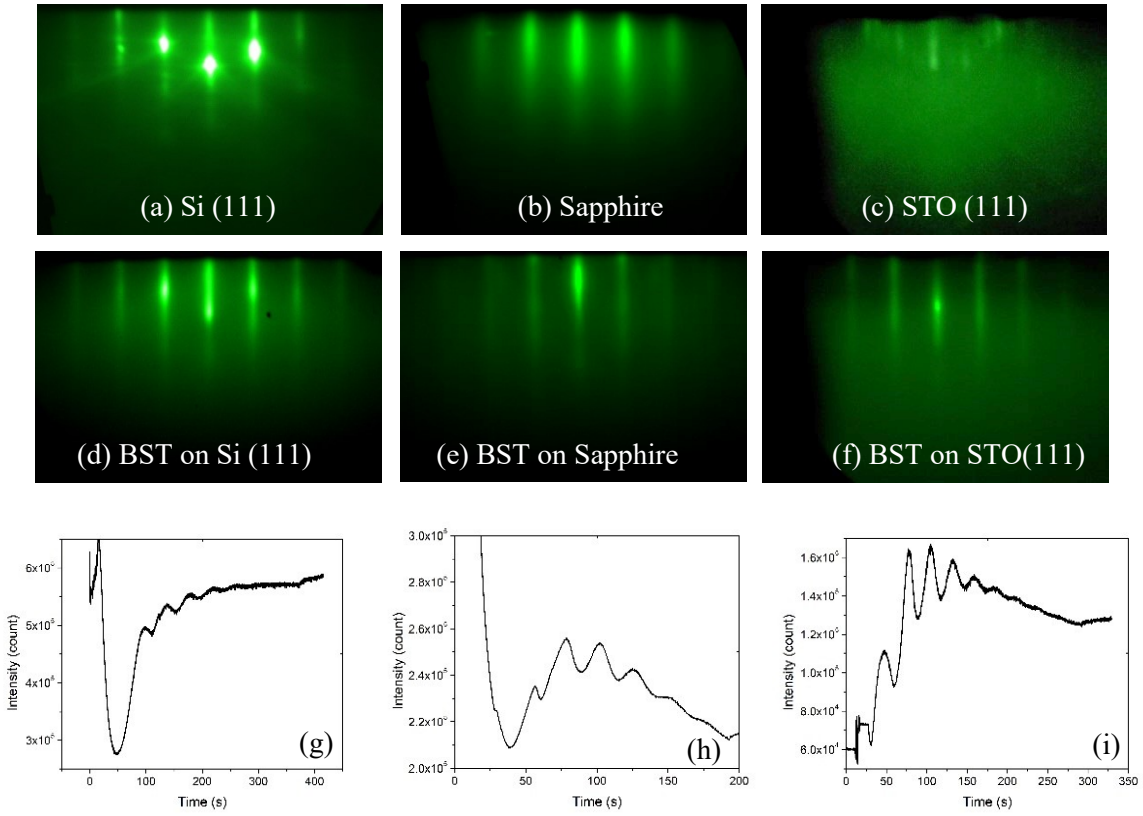

Figure 4-3: (a)-(c) RHEED patterns of Si (111), *c*-cut sapphire and STO (111) substrates after being treated by corresponding procedures. (d)-(f) $(Bi_{1-x}Sb_x)_2Te_3$ films grown on different substrates, incident along [1 1 $\bar{2}$ 0]. (g)-(i) RHEED intensity oscillations during the growth on each substrate.

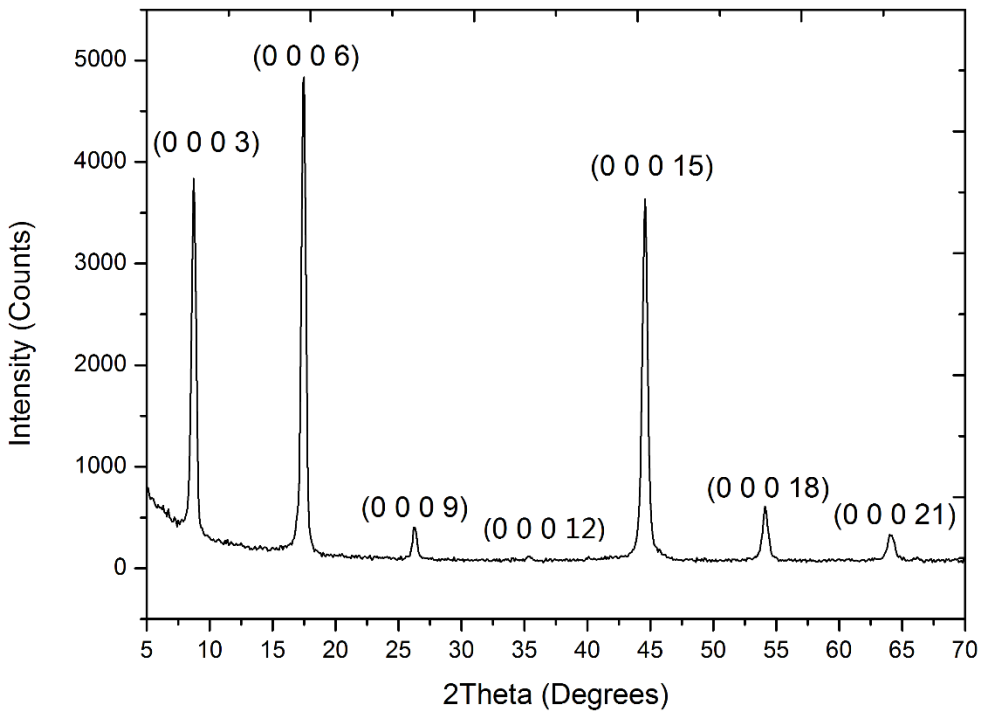

Figure 4-4: XRD coupled θ-2θ scan showing peaks from $(Bi_{1-x}Sb_x)_2Te_3$ {0 0 0 1} plane family. Substrate is sapphire.

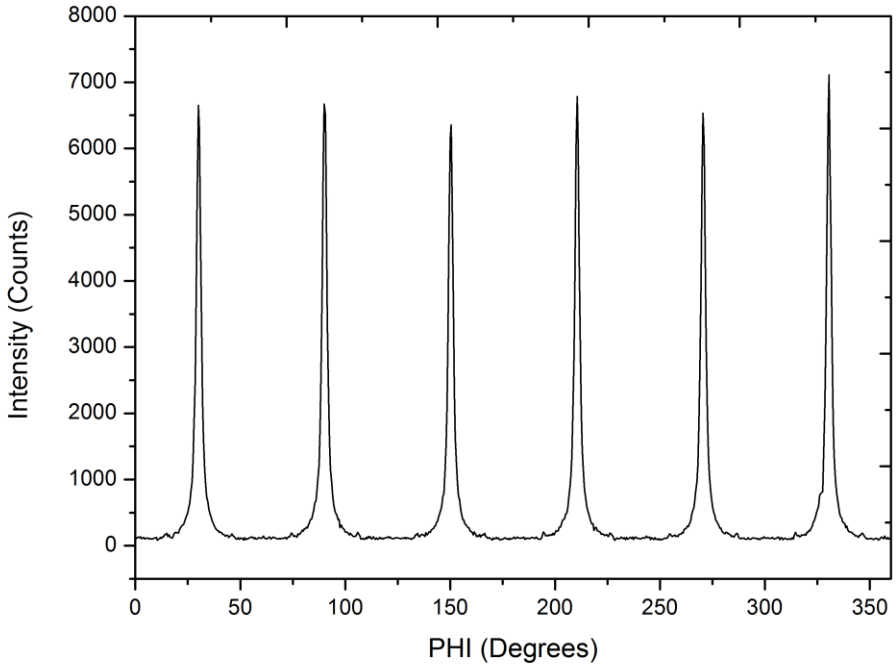

Figure 4-5: XRD azimuthal Φ scan of $(Bi_{1-x}Sb_x)_2Te_3$ on Si (111), seeing (0 1 $\bar{1}$ 5) plane.

Besides the crystalline quality, the chemical stoichiometry of the $(Bi_{1-x}Sb_x)_2Te_3$ thin films was characterized *in situ* by XPS. According to literature [87], the bulk insulating $(Bi_{1-x}Sb_x)_2Te_3$ film should be achieved when the ratio $x \cong 0.5$. With this ratio, the Dirac point of topological surface state can be tuned within the bulk band gap, previously reported by ARPES. In this project, $(Bi_{1-x}Sb_x)_2Te_3$ thin films with different x values were grown on STO and Hall measurements were performed to compare their carrier density. The thickness of these films is about 7 nm, which is also the typical thickness used for our heterostructure later. Figure 4-6 shows the carrier density of four samples measured at 4K. The film with $x \sim 0.5$ has the lowest carrier density, which is about 5×10^{12} cm^{-2}. Back gating voltage was further applied to the $(Bi_{0.5}Sb_{0.5})_2Te_3$ film. Figure 4-6 (b) shows the sheet resistance and carrier density at different gating voltages. The Fermi level is tuned across Dirac point with R_{xx} maximized around $V_G = 20$ V. On the other hand, sheet carrier density is close to its minimum at $V_G = 12$ V. The Hall measurements confirmed that our $(Bi_{0.5}Sb_{0.5})_2Te_3$ film is bulk

insulating and the surface states can be well tuned by applying gate voltages, consistent with literature [87].

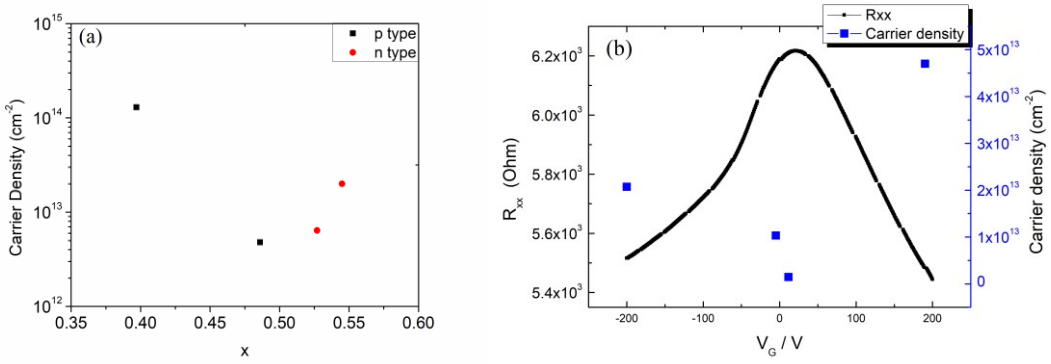

Figure 4-6: (a) Sheet carrier density dependence on Sb concentration (b) Sheet resistance (left) and carrier density (right) tuned by gate voltage

4.3 MBE growth of $(Bi_{0.5}Sb_{0.5})_2Te_3$ (BST)-Nb heterostructure

In previous sections, the $(Bi_{0.5}Sb_{0.5})_2Te_3$ (BST) film has been verified to have high crystalline quality and low carrier density, which is preferable for the study on its surface states. The TI-S or S-TI heterostructure provides a platform to induce 2D topological superconductivity at the bottom or top interface of TI through superconducting proximity effect. Different from most studies in literature, where the heterostructures were built using TI flakes [48] or superconductor flakes [11-13, 81], we aimed at growing TI-S multilayers on wafer size scale. In this section, we will show the growth methods and characterization results of BST-Nb heterostructure. The superconductor Nb was chosen because of its stability and compatibility with the subsequent fabrications. Note a kind of S-TI heterostructure can be easily obtained in our growth system by simply depositing Nb on top of BST at room temperature. But in the opposite way, it is not trivial to grow BST on top of Nb because the growth of BST requires elevated substrate temperature, and this temperature needs to be readjusted due to existence of Nb.

Si (111) and *c*-cut sapphire substrates were used to deposit the heterostructure. The deposition follows several steps. First, the substrates were treated following the same preparation procedure described in section 4.2.1, then transferred under vacuum to a magnetron-sputtering chamber to

deposit the Nb film. The base pressure of this sputtering chamber was kept at 1×10^{-10} mbar to reduce foreign compounds such as Nb oxides. The Nb film was deposited at room temperature. The Ar gas flow was 30 sccm and injected near the sputtering targets. The pressure during growth was kept at 5×10^{-3} mbar and the power for growth was 200 W, giving the growth rate 2 Å/s. After the deposition of 50 nm Nb thin film, the sample was then transferred to the MBE chamber for the BST film deposition.

Before growing BST, the surface condition of Nb film was characterized by RHEED. Figure 4-7 shows the RHEED pattern of a 50 nm Nb film deposited on the sapphire substrate. The Nb surface was smooth, indicated by the streaky RHEED patterns. The six-fold symmetric RHEED patterns coupled with *ex situ* XRD scans, indicates that the Nb film is (110) highly textured, with three equivalent layouts simultaneously present on the hexagonal sapphire lattice. Despite the good Nb quality, when we attempted to deposit the BST films on Nb following the same condition as they were grown directly on the bare substrates, RHEED patterns indicated amorphous film. This is in sharp contrast to the previous results, where RHEED showed perfect streaky patterns and clear layer-by-layer intensity oscillations. We employed XPS to check the chemical composition of the amorphous film and found out the Te element was much more concentrated while Bi & Sb were insufficient compared to the desired $(Bi_{0.5}Sb_{0.5})_2Te_3$ film, see Figure 4-8, which means the deposition at regular growth temperature didn't realize the stoichiometric $(Bi_{0.5}Sb_{0.5})_2Te_3$ phase. It was similar to the case when substrate temperature is higher than the decomposing temperature of $(Bi_{0.5}Sb_{0.5})_2Te_3$, indicating that the real temperature might be higher when the Nb film was coated than that on a bare substrate if using same set values. Considering the substrate was heated through thermal radiation from a heater mounted at the backside, the Nb film coating can affect its thermal property. On one hand, Nb will absorb more infrared radiation that was originally transparent through the substrate. On the other hand, the thermal emissivity constant of Nb at the growth temperature is quite low (7% at 270 ºC) [110], which means it reflects the radiation back to the substrate and blocks the heat transfer to vacuum. As a result, the actual substrate temperature can be elevated. To compensate this increment, we decreased the set value of substrate temperature to lower the power applied to the heater. It turns out that the $(Bi_{0.5}Sb_{0.5})_2Te_3$ films grown at this decreased temperature showed expectant single crystallization and correct chemical stoichiometric. Figure 4-7 (c) and (d) Figure 2-1compare the RHEED patterns of two BST films grown on Nb-Si (111) when substrates were set at

270 ºC and 150 ºC respectively. The one at 270 ºC shows amorphous surface, while streaky patterns show up at 150 ºC. Clearly the setting value for substrate temperature needs to be re-adjusted to 150 ºC for successful formation of BST. Similar influence on substrate temperature from coated film was also found when we grew other heterostructures, including MgB_2-MgO-MgB_2 and BST-MgB_2, which will be discussed in chapter 6 and chapter 7.

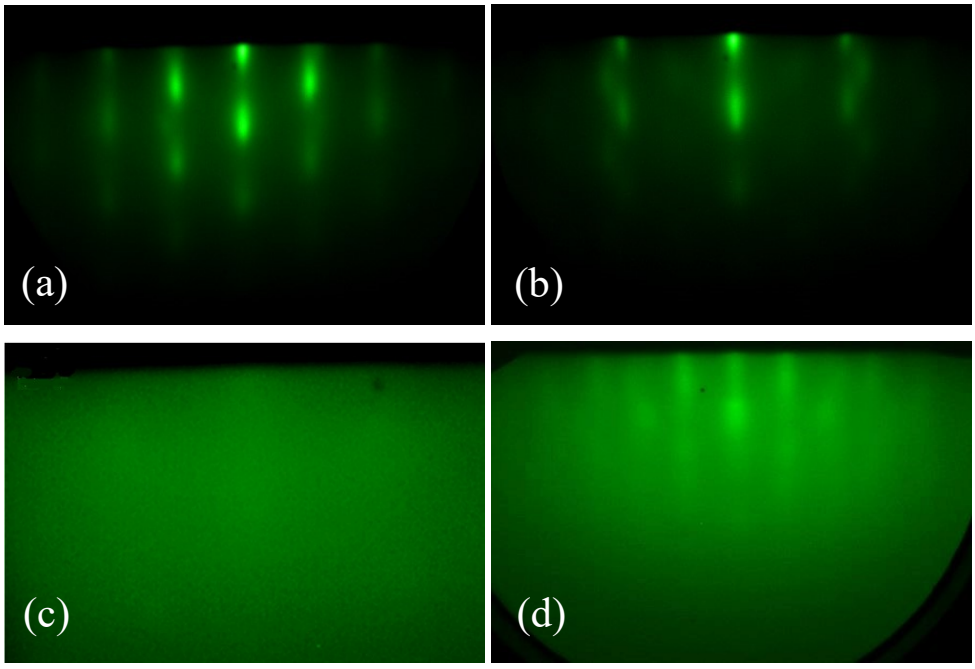

Figure 4-7: (a) and (b): Two sets of RHEED patterns of Nb film showing up alternatingly every 30° as sample was rotating azimuthally, suggesting the (110) oriented Nb film is highly textured with six-fold symmetry (c) BST grown on Nb when substrate was set at 270 ºC (d) BST grown on Nb when substrate was set at 150 ºC

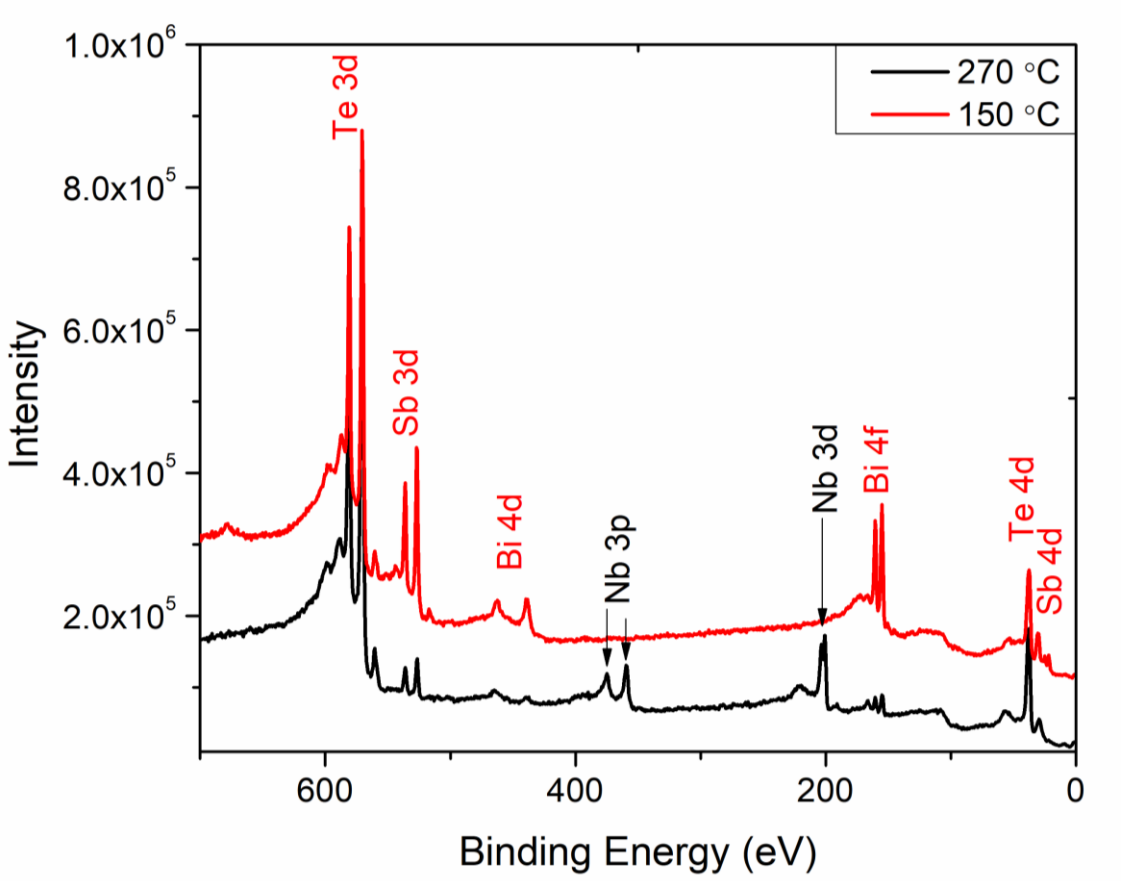

Figure 4-8: XPS survey scan on BST films grown on Nb at 150 ºC and 270 ºC

A two-step growth method introduced in reference [111] can further improve the quality of BST films grown on Nb. Following this method, a thin passivation layer of Bi-Sb-Te (0.5nm) was deposited at low temperature (150 ºC), then annealed to 210 ºC with a slow ramping speed. RHEED patterns became brighter and clearer during this annealing process, suggesting it can aid crystallization in the Bi-Sb-Te passivation layer. After annealing, the temperature was again lowered to the passivation layer deposition temperature and another passivation layer was grown. After a few cycles of such passivation step, 1~2 nm Bi-Sb-Te crystallized layer was formed. Then the $(Bi_{0.5}Sb_{0.5})_2Te_3$ film was deposited at 150 ºC. Figure 4-9 shows the RHEED pattern for a typical BST film deposited using the two-step methods. The bright streaky pattern indicates the film has flat surface morphology.

The quality of BST films grown on Nb was then characterized *ex situ* by XRD. Figure 4-10 (b) shows the θ-2θ scans. The peak positions are consistent with the reflections from only {0001} lattice plane family, which indicates the well orientated *c*-axis growth of BST films. To examine the quality of the interface between BST and Nb, cross-sectional high-resolution transmission electron microscopy (HRTEM) measurement with an acceleration voltage of 200 KeV was performed on one of the two-step deposited samples. Figure 4-10 (a) shows a film of 12 QLs of BST (~ 12 nm) on top of 60 nm Nb. An epitaxial layered structure of BST film on Nb surface can be clearly observed, with very high structural perfection. The first several quintuple layers do not show any amorphous nature or half BST quintuple layer indicating that growing with the two-step method indeed prevents amorphous BST formation, and promotes top BST layers *Van der Waals* epitaxy.

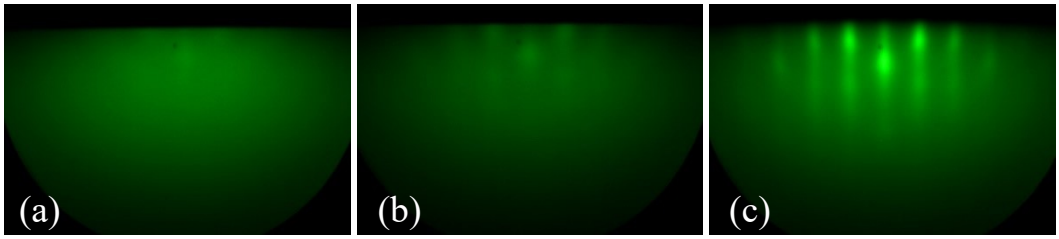

Figure 4-9: RHEED pattern evolution during two-step growth of BST on Nb. (a) 0.5 nm Bi-Sb-Te passivation layer deposited at 150 ºC (b) anneal to 210 ºC (c) 7nm BST grown by two step method.

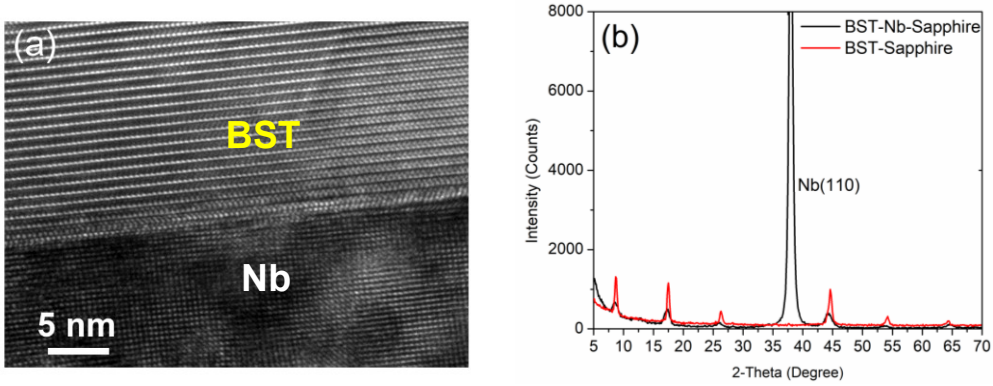

Figure 4-10: (a) Cross-sectional HRTEM image showing the interface of BST-Nb (b) XRD θ-2θ coupled scan results comparing the BST films grown on Nb and directly grown on sapphire.

4.4 BST-EuS heterostructure: magnetic proximity

Introducing ferromagnetic order into TI will open up a gap on the surface states. Interplay between a magnetic gap and a superconducting gap on the TI surface can lead to chiral Majorana modes [60, 78]. Doping TI with magnetic elements is an effective way to introduce ferromagnetism, through which researchers have realized the quantum anomalous insulator (QAHI) [6, 79, 112]. More inspiringly, signature of chiral Majorana modes has been reported in a heterostructure combining a QAHI and a superconductor [79].

Magnetic interaction can also be induced through proximity with ferromagnetic insulator. Compared with the doping method, this will avoid introducing crystal defects hence avoid affecting the bulk conductivity of TI. In addition, the short-range nature of exchange interaction will ensure magnetic response is from the TI surface states instead of bulk carriers. EuS is a typical Heisenberg-type ferromagnetic insulator with a large exchange splitting on its conduction band (0.36 eV at 0.4 K) and the Curie temperature of bulk EuS is 16.7 K [113]. Each Eu^{2+} ion has a large magnetic moment of $7\mu_B$ (Bohr magneton) from the half-filled 4*f* bands [114]. With a reasonably large bandgap, EuS is widely used as tunnel barrier for spin filtering magnetic tunneling junctions [115-117]. Moreover, it has been reported that EuS can provide effective exchange coupling with TI surface states in different TI-EuS heterostructures [118-124]. Here we grew heterostructures including EuS-BST, BST-EuS and BST-EuS-BST sandwich structure. The substrates can be Si (111) or *c*-cut sapphire. In either of the heterostructures, ferromagnetic order has been successfully introduced onto the surface of BST.

EuS was evaporated by the e-beam evaporator. Figure 4-11 (a) and (b) show the RHEED patterns of EuS (001) grown on BST thin films at 100 ºC. Two different sets of patterns are seen along [100] and [110] azimuthal incidence, suggesting the EuS film is single crystalline with good in-plane orientation. Inversely, BST thin film can also grow epitaxially on EuS following the same growth condition as it was grown on bare substrates. Figure 4-11 (c) and (d) show the RHEED patterns of BST film grown on EuS at 250 ºC, along $[10\bar{1}0]$ and $[11\bar{2}0]$ incident directions. Despite the roughness of underneth EuS film indicated by the dotted patterns in (a) and (b), after BST film was grown, streaky patterns devleoped. This suggests the *van der Waals* epitaxy mode helps relax the

BST film as it is growing and smooth its surface, although the streaks are thicker compared with BST films grown directly on bare substrates.

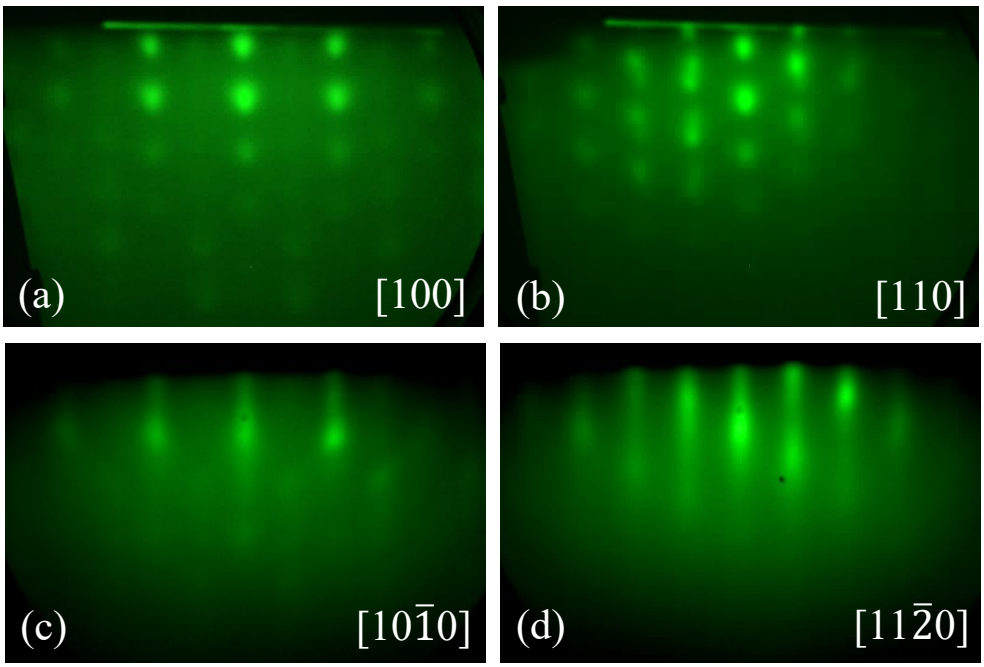

Figure 4-11: (a) and (b): RHEED patterns of EuS (001) film grown on BST, incident along [100] and along [110]. (c) and (d): RHEED patterns of BST grown on top of EuS, incident along [10$\bar{1}$0] and [11$\bar{2}$0].

The magnetic property of the heterostructures was determined by measuring magnetoresistance (MR) at 4.2K. Similar results were observed on both BST-EuS bilayer or BST-EuS-BST trilayer structures. In Figure 4-12 , we show the typical MR of a BST-EuS-BST structure. Both BST layers are 15 QLs and EuS is 8 nm. Sample was cut into 1 cm^2 square and 4 wires were connected on the 4 corners. Longitudinal resistance (R_{xx}) was measured by sending current along one edge of the square and reading voltage on the opposite edge. Magnetic field was applied parallel and perpendicular to the sample surface. With parallel magnetic field, the MR curve shows two hysteretic dips at H = $\pm$63 Oe, corresponding to the coercive fields H_c of EuS. This is consistent with the results observed in a Bi_2Se_3-EuS heterostructure [118]. The hysteretic MR is an indication that the BST film is induced

into ferromagnetic phase. The MR dips were not observed in perpendicular field setup, see Figure 4-12 (b), because EuS favors in-plane anisotropy at the given thickness.

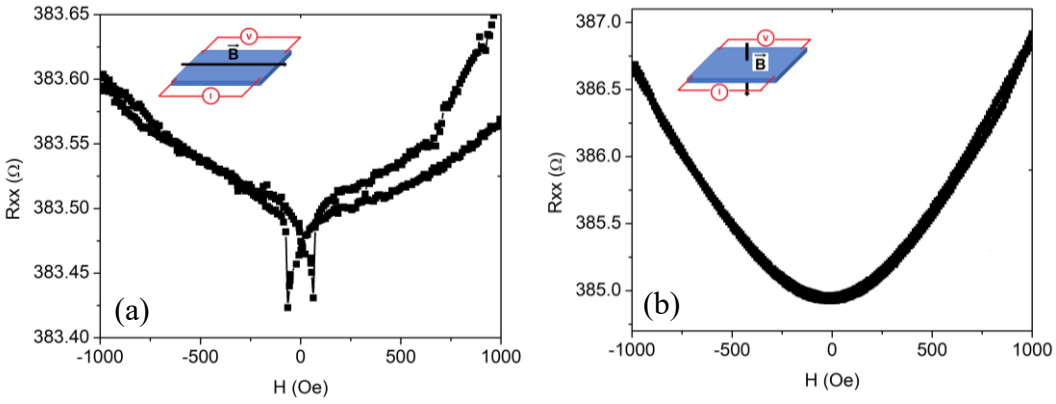

Figure 4-12: Magnetoresistance measured on a BST-EuS-BST trilayer heterostructure with magnetic field parallel to sample surface-(a) and perpendicular to sample surface-(b). The inset figures show corresponding measurement setup.

4.5 Conclusions

In this chapter, first we have shown that the $(Bi_{0.5}Sb_{0.5})_2Te_3$ thin film grown in our system is epitaxial with good surface morphology. Transport measurements on our $(Bi_{0.5}Sb_{0.5})_2Te_3$ thin film confirmed it is bulk insulating, which is desired to utilize its exotic surface states for further study. More importantly, we developed and optimized the method to grow wafer scaled BST-Nb heterostructure by MBE. Characterization results showed the heterostructure has high crystalline quality and clear interface. On the other hand, by growing BST-EuS heterostrucure, we can introduce ferromagnetic order onto the BST surfaces. Both the superconducting proximity and magnetic proximity effects on TI, or combination of these two effects, can lead to exotic Majorana states. The heterostructures provide a good platform for further study as well as paves a way to make scalable devices for quantum technology in the future.

Chapter 5
Vertical Nb-BST-Nb junctions

5.1 Introduction

Being able to grow high quality BST on top of Nb, or simply deposit Nb on top of BST, we can obtain TI-S or S-TI heterostructures. In these two types of structures, the superconducting proximity effect exists on the bottom or top surface of TI and different experimental approaches are needed to access them. For example, TI-S structure is more suitable for scanning tunneling microscopy (STM) studies, like those done by [11-13]. With the STM tip approaching from the top while proximity effect coming from the bottom, tunneling spectroscopy can see thickness dependence of the induced superconducting gap. By applying perpendicular magnetic field to generate vortices, one can expect to see signatures of tunneling via Majorana states bound in the vortex core. Whereas for an S-TI structure, STM study might be more challenging because the signals from the superconductor on top will dominate. Instead, the S-TI bilayer structure can be fabricated into planar S-TI-S Josephson junction by creating a gap on the S layer, shown in Figure 5-4. In this configuration, a 4π periodicity of bound states forming in the gap will signal the presence of Majorana modes [14, 15, 125, 126].

In recent years, more and more researches are concentrating on S-TI-S Josephson junctions [14, 15, 125, 126], with most of them being in-plane junctions. We are aiming one step further - to create vertical S-TI-S Josephson junctions with high quality. A vertical S-TI-S structure, which can be seen as a folded planar junction, mimics the sphere model mentioned in [60]. With two superconductor layers covering the top and bottom hemisphere of a 3D TI, a π-phase difference between the two superconductors will yield chiral Majorana modes counterpropagating on the two edges. Furthermore, upon applying an out-of-plane magnetic field penetrating the junction, Majorana zero-modes are predicted to exist on the two ends of a flux line [47]. Furthermore, compared with lateral junctions, vertical junctions with thinner TI film can better maintain superconducting coherence. Therefore, we made vertical S-TI-S Josephson junctions by depositing another layer of Nb on top of the BST-Nb bilayer to get Nb-BST-Nb sandwich structure and then going through the fabrication process mentioned in chapter 3. Electrical transport measurements were conducted on these junctions. Before we move on to discussion about the results, we will briefly review the physical processes including

Andreev reflection and Andreev bound states which can take place at the interface between a superconductor (S) and a normal metal (N). These processes are also associated with transport mechanism in the S-TI-S structure as the surfaces of TI are metallic.

5.1.1 Andreev reflection at the S-N interface

Andreev reflection occurs at the interface between a superconductor (S) and a normal metal (N), as schematically shown in Figure 5-1. When an electron is incident from the N side at energies less than the superconducting energy gap, single-particle transmission is forbidden. Instead, the incident electron has to form a Cooper pair with another electron with opposite spin and velocity to transfer into S, sending a hole with equal momentum back to N. Due to time-reversal symmetry, the process with an incident hole and retroreflected electron will also work. As a result, this process transfers a charge of 2e, leading to excess current and doubled conductance. Andreev reflection is a phase correlated process, where the phase difference between the electron and the reflected hole is $-\pi/2$ plus the phase of the superconducting order parameter. Observation of Andreev reflection requires a clean interface, otherwise specular reflections at an insulating barrier (I) will reduce conductance, see Figure 5-1. The Blonder-Tinkham-Klapwijk (BTK) model [127] provides a general description of how Andreev reflection affects the I-V characteristics and differential conductance spectroscopy across the N-S junction. The barrier height is included in a parameter Z so that the transmission coefficient can be represented as $T = 1/(1+Z^2)$. When the interface is perfectly clean ($Z = 0$), the conductance for $V < \Delta$ is twice of the normal conductance for $V > \Delta$, as a result of Andreev reflection. For an infinitely large Z, the spectroscopy is exactly of a tunneling junction where conductance is 0 within the gap. Figure 5-2 show the I-V and dI/dV-V curves at zero temperature (T) for different values of Z simulated by BTK model [127].

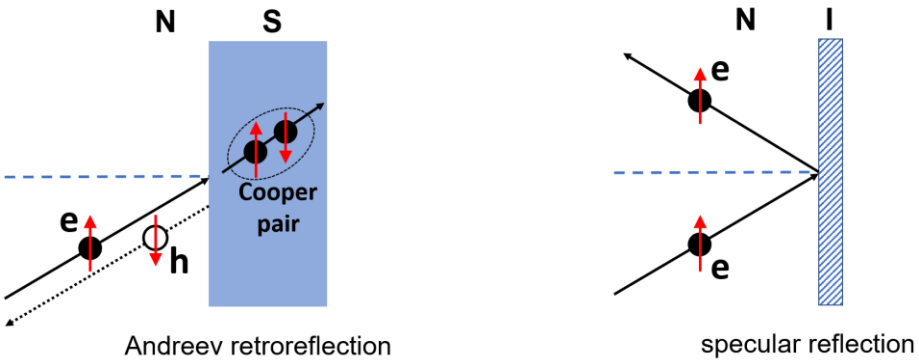

Figure 5-1: Schematic illustration of Andreev reflection at N-S interface (left) and specular reflection at N-I interface (right).

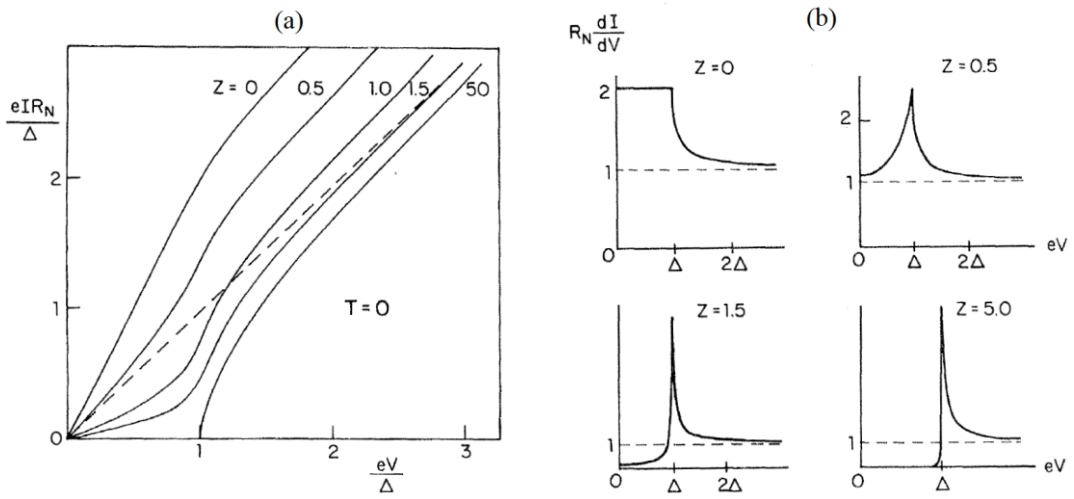

Figure 5-2: (a) I-V characteristics at T = 0 simulated by BTK model for different barrier strengths Z. Z = 0 corresponds to a perfect N-S interface while Z = 50 correponds to an N-I-S tunneling junction. The dashed line indicates the normal-state I-V curve. (b) dI/dV-V curves for various Z values at T = 0 [127].

5.1.2 Andreev bound states in an S-N-S junction

Andreev bound states (ABS) are a set of discrete entangled electron-hole states formed in a confined S-N-S structure as a result of resonant multiple Andreev reflections. The physical process is schematically shown in Figure 5-3. At the right S-N interface, each time an electron is Andreev reflected into a hole, a Cooper pair is effectively generated. When the hole moves to the left interface, it reflects an electron through Andreev reflection, annihilating a Cooper pair in the left S electrodes. Therefore, through an infinite loop of Andreev reflections (electron → hole → electron…), Cooper pairs are transferred from one superconductor to the other, forming dissipationless supercurrent. Standing waves of electron and hole waves going back and forth between two superconductors form the discrete ABS below the superconducting energy gap. These sub-gap bound states are similar to the discrete levels of normal electrons confined in a quantum well, e.x., in a vortex of type-II superconductor. Because each Andreev reflection is a phase correlated process, the resultant ABS are sensitive to the phase difference between the two superconducting electrodes. Two energy levels of bound states ($E = \pm E_B$) can be obtained by solving the Bogoliubov-de Gennes equation [128], $\mathrm{E_B} = \Delta_0\sqrt{1 - T\sin^2(\varphi/2)}$, where $T = 1/(1+Z^2)$ is the transmission coefficient at the interface, $\varphi = \varphi_2 - \varphi_1$ is the phase difference between the two superconductors. These ABS oscillate with φ with a 2π periodicity as schematically shown in Figure 5-3 (b). The Josephson supercurrent carried by the ABS are determined by the phase gradient of these energy levels $\partial E_B(\varphi)/\,\partial\varphi$, which is calculated within the same model as

$$\mathrm{I} = -\mathrm{G_N}\frac{\pi\Delta_0}{2e}\frac{\sin\varphi}{\sqrt{1 - T\sin^2\left(\frac{\varphi}{2}\right)}}\tanh\left(\frac{E_B}{2k_BT}\right)$$

where $\mathrm{G_N} = 2e^2/[h(1+Z^2)]$ is the normal state conductance. The presence of these current-carrying bound states plays a central role as origin of Josephson-like effect for various situations in mesoscopic superconducting systems, including weak links, superconducting quantum point contacts, and conventional tunnel junctions. More detailed introduction to the general feature of Josephson effect is discussed elsewhere in chapter 6.

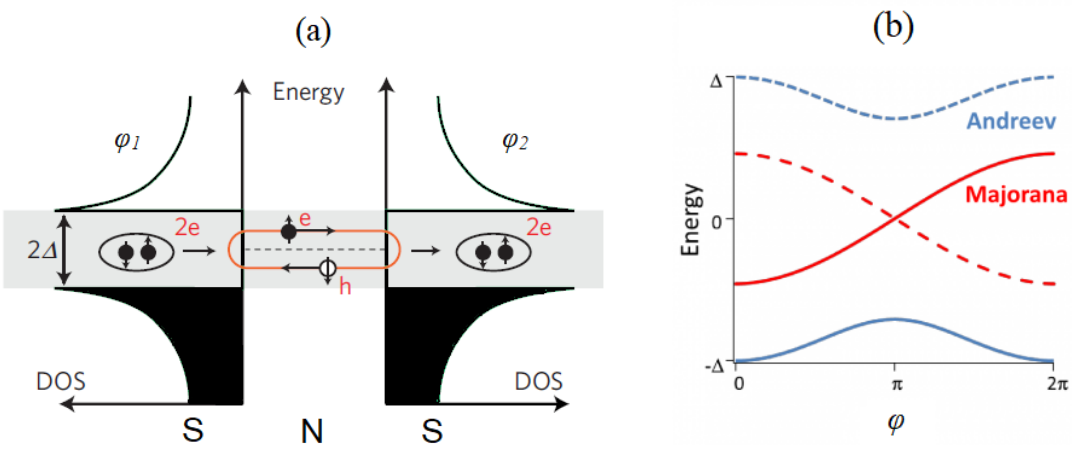

Figure 5-3: (a) Formation of Andreev bound states in an S-N-S junction. (b) Schematic illustration for the phase dependence of the 2π periodic Andreev bound states formed in an S-N-S junction, and the 4π periodic Majorana modes formed in S-TI-S junction.

5.1.3 Andreev bound states and Majorana modes in an S-TI-S junction

Fu and Kane considered an S-TI-S junction (Figure 5-4) in their groundbreaking proposal for the superconducting proximity effect on TI surface [7]. They solved the ABS in the topological surface state channel and found that the spectrum is gapless when the phase difference between two superconductors $\varphi = \pi$, dispersing with the momentum q in the x direction as shown in Figure 5-4 (b). For $q = 0$ and $\varphi = \pi$, the quasiparticle operators corresponding to the two E = 0 modes satisfy $\gamma_+(q) = \gamma_-(q)^\dagger$, which resemble the Majorana modes. The gapless Majorana modes double the period of the gapped ABS, see Figure 5-3 (b), thus will lead to a 4π periodic current-phase relation for the supercurrent flowing across the junction. The proposal made by Fu and Kane boosted both theoretical [17, 126, 129-131] and experimental [14-16, 125, 132] studies on searching for Majorana modes in S-TI-S junctions. Evidence of anomalous current-phase relation has been reported [14, 16, 125] which could be caused by the supercurrent carried by Majorana states. However, there need to be more concrete results to make a firm conclusion.

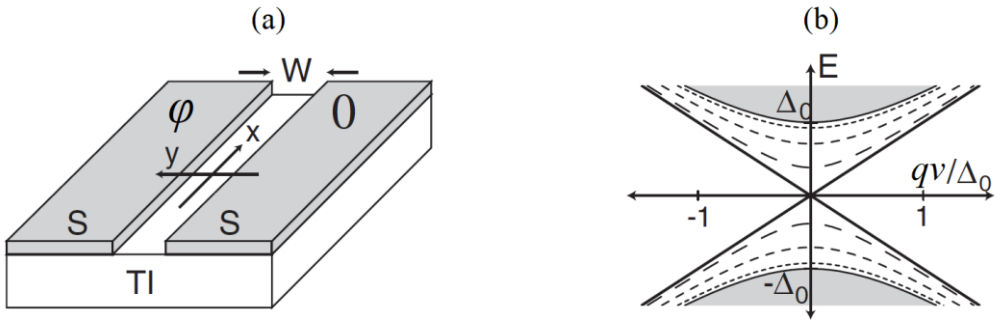

Figure 5-4: (a) An S-TI-S line junction (b) Spectrum of the Andreev bound states formed in the line junction for different φ values, dispersive with momentum q in x direction. The solid line is for $\varphi = \pi$. The dashed lines are for $\varphi = 3\pi/4$, $\varphi = \pi/2$, and $\varphi = \pi/4$. The bound states for $\varphi = 0$ merge with the continuum, indicated by the shaded region. Figures are adapted [7].

5.2 Vertical Nb-BST-Nb junction

Most of the reported studies on S-TI-S structure employed flakes of TI exfoliated from bulk crystal, which restricts the fabrication method to making planar junctions and limits the scalability. We have mentioned that both Nb-BST and BST-Nb structures can be obtained in our MBE system. The Nb-BST structure can be fabricated into planar S-TI-S junctions by creating a small gap on the top Nb layer, similar to those planar junctions using TI flakes yet providing more possibilities for scaling up in the future. Furthermore, by depositing Nb on top of the BST-Nb structure, we obtain Nb-BST-Nb sandwich structure which can be fabricated into vertical S-TI-S Josephson junctions following the fabrication process mentioned in chapter 3.

5.2.1 What to expect in a vertical S-TI-S junction

A spherical model of 3D TI was considered in [60], see Figure 5-5 (a). By coating the top and bottom hemispheres with separate superconductors that have a π phase difference, a pair of counterpropagating Majorana modes will emerge in the gap. A vertical S-TI-S junction can be seen as a deformed version of this sphere by compressing the spherical TI into a sheet with finite thickness. Since the deformation does not change the topology, we would expect the counterpropagating Majorana modes exist on the top and bottom edges of the TI sheet if a π phase shift can be created, for example, by applying a magnetic field in-plane with TI layer. This can also be understood by

thinking a vertical S-TI-S junction as a folded planar junction with its two ends are connected now so that the 1-D nonchiral Majorana modes present in a planar junction develop into chiral Majorana modes with opposite chirality propagating on the side wall of the TI sheet.

Another way to create Majorana modes in a vertical S-TI-S junction is penetrating magnetic flux lines through the junction, as shown in Figure 5-5 (b). We already know the vortex core at the interface of an S-TI or TI-S heterostructure can trap a zero energy Majorana mode. In the S-TI-S structure, with both TI surfaces are proximate to a superconductor, two Majorana zero-modes are expected to exist at the two ends of a flux line. However, as the flux penetrate through the TI bulk, there are possibilities that these two modes will hybridize and disappear. The situations at two opposite physical regimes have been carefully discussed in [47]. In the extreme thin flux limit, which means the spread width of a flux line in TI bulk is much smaller than a lattice constant, the Majorana modes on the two opposite surfaces will hybridize with each other and annihilate. In the thick flux limit, which is likely the regime of most experiments, the two Majorana modes will be well localized the two ends of a flux line.

To experimentally explore the interesting vertical S-TI-S structure, we fabricated and did transport measurements on the vertical Nb-BST-Nb junctions by biasing current. Despite the prediction for existence of Majorana modes, we must keep in mind that the transport behavior can be complicated in these junctions. There are contributions from other trivial mechanisms including Andreev bound states and Josephson effect due to direct coupling between superconducting Nb electrodes. As the surface states become superconducting, it will also add contributions to the conductance.

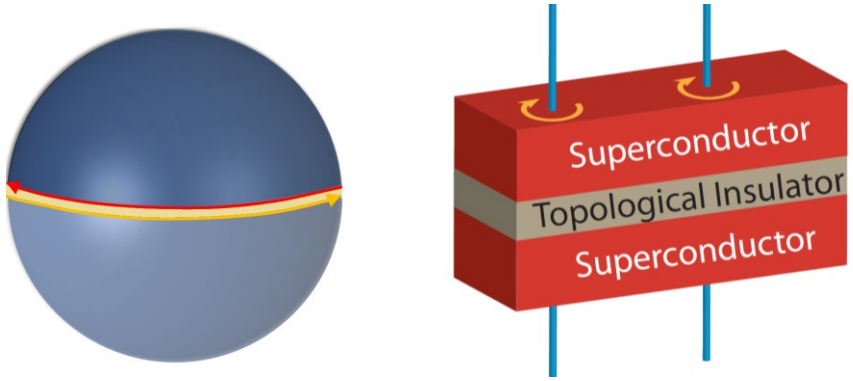

Figure 5-5: (a) 3D TI sphere covered by two separate superconductors. Counterpropagating Majorana modes (indicated by red and orange arrows) will form at the two edges when there is a π phase difference between two superconductors [60]. (b) A vertical S-TI-S junction with magnetic flux penetrating though it. Majorana zero-modes can be bound at the two ends of a flux line.

5.2.2 Transport measurements on vertical Nb-BST-Nb junctions

We fabricated Nb-BST-Nb junctions with different junction areas, 4×4 μm^2, 4×8 μm^2, and 6×6 μm^2. Both top and bottom Nb layers are 50 nm thick and BST is 7 nm. The 7 nm thickness of BST is about the limit for layer by layer growth realized in our system, shown in chapter 4. Meanwhile, it is a reasonable value, being thick enough to avoid direct hybridization between the two surfaces and thin enough for Cooper pairs in the two superconductors to overlap. T_c of the 50 nm Nb electrodes is around 8.1 K ~ 8.2 K, measured on the bottom strips by two terminal methods. The R-T curve is shown in Figure 5-6 (d). Because the two terminals were connected on the two big pads which contain not only the bottom but also the top layer of Nb, we can see the superconducting transitions from both electrodes. Slight difference of T_c from top and bottom Nb gives the small shoulder on the R-T curve. Finite resistance below T_c is from contacts and wires which cannot be eliminated by the two terminal measuring method. The T_c ~ 8.1 K corresponds to a gap value $\Delta \cong 1.2$ meV.

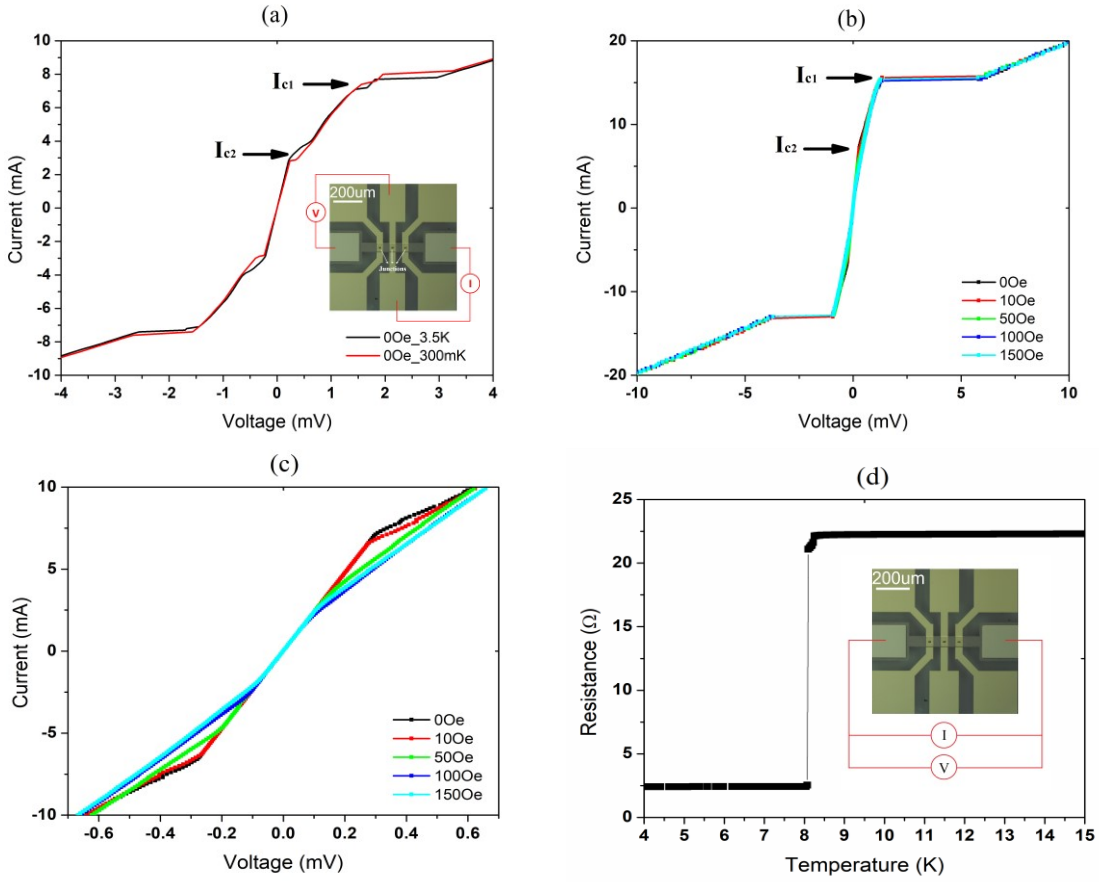

Figure 5-6: (a) The I-V curves measured on the 4×4 μm^2 junction at 3.5 K and 300 mK. (b) The I-V curves measured on the 6×6 μm^2 junction at 3.5 K, showing the behavior of I_{c1} and I_{c2} in parallel magnetic fields. (c) I-V curves on a smaller scale, showing the behavior of I_{c2} in figure "(b)". (d) R-T curve measured on the bottom Nb strip. The inset shows wire connections for the measurement.

Measurements on the junctions were conducted by the 4-terminal method and the connections have been shown in Figure 3-7 (chapter 3). Nine junctions were measured in a continuous flow cryostat at temperatures above 2 K, then six of them were further studied in He^3 fridge down to 300 mK. All junctions exhibited qualitatively similar behaviors. We are going to discuss the typical features measured from two junctions with sizes of 4×4 μm^2 and 6×6 μm^2. Figure 5-6 (a) compares the I-V curves of the 4×4 μm^2 junction measured at 3.5 K and 300 mK respectively. Figure 5-6 (b) and (c) show the I-V curves of the 6×6 μm^2 junction measured at 3.5 K under in-plane magnetic fields within

different ranges of current bias. The I-V characteristics of both junctions share a common feature: there are two critical current values (I_{c1} and I_{c2}) indicated by slope changes, both of whom are dependent on the junction size. I_{c1} is about 8 mA in the 4×4 μm^2 junction and 15 mA in the 6×6 μm^2 junction. I_{c2} is about 3.5 mA in the 4×4 μm^2 junction and 7.5 mA in the 6×6 μm^2 junction. The values of I_{c1} and I_{c2} almost double as the junction area doubles, suggesting that the changes are contributed by the junction itself. As shown in Figure 5-6 (a), when junctions were cooled down from 3.5 K to 300 mK, I_{c1} and I_{c2} did not change much, indicating that they are not sensitive to changes in temperature as long as it is well below the T_c of Nb. In contrast, they react very differently upon application of magnetic field. According to Figure 5-6 (b) and (c), I_{c2} is easily suppressed by a small in-plane field while I_{c1} is not sensitive. This suggests that the two critical currents have different origins which will be discussed later.

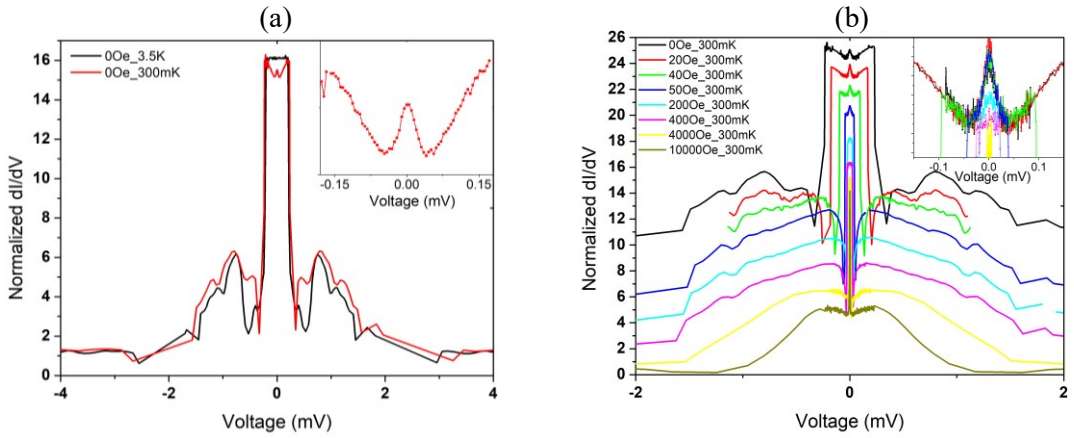

Figure 5-7: Differential conductance spectroscopies of the 4×4 μm^2 junction. The dI/dV values are normalized relative to the normal state conductance values above I_{c1}. (a) dI/dV-V curves at 3.5 K and 300 mK. The inset zooms in on the ZBCP which emerges at 300 mK. (b) dI/dV-V curves measured in a perpendicular magnetic field at 300 mK. Curves are offset for clarity. The inset zooms in on the ZBCP to show its behavior in magnetic fields.

By taking derivative of the I-V curves, we obtained the differential conductance (dI/dV) spectroscopies. The results were also verified with direct lock-in measurements. Figure 5-7 (a) compares dI/dV-V curves measured at 3.5 K and 300 mK. Figure 5-7 (b) shows the curves measured at 300 mK in various magnetic fields perpendicular to the substrate. There are three main features on

the dI/dV-V curves. First, they show a wide bump with some oscillations. The oscillation could be attributed to multiple Andreev reflection or McMillan-Rowell oscillations [133, 134]. The width of the bump is determined by the critical current I_{c1} as shown in Figure 5-6 (a), above which normal junction resistance dominates. In Figure 5-7 (b), we can see the bump width so as I_{c1} does not change in small perpendicular magnetic fields (H < 400 Oe). In larger field up to 1 T, the bump shrinks but is still present, which means I_{c1} survives in this large perpendicular field. By combining with information from I-V characteristics, we can see I_{c1} is fairly robust, not sensitive to temperature nor magnetic field. Therefore, we attribute I_{c1} to the critical value of Josephson supercurrent by direct coupling between the two Nb electrodes.

Second, at low bias voltage (~ 0.25 mV in Figure 5-7) there is a plateau, corresponding to a conductance enhancement below I_{c2} in the I-V curve. The conductance spectroscopy in Figure 5-7 (b) shows the plateau width quickly shrinks into a sharp spike at about 200 Oe, which means I_{c2} can be easily suppressed by a small perpendicular field. This behavior of I_{c2} is similar to that in small parallel field indicated by Figure 5-6 (b) and (c). Compared with I_{c1}, I_{c2} is very fragile. It is therefore attributed to the Josephson effect between the very sensitive, proximity-induced superconducting TI surfaces. As reported in the literature [81, 135], proximity-induced superconductivity on TI surfaces can develop at a temperature close to T_c of S, so we are able to start observing I_{c2} at 3.5 K. When this induced fragile superconductivity is destroyed by a magnetic field, the plateau on the dI/dV curve disappears. On the other hand, as the spike height at zero bias does not change much in higher field up to 1T, we regard it as contribution from the Josephson current between bulk Nb electrodes.

Third, when temperature further cools down to 300 mK, a small zero bias conductance peak (ZBCP) emerges at the center of the plateau as shown in Figure 5-7 (a). The ZBCP requires lower temperature to show up but is more robust in perpendicular field than the plateau. Figure 5-7 (b) we can see the plateau width starts to shrink in a very small field (H < 50 Oe), while the ZBCP does not change much. An obvious suppression of the ZBCP can be seen when H reaches 200 Oe. The dependence of ZBCP on temperature and field is shown in Figure 5-8 (a) and (b) respectively. The peak can survive up to 2000 Oe. This would exclude the contribution from the Al wire as the critical field for superconducting Al is only around 100 Oe [136].

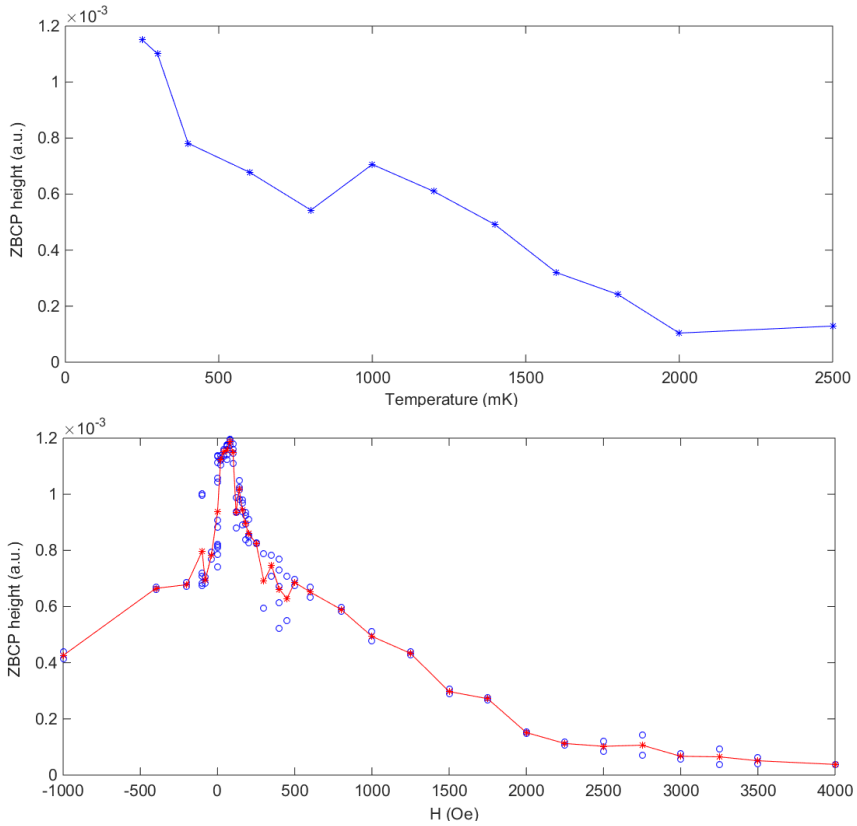

Figure 5-8: (a) Temperature dependence of the ZBCP height. (b) Magnetic field dependence of the ZBCP height. Blue points are experimental data. Red points are averaged data.

5.2.3 Discussion

Since the presence of a ZBCP is usually taken as a signature of the Majorana zero-mode, it has been reported and investigated extensively in various S-TI structures [12, 13, 48, 50, 81, 137]. The ZBCP observed by STM in the vortex cores at the Bi_2Te_3-$NbSe_2$ interface is a strong evidence for Majorana zero-mode [12, 13]. However, in this scenario one needs to first create vortex cores with a perpendicular magnetic field and their number should increase as the field increases. As the ZBCP in our observation showed up in zero magnetic field and decreased monotonically upon applying a perpendicular field, we can basically exclude the possibility that it comes from the Majorana zero-modes bound in vortex cores.

ZBCP has also been observed in different S-TI interfaces through transport measurements [48, 50, 81, 137]. However, the origin of ZBCP in these situations is more complicated because there can be many mechanisms contributing to it as we have mentioned. One possible mechanism is the formation of Andreev bound states between bulk Nb. Since the ZBCP in our observation only appears at very low temperature (300 mK) instead of developing immediately below T_c of Nb, we do not think Andreev bound states are causing our observation. Another possibility is that the bulk of TI is also induced to be superconducting. This mechanism has been claimed responsible for the ZBCP observed at the interface of Bi_2Se_3-$NbSe_2$ [81]. It has also been reported that a strong proximity effect can develop along the thickness direction of the Bi_2Te_3 crystal [135]. Considering the Fermi level in those Bi_2Se_3 and Bi_2Te_3 samples is lying inside conduction bands, it is reasonable that the bulk electrons played an important role in their observation. But in our case, we have demonstrated the Fermi level of BST is carefully tuned into bulk gap by regulating the chemical stoichiometry, supported by Hall measurements shown in chapter 4. Therefore, the insulating bulk of our BST film is not very likely induced into a superconducting state by proximity.

After ruling out these mechanisms, to the best of our knowledge, the ZBCP most possibly originates from a series of tiny Andreev bound states that form on the sidewall of the TI layer confined between the top and bottom superconducting layers, like a planar device being folded up. In this configuration, as we have analyzed in section 5.2.1, when there is a π phase difference, the Andreev levels will cross at zero energy to form counterpropagating chiral Majorana modes expected at the top and bottom edges of the sidewall. With the inherent π Berry phase shift for a closed loop, associated with the nature of TI, all these Andreev bound states have energies centered on zero (with one of them precisely at zero), and conductance through the most dominant states therefore collectively contribute to the ZBCP observed in our devices. However, we do not have the energy resolution to resolve individual bound states so the ZBCP that we observed may contain the integrated total contributions.

5.3 Conclusions

To conclude, motivated by predictions for existence of non-trivial Majorana states in a vertical S-TI-S junction, we grew Nb-BST-Nb sandwich structure by depositing a top layer of Nb on the BST-Nb heterostructures, and fabricated vertical Josephson junctions. The I-V and dI/dV-V characteristics of

these junctions were investigated at different temperatures and in various magnetic fields. There are several channels contributing to the conductance and leading to different features in the dI/dV spectroscopy. Josephson current between bulk Nb contributes to a bump and the non-vanishing sharp spike at zero bias on the dI/dV-V curve. The proximity-induced superconductivity on TI surfaces leads to a plateau which is fragile in magnetic field. A more robust ZBCP was observed on the plateau upon cooling down to 300 mK. The ZBCP could be contributed by tiny Andreev bound states formed on the TI pillar's side wall. However, limited by the energy resolution, whether the ZBCP is related to the long-expected Majorana state is still not confirmed. As the structure of vertical S-TI-S Josephson junction has not been studied much in literature, our experimental results provide further understanding beyond single S-TI interface. The growth and fabrication methods pave a way for further study and potential applications of devices based on various structures including S-TI, TI-S and S-TI-S in the future.

Chapter 6
Superconducting MgB_2 thin films and heterostructures

Before moving on to the BST-MgB_2 heterostructure, in this chapter the discussion will be focused on the growth of superconducting MgB_2 thin film which requires special care to achieve good film quality. We will show the enhancement in the film quality of MgB_2 grown in our system. Furthermore, we have grown fully epitaxial MgB_2-MgO-MgB_2 multilayer heterostructure and fabricated sandwich-type Josephson junctions whose performance supports that the thin films have superb quality. Similarly, we also achieved MgB_2-EuS-MgB_2 heterostructure with magnetic barrier EuS.

6.1 Introduction

The superconductivity of the binary metal MgB_2 was first discovered in 2001 [19, 138]. Since then, it has attracted significant research interests from both fundamental understanding and practical application aspects. Being a standard BCS (Bardeen–Cooper–Schrieffer) superconductor, bulk MgB_2 has the highest critical temperature with T_c = 39 K which is also the theoretic limit of the BCS superconductors at ambient pressure [19]. The superconducting T_c in BCS theory is proportional to phonon frequency. In MgB_2, the light mass of boron atoms enhances its phonon frequency thus enhances the T_c. The crystal structure of MgB_2 has boron atoms forming honeycombed layers and magnesium atoms locating above the center of the hexagons in between boron layers, shown in Figure 6-1. The corresponding lattice constants are a = 3.086 Å and c = 3.524 Å [19]. Similar to graphite, the in-plane B atoms are combined through strong σ-bonding within the honeycombed layer and adjacent layers are coupled through a weaker π-bonding. The phonon mode based on B-B vibrations couples strongly to the σ-bonding electronic states at the Fermi level whereas the coupling to the π-bonding states is much weaker, leading to the two different superconducting gaps with Δ_σ = 5 ~ 7 meV and Δ_π = 2 ~ 3 meV [139], which is a unique nature of MgB_2. This unique two-gap feature has been studied theoretically and confirmed by experiments [18, 140-149].

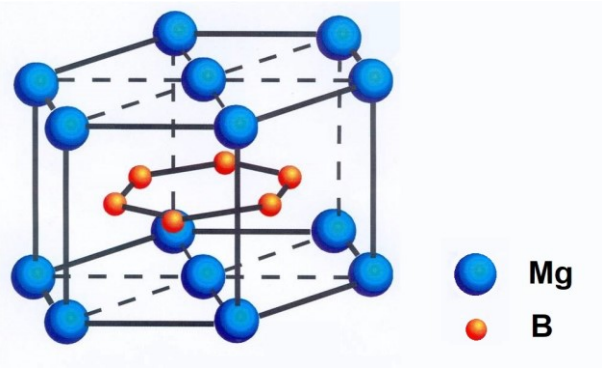

Figure 6-1: Crystal structure of MgB_2. Boron atoms form honeycomb planes, and magnesium atoms occupy the centers of the hexagons in between boron planes.

Its high T_c and large superconducting energy gap allow MgB_2 based superconducting electronics, such as Josephson junctions and superconducting quantum interference devices (SQUID), to operate at relatively higher temperatures ($\geqslant$ 20 K, more suitable for field operations) and higher speeds [150-153]. MgB_2 films also have very high critical current density on the order of 10^7 A cm^{-2} and high critical field up to 29 T [154]. These properties make MgB_2 a favorable candidate for superconductor applications. Moreover, with its hexagonal layered structure, MgB_2 is ready to be coupled with many layered hexagonal materials such as graphene and topological insulators. In this thesis, we attempted to grow $(Bi_{0.5}Sb_{0.5})_2Te_3$-MgB_2 heterostructure, hoping to induce superconductivity with larger gap on the topological surface states of $(Bi_{0.5}Sb_{0.5})_2Te_3$.

Many techniques have been developed to grow epitaxial (0001)-oriented MgB_2 thin films, such as hybrid physical-chemical vapor deposition (HPCVD) [155], co-sputtering [156] and pulsed laser deposition (PLD) [154, 157]. These techniques require either elevated substrate temperature or post-annealing at 700 - 850 °C with high Mg vapor pressure, which is not suitable for multilayer growth and device integration. MBE is able to achieve one step growth of MgB_2 films at a suitable low substrate temperature 150-320 ºC [158-163]. However, even within such a narrow growth window, the MgB_2 crystal quality still varies tremendously. One of the contributions of this thesis is to optimize epitaxial growth of MgB_2 films. We used *in situ* RHEED as well as *ex situ* XRD to demonstrate our films are epitaxial with clear in-plane orientation. We further proceeded to grow fully epitaxial MgB_2-MgO-MgB_2 heterostructures, with MgB_2 are (0001) and MgO are (111)

orientated. Sandwich-type Josephson junctions were fabricated by photo-lithography. These junctions exhibit clear Fraunhofer patterns, demonstrating good barrier uniformity. Furthermore, we observed clear Fiske steps in the I-V characteristics of these junctions, which are caused by interactions of the ac Josephson effect with the intrinsic electromagnetic cavity modes of the junctions that form sandwiched transmission line geometry) [164-167]. Magnitudes of the Fiske steps oscillate periodically with applied magnetic fields, well matching the expected behavior.

6.2 MBE growth and characterization of MgB_2 thin films and heterostructures

6.2.1 Growth of MgB_2 thin films

Growth of *c*-axis or (0001) orientated MgB_2 is desired to be compatible with the hexagonal lattice of $(Bi_{0.5}Sb_{0.5})_2Te_3$ for the purpose of epitaxial heterostructure. With the lattice constant a = 3.086 Å, MgB_2 films are able to be epitaxial on *c*-cut sapphire (a = 4.765 Å) through 30º in plane rotation [168, 169], as well as on Si(111) substrate with MgO (a = 4.211 Å) buffer layer [170]. MgB_2 has a lattice mismatch of -35% referred to sapphire along the $[11\bar{2}0]$ axis, which is unfavorable for epitaxial growth. A 30º in-plane rotation of the $[11\bar{2}0]$ direction of the MgB_2 film with respect to the substrate results in a parallel orientation of $[11\bar{2}0]$ MgB_2 and $[10\bar{1}0]$ sapphire. This provides a lattice mismatch of ~ 9%.

Detailed studies on the influence of growth conditions including substrate temperature and flux ratio of Mg:B during MBE growth are discussed in [171]. According to both the previous studies and to our own experience, high Mg flux is necessary and substrate temperature has very narrow window. After investigations on different substrates including Si (111), Si (100) and *c*-cut sapphire, we found that the best epitaxial films were achieved on Si (111) with a thin (111)-MgO epi-buffer layer. Therefore, we will focus our following discussions mainly on (111)-Si substrates. Si wafers were etched by 10:1 BOE solution or 1% HF solution to remove the native oxide and to form a hydrogen passivated surface. The growth was undertaken in the metal MBE chamber described in chapter 3. To prevent the formation of Mg-Si alloy, prior to the growth of MgB_2, 5 nm MgO was deposited as a buffer layer with electron-beam evaporation with substrate temperature at 300 °C. The substrate temperature was then lowered to the desired values for epitaxial MgB_2 growth. Various growth temperatures were attempted, and the optimum was found to be 240 ºC in our system, calibrated with

surface-mount thermocouple to the substrates' surface. Mg (99.99%) was evaporated from a Knudsen cell (k-cell) with a PBN crucible. Mg flux was maintained at 2 Å/s by regulating the k-cell source temperature within 390 ºC ~ 410 ºC. Electron beam evaporation was adopted for B due to its very high evaporating temperature (~ 1800 ºC). B (99.5%) was contained within a graphite crucible to avoid contamination and its flux rate was kept at 0.2 Å/s, monitored in real-time by QCM. The growth rate of MgB_2 film was dominated by the rate of B. RHEED patterns generated with 15 KeV high energy electron beams were collected before, during and post growth to investigate the surface quality of substrates as well as the deposited films.

Figure 6-2 shows a set of RHEED patterns at different stages of the optimal growth. Our as-grown MgB_2 films showed streaky RHEED patterns instead of spotty patterns reported in earlier work [172, 173], demonstrating significant improved surface smoothness. The rotational symmetry and in-plane crystal orientation of the films was further examined by RHEED with various beam incidence angles. Two distinct RHEED patterns alternate themselves when the azimuthal angle rotates every 30º. The spacing between streaks (W) is reciprocal to the spacing between rows of atoms (d) on the 2D hexagonal lattice. W and d are connected by $d = \lambda L/W$, where L is the distance between the RHEED screen and the sample, λ is the wavelength of the incident electron beam. As shown in Figure 6-2, when the incidence direction rotates from $[10\bar{1}0]$ to $[11\bar{2}0]$, the spacing between streaks changes from W_1 to W_2, where $W_1 \cong \sqrt{3}W_2$ (corresponding to $d_2 \cong \sqrt{3}d_1$) as expected. In addition, the X-ray diffraction result show in Figure 6-3 is consistent with RHEED, showing only reflection peaks from the plane family of {000l} MgB_2 peaks in addition to the substrate peaks, indicating a phase-pure *c*-axis oriented MgB_2 film. The six-fold symmetry from XRD 360º Φ scan on the $\{10\bar{1}1\}$ planes supports the MgB_2 films being also in-plane oriented, i.e., fully epitaxial. In addition to the crystalline quality, the superconducting transition of a 50 nm MgB_2 film was measured to be $T_c = 36$ K with $\Delta T <$ 1 K, shown in Figure 6-2 (e). It is lower than the T_c = 39 K of bulk material, which is reasonable considering the small thickness.

The substrate temperature is critical for the cystallization of MgB_2. We carefully investigated the growth at various substrate temperatures. The substrate was heated through radiation heating from a noncontact heater (SiC). As a result, the actual substrate temperature can be different from the set point, depending on many factors that may affect radiation absorption, including substrate type as

well as the thickness and absorption coefficient of the prior deposited films. On the other hand, the quality of MgB_2 is very sensitive to the changes in substrate temperature caused by these subtle differences. Therefore, in addition to the calibrations from substrate-mounted thermocouples, we extensively referred to the *in situ* RHEED patterns to determine the real-time surface condition which can also reveal the true surface temperature.

The crystallization of MgB_2 happened in a Mg-rich enviroment. Because of the high flux rate of Mg, the substrate has to be maintained at higher than a critical temperature so that excess Mg can not physically condense onto the substrate unless it chemically reacts with B to form MgB_2. We found the critical teperature for Mg condensation to be around 235 ºC in our system, by deopositing only Mg at different temperatures. The saturation Mg vapor pressure is around 5×10^{-7} torr at this temperature [174], roughly corresponding to a Mg impingement rate of 1 monolayer/sec in equilibrium with the vaporization rate. The Mg flux we sent in our system is on the same order of magnitude as this equilibrium vaporization rate, therefore at lower than this temperature, we can expect a large amount of excess Mg reaching and condensing on the surface because deposition > vaporization; at higher than this temperature however, Mg will vaporize right away unless they become chemically bound to the surface with B (forming MgB_2). This becomes a self-limiting process. According to our obervation, Mg droplets indeed formed below 235 ºC, evidenced with spotty RHEED patterns (indicating poly 3D growth) appearing in less than 1 min after the deposition starts, see Figure 6-4 (a), wheares when the substrate temperature was raised to 235 ºC (Figure 6-4 b), such RHEED patterns did not show up throughout the growth, demonstrating the absence of Mg droplet formation. After identifying this critical temperature by sending only Mg flux, we used it as a reference for growing MgB_2. As comparison to the optimal reults of MgB_2 grown at 240 ºC, Figure 6-4 (c) shows the RHEED paterns of MgB_2 films grown at 230 ºC which lower than the critical temperature. The spotty RHEED patterns taken at the beginning of growth clearly indicates existence of Mg droplets and the final 30 nm MgB_2 film (Figure 6-4 d) has much lower crystalline quality compared with that in Figure 6-2. The poorer crystalline film with excess Mg has a lower superconducting transition temperature (~ 26 K at 50 nm). Although this is still a relatively high T_c compared with other BCS superconductors, the film degraded very fast under ambient enviroment due to the reactivity of excess Mg with oxygen and moisture, making it not applicable. Moreover, Mg droplets are volatile during certain device fabrication steps, especially the ion milling procedure when the substrate is locally

heated by ion bombardment, leaving lots of deffects in the patterned junctions. Excess Mg could explain some reports in the literature with seemingly good supercondcuting behavior yet very poor device performance. Thus it is important to eliminate excess Mg in the film deposition. As mentioned before, the optimal substrate temperature producing the highest quality of MgB_2 films in our system is around 240 ºC, barely above the critical temperature to get rid of Mg condensation.

Clearly, such optimal temperature depends sensitively on the chosen Mg flux: larger Mg flux will require higher optimal temperature. Lowering Mg flux is therefore an efficient way of reducing the sample deposition temperature, yet it cannot go too low as a larger-than-needed Mg flux is required in order to reduce the thermodynamic equilibrium concentration of Mg vacancies. On the other hand, higher substrate temperature can enhance the final crystal quality but also calls for larger and larger Mg flux, posing a practical challenge for a given system. When the Mg flux is not sufficient, MgB_2 becomes highly defective instead and even losing the desired crystal structure. With our Mg flux fixed, we attempted growth at various increased temperatures. It turns out the MgB_2 films deposited at 260 ^{o}C became (0001)-textured, losing its in-plane orientation (Figure 6-4 e). The RHEED patterns showed mixed diffractions from both $[11\bar{2}0]$ and $[10\bar{1}0]$ directions and did not change upon azimuthal rotation. The films grown at 280 ^{o}C were completely poly-crystalline (Figure 6-4 f). For deposition temperature higher than 320 ^{o}C, the films were amorphous and not superconducting at all. By comparing the RHEED results in Figure 6-4 with those in Figure 6-2, we can see that small temperature difference can make a big difference in the outcome. In addition, we also tried growth on different substrates at the optimized conditions. MgB_2 films on Si (100) and on *c*-cut sapphire are both highly textured without in-plane orientation (Figure 6-5), similar to the results Figure 6-4 e. This revealed that Si (111) with (111)-MgO buffer is the preferred substrate among these substrates we tested.

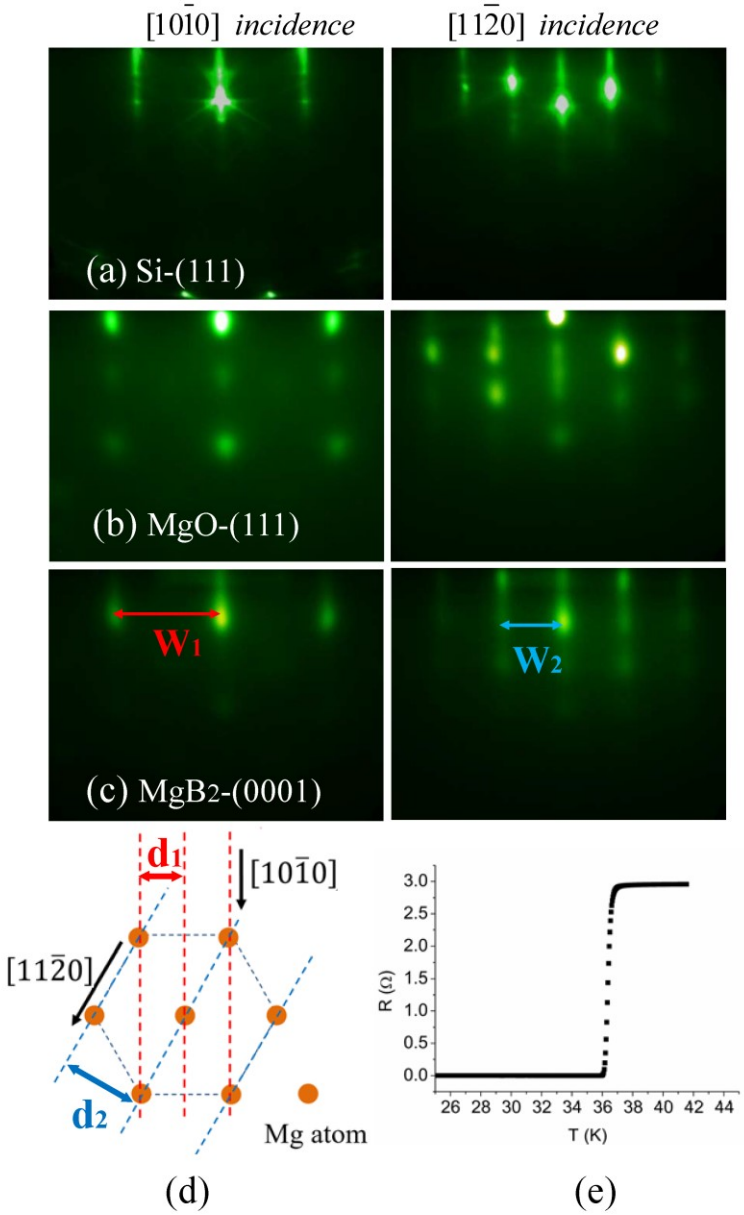

Figure 6-2: (a)-(c) RHEED patterns taken at different stages during the growth of an epitaxial MgB_2 film. Figures on the left column are taken with electron beam incident along $[10\bar{1}0]$ and those on the right column are taken along $[11\bar{2}0]$ after the substrate being rotated 30° azimuthally. (d)

Schematic illustration for electron beam incidence relative to the surface lattice. (e) Superconducting transition of the 50 nm MgB_2 film. T_c = 36 K with $\Delta T < 1$ K.

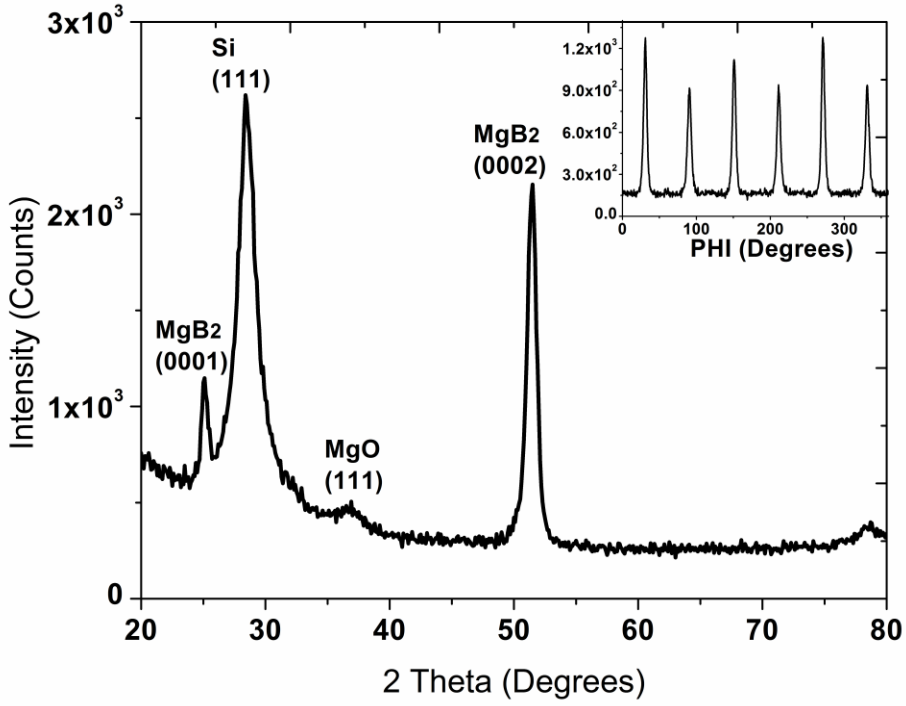

Figure 6-3: Coupled θ-2θ XRD scan of MgB_2 film grown on MgO buffered Si (111) at 240 ºC. A 2º offset was applied to the ω axis to avoid the strong satellite peaks from Si. The upper right inset shows the 360º azimuthal Φ scan targeting reflections from MgB_2 $\{10\bar{1}1\}$ planes.

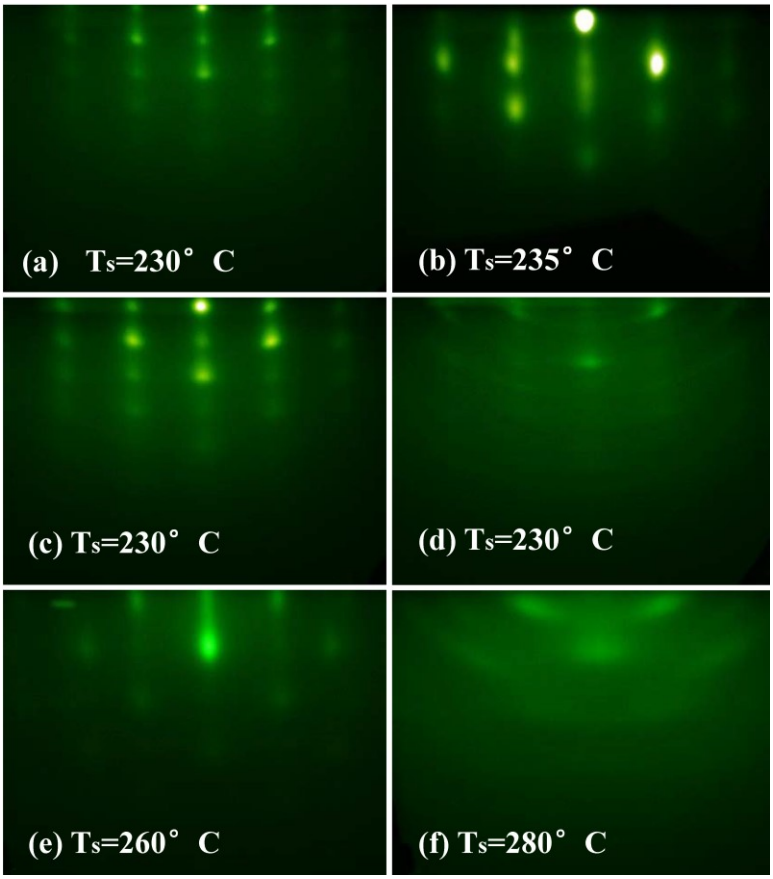

Figure 6-4: (a) Test deposition of only Mg at T_s = 230 ºC. The spotty patterns characterize formation of Mg droplets at this substrate temperature. (b) Test deposition of only Mg after raising T_s to 235 ºC with Mg source opening. Mg cannot stick to the substrate hence RHEED patterns are from the MgO surface, which is the buffer layer on the Si wafer. (c) Beginning of growth of MgB_2 at T_s = 230 ºC, within 1min after both Mg and B sources open. The spotty patterns signal excess Mg formation at the beginning of growth. (d) 30 nm MgB_2 grown at T_s = 230 ºC, poor crystalline quality due to excess Mg incorporation during the growth. (e) 30 nm MgB_2 grown at Ts = 260 ºC, a highly *c*-axis textured film without preferred in-plane orientation. The pattern shows mixed diffractions from both $[11\bar{2}0]$ and $[10\bar{1}0]$ reflections and does not change upon azimuthal rotation. (f) 30 nm MgB_2 grown at T_s = 280 ºC, the pattern becomes thicker and tends to show polycrystalline features.

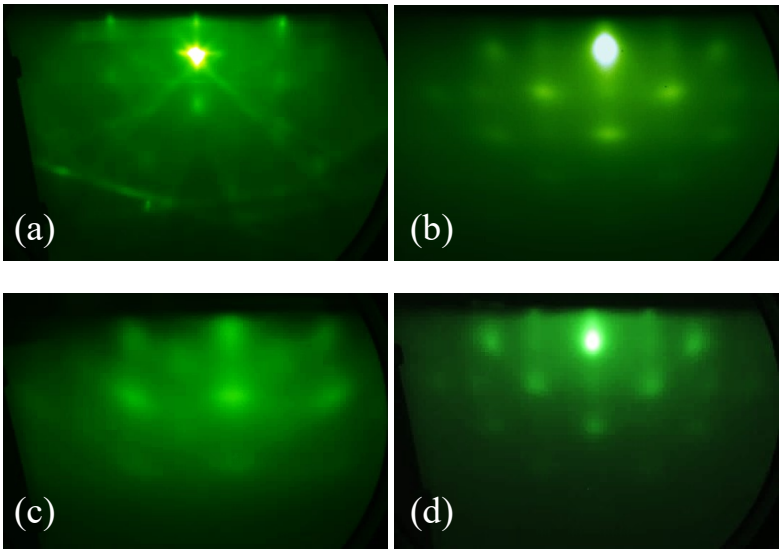

Figure 6-5: RHEED patterns of (a) *c*-cut sapphire (b) MgB_2 film grown on sapphire (c) MgO buffer grown on Si (100) (d) MgB_2 film grown on MgO-Si(100)

6.2.2 Growth of fully epitaxial MgB_2-MgO-MgB_2 heterostructure

Sandwich-type superconductor-insulator-superconductor (S-I-S) Josephson junctions are widely applied in superconducting circuits while the high T_c makes MgB_2 promising for Josephson junction applications. Multilayer MgB_2 heterostructures with smooth interface and pin-hole free barrier is the prerequisite for high performance of MgB_2 Josephson junctions. MgO has been proven to be a good barrier in magnetic tunneling junctions and has also been used as barrier in MgB_2 Josephson junctions [175-179]. Here in this project, after optimizing the growth conditions for single layer MgB_2 thin film, we proceeded to grow (0001)-MgB_2 / (111)-MgO / (0001)-MgB_2 hetero-epitaxial structures and fabricated Josephson junctions. We will show the growth and characterization of this multilayer structure in this subsection and discuss the device behavior in next section.

After deposition of 30 nm epitaxial MgB_2 bottom layer at 240 ºC as we mentioned earlier, the substrate was cooled down to room temperature to grow 1 nm MgO tunnel barrier with e-beam evaporation. Lower growth temperature yields a more uniform, pinhole-free barrier. The RHEED patterns in Figure 6-6 shows (111)-oriented MgO was well epitaxially grown on the MgB_2 layer. Subsequently, the substrate temperature was raised to 230 ºC for the top MgB_2 film deposition. It is

worth noting that the temperature set point for growing the top MgB_2 layer needs to be slightly lower than that for the bottom layer in our system. The reason for this difference is related to our system's radiation heating method, which we have also discussed for the deposition of BST-Nb heterostructure. The existing bottom MgB_2 film absorbs some infrared radiation that was originally transparent through Si hence slightly increases the actual surface temperature under the same heating power. Such surface temperature cannot be well calibrated with infrared thermometers as a significant portion of the heater infrared radiations can pass through the Si wafer. Instead, with RHEED we can readily identify the optimal growth temperature for the top layer using the same principles described earlier, namely use solely Mg flux to find a critical temperature above which the growth temperature should be slightly higher. The surface temperature is critical for condensing the first few atomic layers of MgB_2 on a hetero-surface (MgO), subsequently it affects much less once MgB_2 crystal structure is successfully settled. This explains why the growth of bottom layer was not ruined by the gradually increasing surface temperature as the film grows. For the top layer MgB_2, the increase in substrate surface temperature (due to coverage of the bottom layer) must be compensated by correspondingly lowering the heating power to achieve the ideal growth condition. Figure 6-6 (c) and (d) compare the growth results of the top MgB_2 layer when substrate temperature was set to be 230 ºC and 240 ºC. Obviously, the top layer was poorly crystalline if the substrate was set to the same temperature for the bottom layer deposition (240 ºC). Finally, the whole stack of films is cooled down to room temperature, and capped with 10 nm Ti and 50 nm Au as protection, before proceeding to micro-fabrications.

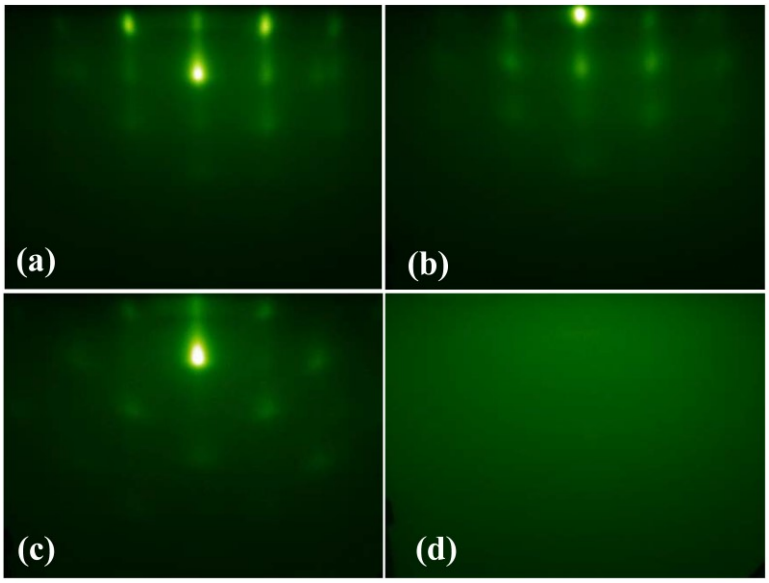

Figure 6-6: Multilayer growth of (0001)-MgB_2 /(111)-MgO/(0001)-MgB_2. (a) 30 nm bottom MgB_2 grown at T_s = 240 ºC; (b) 1 nm MgO barrier grown at room temperature; (c) 30 nm top MgB_2 if grown at T_s = 230 ºC; (d) 30 nm top MgB_2 if grown at T_s = 240 ºC.

6.3 MgB_2-MgO-MgB_2 tunneling Josephson junction

The fully epitaxial MgB_2-MgO-MgB_2 heterostructure were micro-fabricated into Josephson junctions following standard photolithography and ion milling techniques described in chapter 3, section 3.4. In this section, after reviewing the basic properties of a general sandwich-type Josephson junction, we will show the measurement results of our MgB_2-MgO-MgB_2 junctions.

6.3.1 Josephson effect in an S-I-S junction

The Josephson effect, predicted by Brian D. Josephson in 1962 [180], can be observed in two weakly coupled superconductors in the form of S-I-S junction, S-N-S junction, superconducting weak link or point contact, as long as there is a probability for Cooper pairs in one superconductor transfer to the other. This subsection reviews the basic properties of the S-I-S Josephson junctions.

It is well known that in an N-I-N junction, electrons in the normal metal electrodes can tunnel through the thin insulating barrier with certain probability *p*. For an S-I-S junction with two superconductor electrodes S_1 and S_2, Josephson discovered that the Cooper pairs in the

superconductors can tunnel coherently through the barrier with the same probability *p*. When the current density flowing across the junction is smaller than the critical Josephson current density J_c, it is supercurrent carried by Cooper pairs without any voltage drop. The supercurrent density J_s is related to the phase difference across the junction by *current-phase relation*,

$$J_s = J_c \ sin\,\varphi \qquad \text{(First Josephson equation)}$$

where φ is the phase difference across the junction. In the absence of any electric and magnetic field, $\varphi = \theta_2 - \theta_1$, which is just the phase difference between the two superconductors. The critical Josephson current density J_c decays exponentially with increasing of barrier thickness *d*

$$J_c \propto exp\,(-2\kappa d)$$

and κ is the characteristic decay constant, determined by the barrier property. When the current density exceeds J_c, only part of the current can be carried by Josephson supercurrent, therefore normal electrons will be involved to conduct current and contribute finite resistance, so that there will be a voltage drop *V* across the junction. The phase difference and voltage drop are related by the *voltage-phase relation*,

$$\frac{\partial\varphi}{\partial t} = \frac{2\pi}{\Phi_0}V \qquad \text{(Second Josephson equation)}$$

where $\Phi_0 \equiv \frac{h}{2e} = 2.068 \times 10^{-15}$ Vs, is the flux quantum. In the finite voltage state, the phase difference φ evolves with time linearly as

$$\varphi(t) = \varphi_0 + \frac{2\pi}{\Phi_0}V \cdot t$$

Thus, the Josephson current $I_s = I_c \sin \varphi(t)$ is oscillating with time at the Josephson frequency ν,

$$\frac{\nu}{V} = \frac{1}{\Phi_0} = 483.6\ \frac{\mathrm{GHz}}{\mathrm{mV}}$$

The Josephson junction can be used as a voltage-controlled oscillator to generate high frequency microwaves.

6.3.2 Fraunhofer pattern - quantum interference effects of a Josephson junction in applied magnetic field

According to the Josephson equations, the supercurrent flowing across a Josephson junction is related to the phase difference across the junction. At $V = 0$ state and in the absence of magnetic field, the phase difference $\varphi = \varphi_0 = \theta_2 - \theta_1$ is a constant. In the presence of an external magnetic field, the phase difference will change in space, causing spacial distribution of the Josephson current. Consider a rectangular junction with dimension L_x and L_y, and current is flowing in z direction, as shown in Figure 6-7. A magnetic field $\mathbf{B} = B\,\hat{y}$ is applying along y direction. The magnetic field can penetrate through the barrier and into the superconducting electrodes up to the London penetration depth λ_{L1} and λ_{L2}. Analysis based on integration of the vector potential over a close contour across the junction [181] yields

$$\frac{\partial \varphi}{\partial x} = \frac{2\pi}{\Phi_0} B \cdot (d + \lambda_{L1} + \lambda_{L2})$$

Integration along x gives

$$\varphi(x) = \frac{2\pi}{\Phi_0} B \cdot (d + \lambda_{L1} + \lambda_{L2}) \cdot x + \varphi_0$$

Following the current-phase relation, the current density in x-y plane can be written as

$$J_s(x,y) = J_c(x,y) \sin\left(\frac{2\pi}{\Phi_0} B \cdot (d + \lambda_{L1} + \lambda_{L2}) \cdot x + \varphi_0\right)$$

Assume the barrier is uniform so that the current density is uniformly distributed in x-y plane, $J_c(x,y) = J_c$, one can get the total current by integrating the current density

$$I_s(B) = \iint J_s(x,y)\,dxdy = J_c L_y \int \sin\left(\frac{2\pi}{\Phi_0} B \cdot (d + \lambda_{L1} + \lambda_{L2}) \cdot x + \varphi_0\right) dx$$

$$I_s(B) = I_c \left| \frac{\sin\left(\frac{\pi\Phi}{\Phi_0}\right)}{\frac{\pi\Phi}{\Phi_0}} \right|$$

where $\Phi = B \cdot L_x \cdot (d + \lambda_{L1} + \lambda_{L2})$ is the total flux penetrating the junction and $I_c = J_c \cdot L_x \cdot L_y$. This $I_s(B)$ dependence is equivalent to the optical ***Fraunhofer diffraction pattern*** through a single slit,

as shown in Figure 6-7 (b). One would notice that a uniform barrier is required to observe the Fraunhofer pattern in a Josephson junction, as J_c decays exponentially with increasing of barrier thickness. If the supercurrent density varies in the junction's *x*-*y* plane or it is flowing through small pinholes in the tunneling barrier, no Fraunhofer diffraction pattern can be observed. Therefore, observation of Fraunhofer pattern is usually used as a direct proof of a uniform junction.

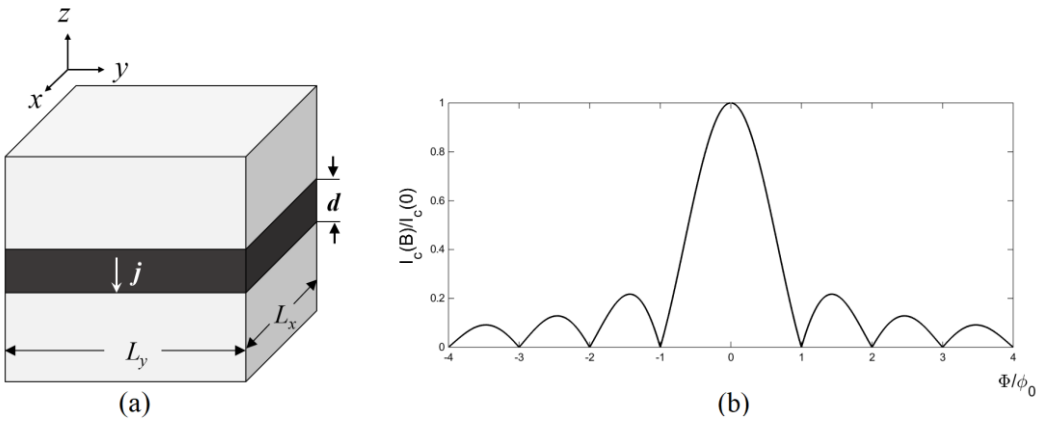

Figure 6-7: (a) An S-I-S Josephson junction. Current is flowing along *z* direction. (b) Simulated Fraunhofer pattern: critical current of the Josephson junction is oscillating with in-plane magnetic flux.

6.3.3 Measurements on MgB_2-MgO-MgB_2 Josephson junction

Measurements on our MgB_2-MgO-MgB_2 Josephson junction were performed in a liquid He_4 continuous flow cryostat to reach 4.2 K. Sandwich-type Josephson junctions of area 4 μm ×4 μm, 6 μm ×6 μm, 8 μm ×8 μm and 8 μm ×16 μm were measured. Thickness of the MgO barrier is 1 nm. The bottom and top MgB_2 electrodes are 30 nm thick. At zero magnetic field, the I-V characteristics of junctions with different sizes are reproducible and consistent with previous reports [179, 182-185]. We will focus our discussion on the junction with area 8 μm ×16 μm and look at its field performance. Figure 6-8 shows the I-V curve of the Josephson junction. The non-hysteresis suggests this junction is overdamped due to its small resistance and small capacitance. According to the I-V curve, the critical Josephson current at zero magnetic field is about 0.33 mA, corresponding to a critical current density $J_c \cong$ 260 A/cm^2. Product of I_cR_N is estimated to be 1 meV. This value is higher than those in reference [183], but still small compared with the calculated value (~ 4 meV) [186],

which is partly caused by the reduction of T_c (< 39 K) when the MgB_2 film is thin. The nonlinearity of the I-V curve at higher voltages comes from the non-constant tunneling resistance, which is also present in earlier reported works when the barrier is thin [151, 172, 183, 187]. An in-plane magnetic field was then applied perpendicularly to the short edge with length l = 8 μm and the magnetic field dependence of the critical current showed a clear Fraunhofer pattern with a period of ΔH = 70 Oe, see Figure 6-9. The Josephson penetration depth can be estimated to be $\lambda_J = \mathrm{sqrt}\left(\frac{\Phi_0}{2\pi\mu_0 s J_c}\right) \cong 60$ μm, where $s = d + 2\lambda_L$ and d is the barrier thickness. Because the MgB_2 electrode's thickness is smaller than the London penetration depth ($\lambda_L \cong 40 \sim 100$ nm for MgB_2) [182, 188], where s is the sum of barrier thickness and both MgB_2 electrodes thickness. We see that l is much smaller than λ_J, so the junction can be treated as a small junction with uniform field distribution and the penetrating flux is $\Phi = Bls$. The red curve in Figure 6-9 is theoretically simulated based on the above parameters, fitting well with the experimental result.

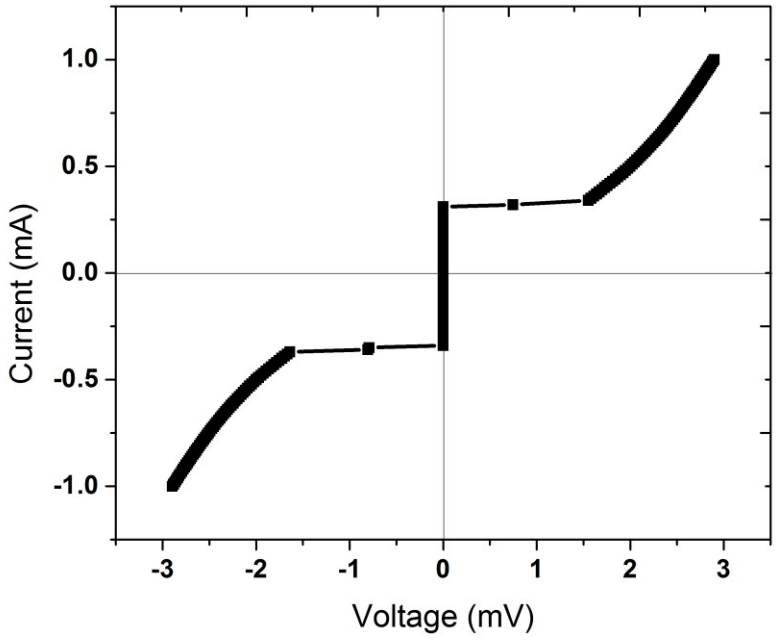

Figure 6-8: I-V curve of MgB_2-MgO-MgB_2 Josephson junction measured at 4.2 K. Junction area is 8 μm × 16 μm.

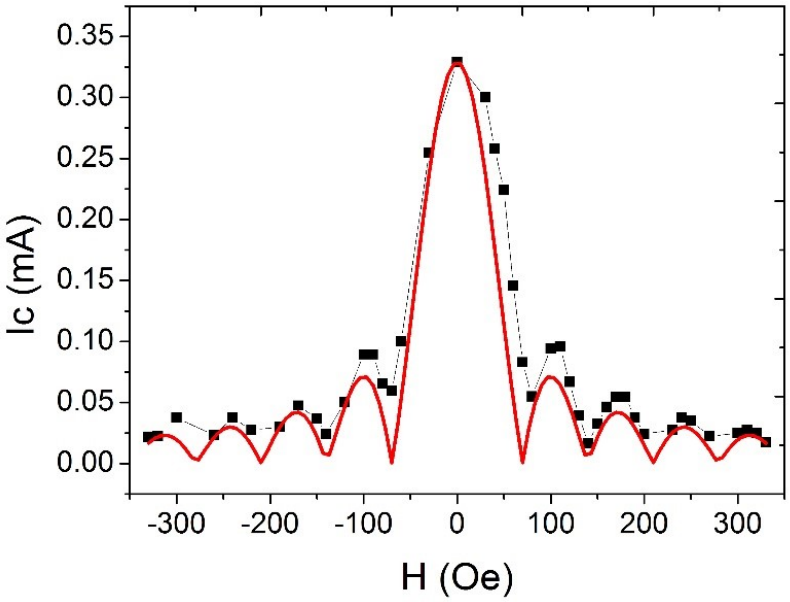

Figure 6-9: Magnetic field dependence of the Josephson critical current exhibit a clear Fraunhofer pattern, with period ΔH = 70 Oe. Red curve is a theoretical fitting.

In addition to the modulation of critical current, the I-V characteristics also clearly showed a series of steps when the magnetic field varied from -350 Oe to 350 Oe. Both the I-V curve and the dI/dV-V curve in Figure 6-10 indicate that these steps happen at voltages that are multiples of 0.18 meV, i.e., $V_n = n \cdot 0.18$ meV, where n is an integer. They are identified as Fiske steps, resulting from the Josephson effect in resonance with the junction's own cavity modes. According to the Josephson equations, when the junction is under finite voltage bias V, the Josephson current is oscillating at the Josephson frequency $\omega_J = 2\pi\nu = \frac{2\pi}{\Phi_0}V$. On the other hand, with a dielectric layer separating two superconductor planes, the junction can be regarded as an open ended transmission line with the resonant frequency $\omega_n = \frac{n\pi\bar{c}}{l}$ of the n-th cavity modes, where $\bar{c} = c\sqrt{t/\varepsilon_r s}$ is the effective wave

velocity in the transmission line, ε_r is relative dielectric permeability and c is light velocity in free space [189]. The standing wave voltage pattern for the n-th mode in the cavity is

$$v_n(x,t) = A_n e^{j\omega_n t}\cos\frac{n\pi x}{l}$$

The resonant modes can be excited by the electromagnetic power with frequency ω_J radiated by the Josephson current into the junction. When ω_J matches ω_n of one of the modes, a zero-frequency current will appear and show as a series of DC current steps in the I-V characteristic at well-defined voltages

$$V_n = \frac{\hbar}{2e}\omega_n = n\Phi_0\frac{\bar{c}}{2l}$$

In order to have a stronger interaction with the resonant modes, the Josephson current must be spatially modulated in x direction to match the standing wave in the cavity, which can be achieved by applying a magnetic field in y direction for small junctions ($l \ll \lambda_J$). Similar to the field dependence of Fraunhofer patterns, the amplitude of the n-th Fiske step is also a periodic function of magnetic fields. This modulating function has a well-defined form,

$$F_n^2(\phi) = \begin{cases} \left\{\dfrac{2\phi\cos(\pi\phi)}{\pi\left[\phi^2 - \left(\frac{n}{2}\right)^2\right]}\right\}^2, & n = 1,3,5,\ldots \\ \left\{\dfrac{2\phi\sin(\pi\phi)}{\pi\left[\phi^2 - \left(\frac{n}{2}\right)^2\right]}\right\}^2, & n = 2,4,6,\ldots \end{cases}$$

where $\phi = \Phi/\Phi_0$ [189]. We can see that the magnetic field dependence of Fiske step amplitudes will have the same periodicity as the Fraunhofer patterns. There should also be a half-period offset between the odd and even steps.

According to the I-V curves measured in various magnetic fields, shown in Figure 6-10, up to 3 orders of Fiske steps were observed and the amplitudes of each Fiske step were indeed oscillating with applied magnetic field H. Figure 6-11 shows the field dependence of each step amplitude, where we can see the periodicity ΔH = 70 Oe, the same as that in the Fraunhofer patterns. Furthermore, it also shows the field modulations of even and odd steps are out of phase, i.e., maxima of even steps

occur at fields giving minima of odd steps. All of these experimental results agree well with theories. Both the clear Fraunhofer pattern and Fiske steps indicate superb quality of the MgB_2-MgO-MgB_2 heterostructure.

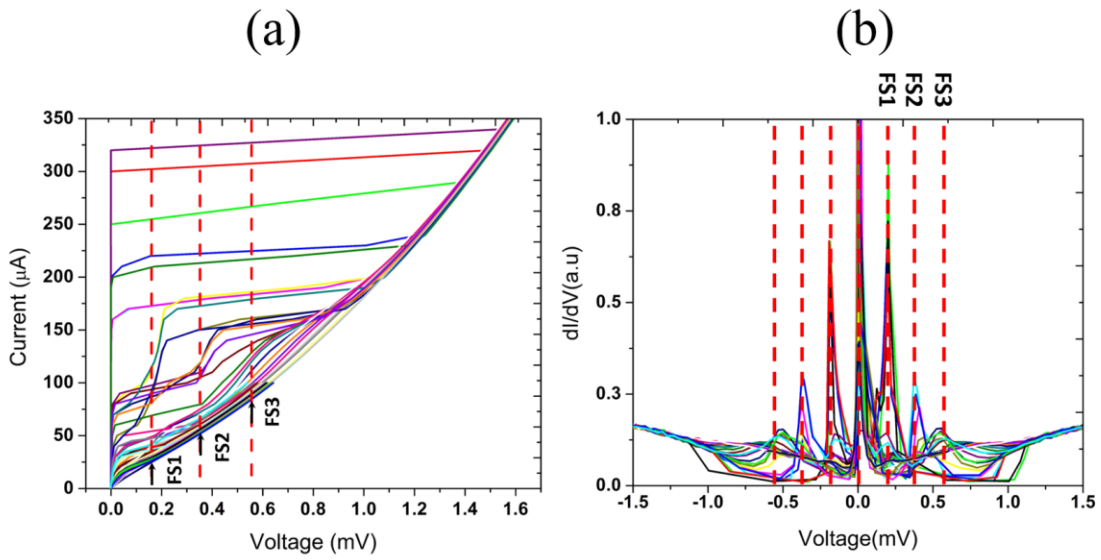

Figure 6-10: (a) Fiske steps in a series of I-V curves. I-V curves measured at various magnetic fields from -350 Oe to 350 Oe are distinguished by different colors. (b) The derivative curves of dI/dV-V, where Fiske steps are identified as the local maxima. The red dashed lines are for eye guidance to mark the voltage positions where the steps occur.

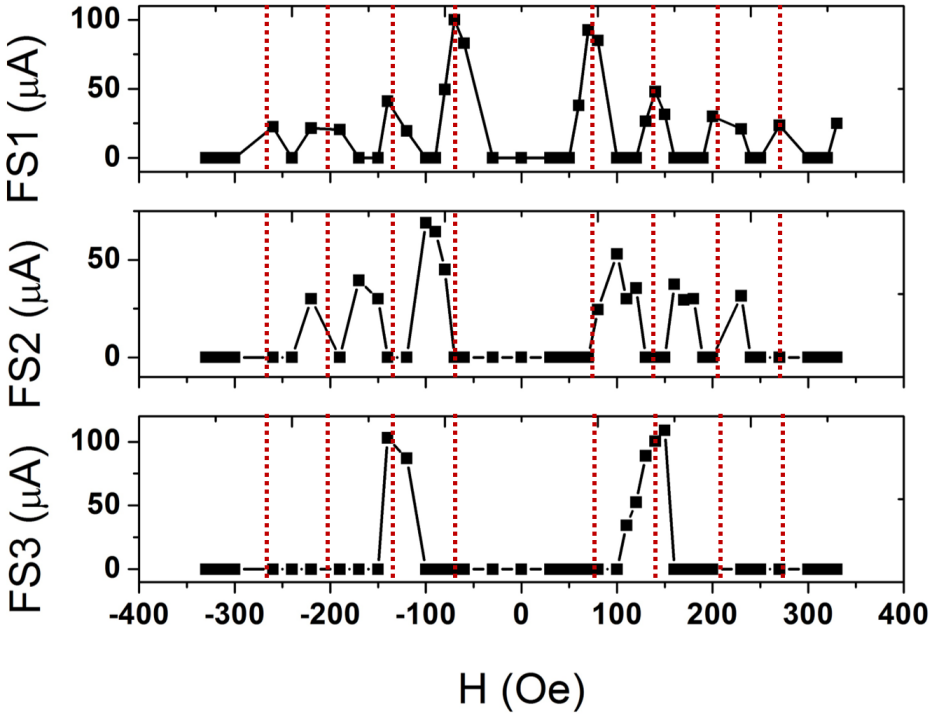

Figure 6-11: Magnetic field dependence of the step amplitudes for the 1st, 2nd, and 3rd order Fiske steps. Modulations of odd and even orders of step are out of phase, that is, maxima of odd steps occur at fields giving minima of even steps.

6.3.4 EuS-MgB_2 heterostructure

In chapter 4, we have shown successful growth of EuS-BST heterostructure and observed ferromagnetic order induced on BST surfaces. Since superconductor is the next ingredient to be added for realizing a system that can hold Majorana mode, we explored the MBE growth of EuS-MgB_2 heterostructure as well as MgB_2-EuS-MgB_2 multilayer and fabricated Josephson junctions.

After the deposition of *c*-axis oriented bottom MgB_2 film on MgO buffered Si (111) substrate, EuS was grown at room temperature on top of MgB_2 by e-beam evaporation from EuS powder source. RHEED pattern in Figure 6-12 (b) shows that EuS was single crystallized. To grow MgB_2-EuS-MgB_2 heterostructure, as we have discussed when growing MgB_2-MgO-MgB_2, the set temperature for top layer MgB_2 needed to be lower than the bottom MgB_2 (240 ºC) due to temperature elevation caused by existing films on the substrate. Here for the growth of MgB_2 on EuS, the temperature needed to

further go down to 210 ºC, 20 ºC lower than the growth temperature (230 ºC) for the top layer in the MgB_2-MgO-MgB_2 structure. This adjustment was necessary to get good film quality. In addition to the reason discussed earlier, this difference might be caused by the different surface energy between EuS and MgO. Figure 6-12 (c) and (d) show the RHEED pattern of top MgB_2 on EuS along $[10\bar{1}0]$ and $[11\bar{2}0]$ incidence, demonstrating the film was epitaxial. Based on the multilayer thin film, MgB_2-EuS-MgB_2 Josephson junctions were fabricated and measured at 4.2 K. The junctions exhibited typical I-V characteristics of Josephson current. Figure 6-12 (a) shows the I-V curve of junction with junction size 8 μm ×16 μm and EuS thickness was 1.5 nm. The critical current I_c is about 1.2 mA. The I_cR_N product is about 4.9 mV, comparable to the value of $2\Delta_\pi$ of MgB_2 gap. The observation of Josephson effect in vertical MgB_2-EuS-MgB_2 junctions supports that EuS-MgB_2 heterostructure has good quality.

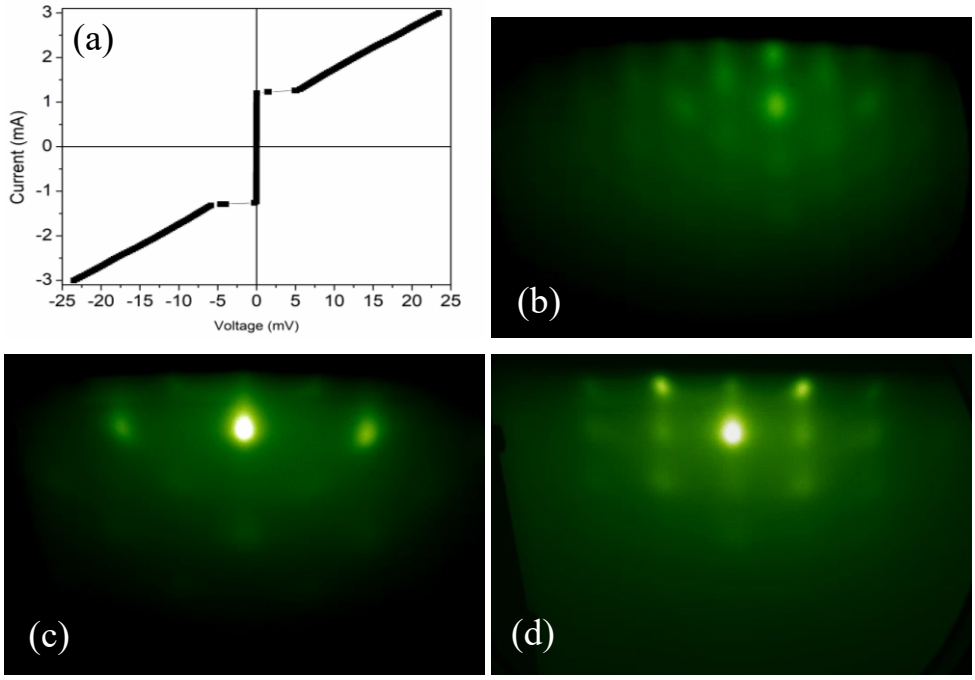

Figure 6-12: (a) I-V curve of an MgB_2-EuS-MgB_2 Josephson junction. (b)-(d) RHEED patterns during growth of MgB_2-EuS-MgB_2 heterostructure. (b) EuS barrier (c) top MgB_2 at $[10\bar{1}0]$ incidence (d) top MgB_2 at $[11\bar{2}0]$ incidence

6.4 Conclusions

To summarize, we have optimized the MBE growth condition to enhance the film quality of MgB_2. We also succeeded in growing fully epitaxial multilayer heterostructures of MgB_2-MgO-MgB_2. Vertical Josephson junctions were fabricated based on the heterostructures. The MgB_2-MgO-MgB_2 Josephson junctions exhibited good device behavior, including Fraunhofer patterns and Fiske steps, which require a uniform barrier to be observed. Furthermore, we also realized the combination of MgB_2 with ferromagnetic insulator EuS. The EuS-MgB_2 heterostructure can be combined with topological insulator, providing a platform to search for Majorana modes. On the other hand, the combination of MgB_2 and the topological insulator BST will be discussed in next chapter.

Chapter 7
BST-MgB_2 heterostructure

7.1 Motivation

We have already shown the successful achievement of wafer sized BST-Nb heterostructure and related device performance. Nb was used due to its stability during fabrication processes. However, the superconducting gap of Nb is still relatively small, having no advantage compared to $NbSe_2$ used in the Bi_2Se_3-$NbSe_2$ heterostructure [11-13], where a zero bias conductance peak has been observed in the vortex core as a signature of Majorana zero-mode. As we have shown in section 2.3.2, the energy splitting between the zero-energy state and other low-lying vortex core bound states is on the order of Δ^2/E_F. To better distinguish them, a superconductor with larger band gap will be helpful.

High-T_c superconductors could be a choice, however, due to their anisotropic *d*-wave pairing nature, do not couple as effectively with the isotropic topological surface states. Moreover, the complex stoichiometry of typical high-T_c superconductors increases the difficulty to grow them in the form of thin films, thereby limiting the possibility of wafer sized heterostructures. The existing combinations of TI and high-T_c superconductors have employed $Bi_2Sr_2CaCu_2O_{8+\delta}$ cleaved from bulk crystal. [83, 84]. By contrast, MgB_2 has relatively high T_c and simpler stoichiometry, and its layered hexagonal structure matches the growth of the layered topological materials through *Van de Waals epitaxy*. We have readily achieved thin films of both BST and MgB_2 in high quality. One step further, the heterostructure of BST-MgB_2 would bring more possibilities of studying the proximity effects on topological surfaces. The larger σ-gap residing on the 2D cylindrical Fermi surface from σ antibonding states of MgB_2 is expected to couple stronger with the 2D topological surface states, thus can induce the desired 2D superconductivity into the surface states of BST.

Dr. Long Cheng and Dr. Hui Zhang contributed to this chapter by collaborating for sample growth. The TEM was done by the group of Prof. Xixiang Zhang at the King Abdullah University of Science and Technology (KAUST).

7.2 MBE growth of BST-MgB_2 heterostructures

7.2.1 Role of substrate temperature

The BST-MgB_2 heterostructures were grown on Si (111) substrates. After deposition of MgB_2, sample was transferred to the TI chamber. Similar to the growth of BST on Nb, when growing on MgB_2, the substrate temperature also needed to be lowered to compensate the over-heating due to existing films on substrates. The optimal substrate temperature was found to be 150 ºC, the same as the case when growing BST-Nb heterostructures on sapphire. For heterostructures grown at ~ 270 ºC, which is the typical temperature for growth of BST on bare Si, *in situ* XPS showed deficiency in Bi and Sb, and *ex situ* XRD showed no BST peaks. This indicates that the substrate was already above the BST decomposing temperature. Furthermore, for samples grown at > 270 ºC, the films suffered from severe chemical reaction and broke into cracks immediately once exposed to air. Figure 7-1 showed the structure of these cracks under microscope. Broken samples lost conductivity, revealed by more than 4 orders higher resistance than unbroken films at room temperature. In addition, absence of superconducting transition indicates that the MgB_2 film at bottom were destroyed by chemical reaction. We confirmed that the reaction did not happen in vacuum nor in nitrogen atmosphere until exposed to air, while higher humidity level in air can speed up the reaction. Therefore, we speculate that the chemical reactions are related to certain kind of compound that is sensitive to moisture in air forming at the interface of BST and MgB_2 when growth temperature is high. We tried to deposit a thin layer (2.5 nm) of Nb by magnetron sputtering on MgB_2 before depositing BST, to prevent formation of undesired compound between BST and MgB_2. It turned out that the insertion of Nb can increase the critical temperature for reaction to happen (from 270 ºC to 300 ºC), but does not fully prevent it. When growth temperature was higher than 300 ºC, samples with Nb protection still degraded immediately in air.

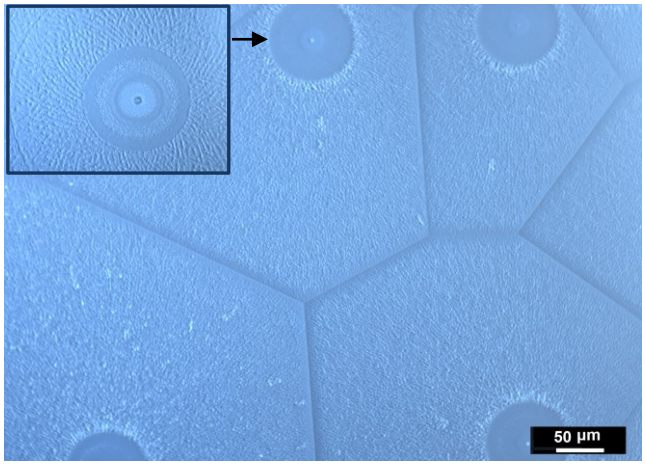

Figure 7-1: Cracks of MgB_2-BST heterostructure under optical microscope.

7.2.2 Role of Nb insertion layer

As we have talked earlier, the optimal substrate temperature was 150 ºC for BST phase to form on top of MgB_2. Being aware of that the BST-MgB_2 interface is chemically active, successful formation of BST thin films at this lower temperature does not guarantee a good BST-MgB_2 interface. It is possible that the reaction already happened at the interface but not yet further extended to the bulk of films at lowered temperature. In this case, a thin Nb insertion layer between BST and MgB_2 would still be necessary. We compared the growth results with/without Nb and found out that the Nb insertion layer indeed improved the interface quality, meanwhile facilitated the epitaxy of BST films. Figure 7-2 and Figure 7-3 present the RHEED, XRD and cross-sectional TEM images of two samples, which are BST-2.5 nm Nb/MgB_2 and BST-MgB_2 heterostructures following the same growth condition. The RHEED patterns of BST grown directly on MgB_2 are dark and thick streaks, mixing with some weak poly-rings. As a comparison, the one with 2.5 nm Nb insertion layer shows bright and sharp RHEED streaks, comparable to the quality of BST-Nb heterostructure grown on sapphire by two steps growth, talked in chapter 4. This indicates that Nb provides a better surface for BST to grow epitaxially. XRD results are consistent with RHEED. Both samples show the characteristic diffraction peaks from BST {0001} plane family, meaning that BST can grow along *c*-axis on MgB_2 with or without Nb insertion, whereas the one with Nb has higher quality. From the cross-sectional TEM images (Figure 7-3) we can see that the Nb layer plays a crucial role to protect the interface. Without Nb, the interface between BST and MgB_2 is very rough, showing amorphous

feature, which indicates BST and MgB_2 react with each other at the growth temperature. The reaction extends to the BST layer for about 1~2 nm. As the growth continues, BST lattice starts to form. However, the BST lattice shows obviously wavy patterns with many grains and defects due to the rough interface. In apparent contrast, TEM image of the other sample with the Nb insertion layer shows clear structure of the BST quintuple layers. Both interfaces of MgB_2-Nb and Nb-BST are smooth. The Nb insertion layer grown on MgB_2 is single crystalline and it prevents reactions between BST and MgB_2, so that the following BST layer can grow well.

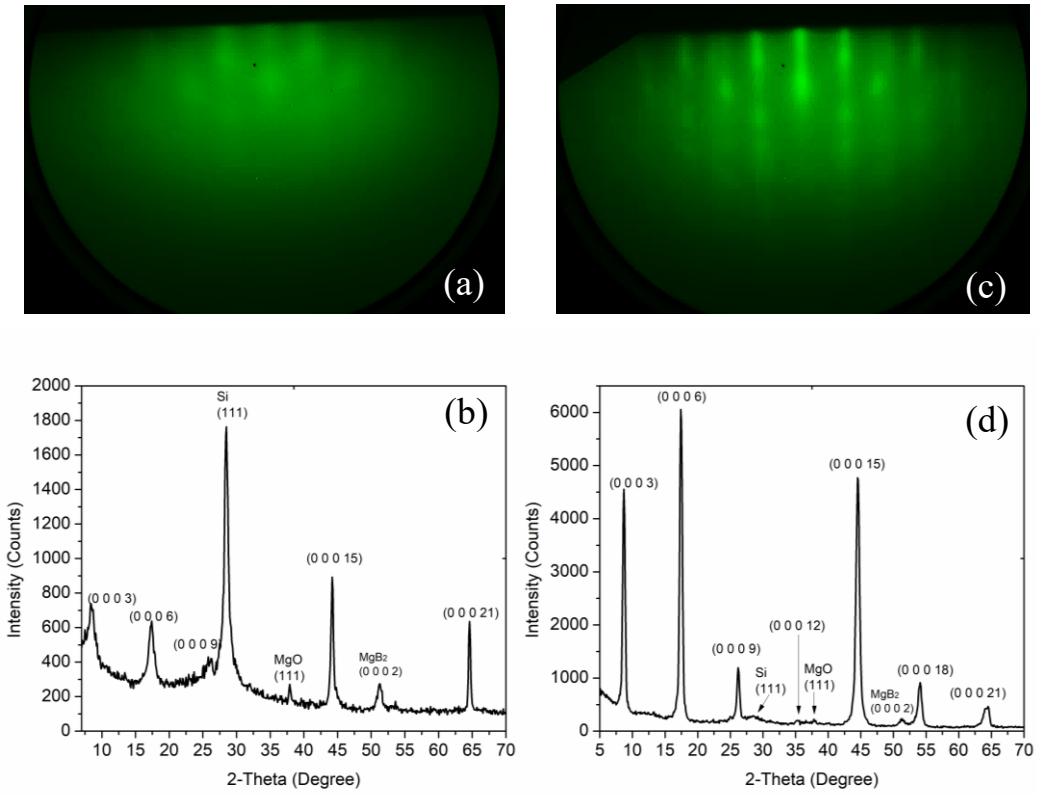

Figure 7-2: (a)-(b) RHEED pattern and XRD θ-2θ scan of BST film grown directly on MgB_2 (c)-(d) BST grown on 2.5nm Nb protected MgB_2.

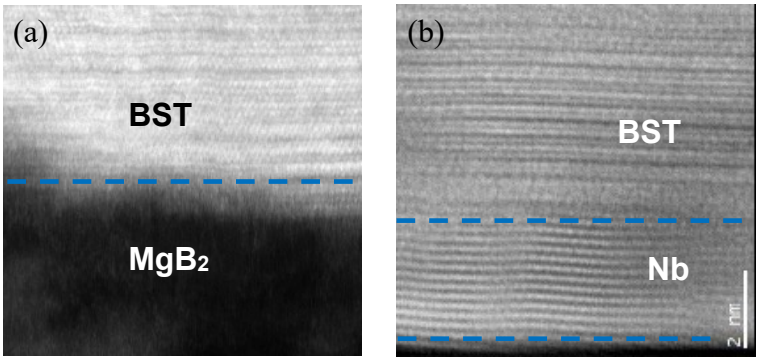

Figure 7-3: Cross-sectional TEM images of BST films (a) grown directly on MgB_2 and (b) grown on Nb protected MgB_2

From the view point of thin film growth, Nb insertion layer does improve the crystal quality of the heterostructure. The cost is losing direct proximity from MgB_2. However, considering coherence length in Nb is long enough (~ 40 nm), the superconducting proximity can still reach BST. We can view the Nb/MgB_2 part as a superconductor with higher T_c and enhanced superconducting gap compared with pure Nb.

7.3 BST-MgB_2 Josephson junctions

The superconducting transition temperature of BST-MgB_2 and BST-Nb/MgB_2 heterostructures was measured to be around 28 K and 30 K for 25 nm MgB_2, see Figure 7-4 (d). Thickness of BST is 7 nm and Nb insertion layer is 2.5 nm. To further check the property of these two heterostructures, we deposited 50 nm Nb on top to fabricate Nb-BST-MgB_2 and Nb-BST-Nb/MgB_2 junctions. The choice of Nb to be top superconducting layer will simplify the growth process because deposition of Nb does not require elevated substrate temperature that may destroy the BST-MgB_2 interface. Fabrication process and measurement setup is the same with the Nb-BST-Nb junctions discussed in chapter 5, except that the junction dimension was reduced to 2 μm considering larger roughness introduced by MgB_2. Figure 7-4 shows the measurement results including the I-V characteristics and differential conductance dI/dV-V with dI/dV values collected by lock-in measurements. Despite the same thickness of BST barrier, the two types of junction exhibit significantly different behaviors.

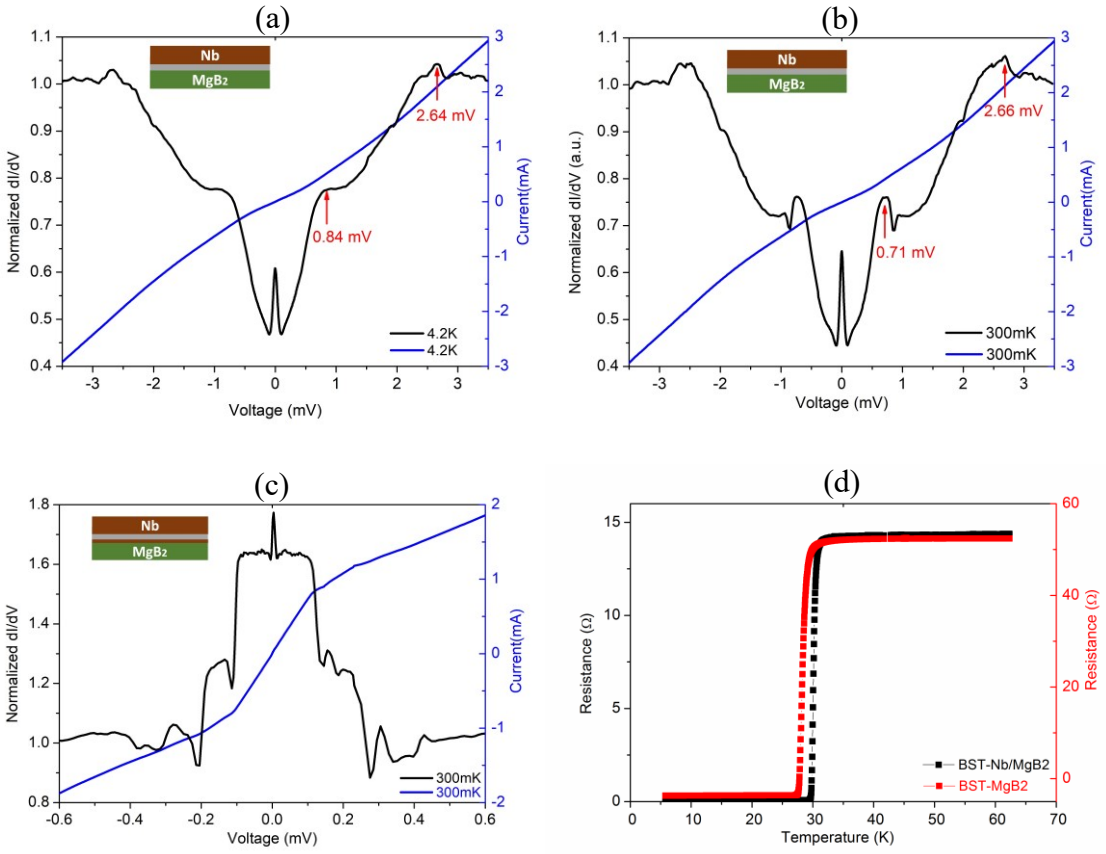

Figure 7-4: I-V characteristics (blue) and dI/dV-V curves (black) measured on (a) Nb-BST-MgB_2 junctions at 4.2 K, (b) Nb-BST-MgB_2 junctions at 300 mK and (c) Nb-BST-Nb/MgB_2 junctions at 300 mK. (d) R-T curve showing superconducting transition temperature of BST-MgB_2 and BST-Nb/MgB_2 heterostructures.

(1) Nb-BST-MgB_2 junction

From Figure 7-4 (a) and (b), we can see the dominate feature of the Nb-BST-MgB_2 junction is tunneling effect through normal electrons, as an asymmetric S_1-I-S_2 tunneling junction. At 4.2 K, there are two conductance peaks appearing at the V = 2.64 mV and 0.84 mV, identified as $\Delta_1+\Delta_2$ and $\Delta_1-\Delta_2$. It can be estimated that $\Delta_1 \sim 1.7$ meV is the π gap of MgB_2 and $\Delta_2 \sim 0.9$ meV is the gap of Nb. After further cooling down to 300 mK, $\Delta_1+\Delta_2$ increased a bit and $\Delta_1-\Delta_2$ decreased. This is reasonable as Δ_2 from Nb should increase more than Δ_1 within the given temperature change. The overall tunneling feature of this junction indicates an insulating layer formed at the BST/MgB_2 interface,

which can also be seen from the cross-sectional TEM image (Figure 7-3). This insulating layer suppresses direct Josephson coupling between Nb and MgB_2.

(2) Nb-BST-Nb/MgB_2 junction

The junction with a thin Nb insertion layer between BST and MgB_2 behaves like a Josephson junction, where we see conductance enhancement at low bias. The overall shape of the conductance curve is similar to that of a Nb-BST-Nb junction discussed in chapter 5 (Figure 5-7). Previous discussions on the Nb-BST-Nb junction should still apply here. Because the two superconductors directly touching BST layer are Nb in both junctions, we expect the transport mechanism to be the same. The only difference is, with MgB_2 underneath the bottom Nb, the bottom electrodes Nb/MgB_2 has higher T_c than pure Nb. On the other hand, the MgB_2 layer introduces significant roughness which reduces the barrier uniformity and can lead to current leakage. As a result, even though we reduced the Nb-BST-Nb/MgB_2 junction size to 2 μm, it still has much smaller junction resistance (~0.06 Ω) compared with the 4 μm Nb-BST-Nb junction (~0.4 Ω according to Figure 5-6).

A common feature shared by the three junctions (Nb-BST-MgB_2, Nb-BST-Nb/MgB_2 and Nb-BST-Nb) is the zero bias conductance peak (ZBCP). In the Nb-BST-Nb junction, the ZBCP does not show up until cooling down to 300 mK, whereas in the junction with MgB_2, it is present at 4.2 K and can be enhanced at 300 mK. Previously in chapter 5, we discussed that the ZBCP could be caused by tiny Andreev bound states forming at the conducting TI side surfaces (Figure 7-5), which is weak and can only be seen at very low temperature. Here with MgB_2 improving the T_c, we can see this part of contribution at higher temperature. As the ZBCP is attributed to the BST side surface, which is an additional channel parallel to the junction bulk channel, its presence does not depend on the interface quality. Therefore, it can appear in the tunneling gap when the bulk channel is a tunneling junction (Nb-BST-MgB_2) or on the conductance plateau when the bulk is a Josephson junction (Nb-BST-Nb/MgB_2 and Nb-BST-Nb).

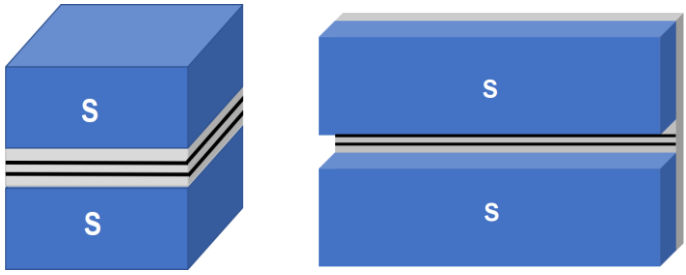

Figure 7-5: Schematic illustration of Andreev bound states forming on the side surfaces of TI in the vertical S-TI-S junction(left), which can be seen as a planar S-TI-S junction (right) being folded. The grey area is TI and black lines indicate the bound states in these junctions.

7.4 Conclusions

In this chapter, we discussed the MBE growth of BST on MgB_2, which is challenging due to chemically active BST-MgB_2 interface. The growth temperature of BST has to be lowered for successful growth. However, even if stable BST-MgB_2 heterostructure can be obtained at low growth temperature, the interface is not ideal according to cross sectional TEM image. With insertion of a thin layer Nb, the quality of interface and BST film can be improved. Vertical junctions based on BST-MgB_2 heterostructure were fabricated and measured. On one hand, the results demonstrate that the heterostructure is durable during fabrication process. On the other hand, the interface quality apparently determines overall junction behavior. Without Nb insertion, the junction behaves as a tunneling junction due to formation of insulating layer at the interface, while the one with Nb insertion layer behaves more like a Josephson junction.

Chapter 8
Summary

The interface of topological insulator and superconductor is a candidate system to host Majorana zero-modes. Several approaches have been proposed by theorists, such as magnetic vortex core, S-TI-S line junctions or S-TI-FI boundaries. Experimental studies to realize those proposals would request high quality heterostructures. Driven by this motivation, the work in this thesis focuses on the growth of high-quality TI heterostructures on wafer size scale. We also demonstrated the heterostructures are compatible with fabrication process by fabricating and measuring different kinds of vertical Josephson junctions. Specifically, the achievements can be summarized as follows, which consist the steps reaching the final goal:

1. **Obtain epitaxial and bulk insulating TI films.** We choose $(Bi_{0.5}Sb_{0.5})_2Te_3$ thin film as its bulk conductivity is tunable by regulating Bi:Sb ratio. Epitaxy of the BST film grown on different substrates including Si (111), *c*-cut sapphire and STO (111) has been demonstrated by RHEED and XRD. Layer-by-layer growth mode was achieved, supported by RHEED oscillations. Transport measurements on the $(Bi_{0.5}Sb_{0.5})_2Te_3$ thin film confirmed it is bulk insulating with sheet carrier density on the order of 10^{-12} cm^{-2}. This part of work has been presented in chapter 4, section 4.2.
2. **Grow superconducting MgB_2 thin film with optimized property.** With its T_c as high as 39 K, MgB_2 is a promising superconductor to be combined with TI. However, the growth of MgB_2 requires large flux of Mg, which will result in excess Mg and makes the film unstable in ambient environment. With the assistance of *in situ* RHEED monitoring, we optimized the growth condition by identifying a threshold growth temperature which has a self-limiting effect on the MgB_2 stoichiometry. Furthermore, high quality hetero-epitaxial (0001)-MgB_2/(111)-MgO/(0001)-MgB_2 structures were subsequently created and patterned into Josephson junctions with clear Fraunhofer patterns and Fiske steps, further confirming the high quality of the materials fabricated with our deposition techniques. This part of work has been presented in chapter 6, section 6.2 and 6.3.

3. **Grow BST on top of a superconductor to get TI-S heterostructure.** The growth of BST on two superconductors, Nb and MgB_2, has been investigated. On both materials the growth temperature has to be re-adjusted, which was found to be 150 ºC, deviating from that on bare substrates (270 ºC). This could be caused by difference in thermal radiation properties between bare substrates and film covered substrates considering the substrate is heated by radiation in this system. The crystal property of BST-Nb and BST-MgB_2 has been characterized by RHEED and XRD. Interface quality was characterized by TEM. Especially, for the BST-MgB_2, we found the interface is chemically active which however can be solved by inserting a thin layer of Nb in between. The discussion on BST-Nb is presented in chapter 4 section 4.3, while the BST-MgB_2 heterostructure is discussed in chapter 6 section 6.4.
4. **Fabrication and measurement on vertical S-TI-S Josephson junctions.** Starting from the three types of bilayer heterostructures, we grew S-TI-S sandwich structures by depositing a top layer of Nb and fabricated vertical Josephson junctions. In chapter 5, we discussed the measurement results on Nb-BST-Nb junctions. We identified three channels contributing to the overall conductance. In chapter 7 section 7.3, we discussed another two MgB_2-based junctions, one is Nb-BST-MgB_2, the other is Nb-BST-Nb/MgB_2 with a thin layer Nb insertion between BST and MgB_2. The Nb insertion layer was found to be necessary, otherwise an insulating layer will form at the interface suggested by the tunneling behavior of the Nb-BST-MgB_2 junction. A ZBCP was seen on all three types of junctions. However, limited by the energy resolution, whether the ZBCP is related to the long-expected Majorana states is still not confirmed. These results demonstrate the heterostructures are feasible to go through fabrication; moreover, they provide information to understand the seldomly studied vertical S-TI-S junctions.
5. **Introduce magnetic interaction through proximity with ferromagnetic insulator EuS**. In addition to combining BST with superconductors, we grew BST-EuS heterostructures and observed ferromagnetic order can be induced onto the BST surfaces, presented in chapter 4, section 4.4. Besides this, growth of an EuS-MgB_2 structure is presented in chapter 6. These heterostructures act as ingredients to be combined together to realize a S-TI-FI structure that can host chiral Majorana modes.

The achievement of these heterostructures will provide platforms to study Majorana physics at the interface from different points of view. For example, further investigation on these heterostructures can be achieved by STM. Compared with transport in a fabricated vertical junction, tunneling through the tip of STM to the BST-Nb or BST-MgB_2 film will exclude the complexity of conductance contribution. Moreover, the tip can be placed over a magnetic vortex, providing local information directly related to the vortex where signature of Majorana modes could be found. Alternatively, planar S-TI-S junction can be fabricated in the future and 4π periodicity in the current-phase relationship of such junction will signal existence of Majorana modes. One can also create an S-TI-FI junction to look for Majorana modes at the boundary between a topologically superconducting region and a magnetically gapped region. Compared with most studies using TI flakes, fabrication based on these wafer sized heterostructures will break the size limitation, bringing possibilities for scaling up in future applications.

Appendix A

Lattice parameters

Material	Crystal structure	Lattice constant (Å)
Al_2O_3	Hexagonal	a=4.765, c=12.991 [190]
Bi_2Te_3	Hexagonal	a=4.380, c=30.487 [88]
Sb_2Te_3	Hexagonal	a=4.260, c=30.458 [88]
MgB_2	Hexagonal	a=3.086, c=3.524 [155]
Si	Cubic	a=5.431 [191]
$SrTiO_3$	Cubic	a=3.905 [192]
Nb	Cubic	a=3.300 [193]
MgO	Cubic	a=4.211 [194]
EuS	Cubic	a=5.968 [195]

Bibliography

[1] K. Von Klitzing, "The quantized Hall effect," *Reviews of Modern Physics,* vol. 58, p. 519, 1986.

[2] B. A. Bernevig and S. C. Zhang, "Quantum spin Hall effect," *Phys Rev Lett,* vol. 96, p. 106802, Mar 17 2006.

[3] B. A. Bernevig, T. L. Hughes, and S. C. Zhang, "Quantum spin Hall effect and topological phase transition in HgTe quantum wells," *Science,* vol. 314, pp. 1757-61, Dec 15 2006.

[4] C. L. Kane and E. J. Mele, "Quantum spin Hall effect in graphene," *Phys Rev Lett,* vol. 95, p. 226801, Nov 25 2005.

[5] D. Hsieh, Y. Xia, D. Qian, L. Wray, J. H. Dil, F. Meier*, et al.*, "A tunable topological insulator in the spin helical Dirac transport regime," *Nature,* vol. 460, pp. 1101-5, Aug 27 2009.

[6] C.-Z. Chang, J. Zhang, X. Feng, J. Shen, Z. Zhang, M. Guo*, et al.*, "Experimental observation of the quantum anomalous Hall effect in a magnetic topological insulator," *Science,* vol. 340, pp. 167-170, 2013.

[7] L. Fu and C. L. Kane, "Superconducting proximity effect and majorana fermions at the surface of a topological insulator," *Phys Rev Lett,* vol. 100, p. 096407, Mar 7 2008.

[8] X.-L. Qi and S.-C. Zhang, "Topological insulators and superconductors," *Reviews of Modern Physics,* vol. 83, p. 1057, 2011.

[9] C. Nayak, S. H. Simon, A. Stern, M. Freedman, and S. D. Sarma, "Non-Abelian anyons and topological quantum computation," *Reviews of Modern Physics,* vol. 80, p. 1083, 2008.

[10] S. D. Sarma, M. Freedman, and C. Nayak, "Majorana zero modes and topological quantum computation," *npj Quantum Information,* vol. 1, p. 15001, 2015.

[11] J.-P. Xu, C. Liu, M.-X. Wang, J. Ge, Z.-L. Liu, X. Yang*, et al.*, "Artificial topological superconductor by the proximity effect," *Physical Review Letters,* vol. 112, p. 217001, 2014.

[12] J. P. Xu, M. X. Wang, Z. L. Liu, J. F. Ge, X. Yang, C. Liu*, et al.*, "Experimental detection of a Majorana mode in the core of a magnetic vortex inside a topological insulator-superconductor Bi(2)Te(3)/NbSe(2) heterostructure," *Phys Rev Lett,* vol. 114, p. 017001, Jan 9 2015.

[13] H.-H. Sun, K.-W. Zhang, L.-H. Hu, C. Li, G.-Y. Wang, H.-Y. Ma*, et al.*, "Majorana zero mode detected with spin selective Andreev reflection in the vortex of a topological superconductor," *Physical review letters,* vol. 116, p. 257003, 2016.

[14] S. Ghatak, O. Breunig, F. Yang, Z. Wang, A. A. Taskin, and Y. Ando, "Anomalous Fraunhofer patterns in gated Josephson junctions based on the bulk-insulating topological insulator BiSbTeSe2," *Nano letters,* vol. 18, pp. 5124-5131, 2018.

[15] C. Kurter, A. Finck, Y. S. Hor, and D. J. Van Harlingen, "Evidence for an anomalous current–phase relation in topological insulator Josephson junctions," *Nature communications,* vol. 6, p. 7130, 2015.

[16] M. Veldhorst, M. Snelder, M. Hoek, T. Gang, V. Guduru, X. Wang*, et al.*, "Josephson supercurrent through a topological insulator surface state," *Nature materials,* vol. 11, p. 417, 2012.

[17] Y. Tanaka, T. Yokoyama, and N. Nagaosa, "Manipulation of the Majorana fermion, Andreev reflection, and Josephson current on topological insulators," *Physical review letters,* vol. 103, p. 107002, 2009.

[18] J. Kortus, I. Mazin, K. D. Belashchenko, V. P. Antropov, and L. Boyer, "Superconductivity of metallic boron in MgB 2," *Physical Review Letters,* vol. 86, p. 4656, 2001.
[19] J. Nagamatsu, N. Nakagawa, T. Muranaka, Y. Zenitani, and J. Akimitsu, "Superconductivity at 39 K in magnesium diboride," *nature,* vol. 410, p. 63, 2001.
[20] D. J. Thouless, M. Kohmoto, M. P. Nightingale, and M. den Nijs, "Quantized Hall Conductance in a Two-Dimensional Periodic Potential," *Physical Review Letters,* vol. 49, pp. 405-408, 08/09/ 1982.
[21] C. L. Kane and E. J. Mele, "Z2 topological order and the quantum spin Hall effect," *Phys Rev Lett,* vol. 95, p. 146802, Sep 30 2005.
[22] L. Fu, C. L. Kane, and E. J. Mele, "Topological insulators in three dimensions," *Phys Rev Lett,* vol. 98, p. 106803, Mar 9 2007.
[23] M. Kohmoto, "Topological invariant and the quantization of the Hall conductance," *Annals of Physics,* vol. 160, pp. 343-354, 1985.
[24] M. König, S. Wiedmann, C. Brüne, A. Roth, H. Buhmann, L. W. Molenkamp*, et al.*, "Quantum spin Hall insulator state in HgTe quantum wells," *Science,* vol. 318, pp. 766-770, 2007.
[25] C. L. Kane and E. J. Mele, "Z 2 topological order and the quantum spin Hall effect," *Physical review letters,* vol. 95, p. 146802, 2005.
[26] C.-C. Liu, W. Feng, and Y. Yao, "Quantum spin Hall effect in silicene and two-dimensional germanium," *Physical review letters,* vol. 107, p. 076802, 2011.
[27] Y. Chen, J. G. Analytis, J.-H. Chu, Z. Liu, S.-K. Mo, X.-L. Qi*, et al.*, "Experimental realization of a three-dimensional topological insulator, Bi2Te3," *science,* vol. 325, pp. 178-181, 2009.
[28] T. Fukui, T. Fujiwara, and Y. Hatsugai, "Topological Meaning of Z2 Numbers in Time Reversal Invariant Systems," *Journal of the Physical Society of Japan,* vol. 77, p. 123705, 2008/12/15 2008.
[29] X.-L. Qi, T. L. Hughes, and S.-C. Zhang, "Topological field theory of time-reversal invariant insulators," *Physical Review B,* vol. 78, p. 195424, 2008.
[30] Z. Wang, X.-L. Qi, and S.-C. Zhang, "Equivalent topological invariants of topological insulators," *New Journal of Physics,* vol. 12, p. 065007, 2010.
[31] R. Roy, "Z 2 classification of quantum spin Hall systems: An approach using time-reversal invariance," *Physical Review B,* vol. 79, p. 195321, 2009.
[32] M. Z. Hasan and C. L. Kane, "Colloquium: Topological insulators," *Reviews of Modern Physics,* vol. 82, pp. 3045-3067, 11/08/ 2010.
[33] L. Fu, C. L. Kane, and E. J. Mele, "Topological insulators in three dimensions," *Physical review letters,* vol. 98, p. 106803, 2007.
[34] J. E. Moore and L. Balents, "Topological invariants of time-reversal-invariant band structures," *Physical Review B,* vol. 75, p. 121306, 2007.
[35] R. Roy, "Topological phases and the quantum spin Hall effect in three dimensions," *Physical Review B,* vol. 79, p. 195322, 2009.
[36] D. Hsieh, D. Qian, L. Wray, Y. Xia, Y. S. Hor, R. J. Cava*, et al.*, "A topological Dirac insulator in a quantum spin Hall phase," *Nature,* vol. 452, p. 970, 04/24/online 2008.
[37] H. Zhang, C.-X. Liu, X.-L. Qi, X. Dai, Z. Fang, and S.-C. Zhang, "Topological insulators in Bi 2 Se 3, Bi 2 Te 3 and Sb 2 Te 3 with a single Dirac cone on the surface," *Nature physics,* vol. 5, p. 438, 2009.

[38] Y. Xia, D. Qian, D. Hsieh, L. Wray, A. Pal, H. Lin, *et al.*, "Observation of a large-gap topological-insulator class with a single Dirac cone on the surface," *Nature physics,* vol. 5, p. 398, 2009.

[39] S. Park, W. Jung, C. Kim, D. Song, C. Kim, S. Kimura, *et al.*, "Quasiparticle scattering and the protected nature of the topological states in a parent topological insulator Bi 2 Se 3," *Physical Review B,* vol. 81, p. 041405, 2010.

[40] Y. Xia, D. Qian, D. Hsieh, R. Shankar, H. Lin, A. Bansil, *et al.*, "Topological Control: Systematic control of topological insulator Dirac fermion density on the surface of Bi2Te3," *arXiv preprint arXiv:0907.3089,* 2009.

[41] D. Hsieh, Y. Xia, D. Qian, L. Wray, F. Meier, J. Dil, *et al.*, "Observation of time-reversal-protected single-Dirac-cone topological-insulator states in Bi 2 Te 3 and Sb 2 Te 3," *Physical review letters,* vol. 103, p. 146401, 2009.

[42] D. Hsieh, Y. Xia, D. Qian, L. Wray, J. Dil, F. Meier, *et al.*, "A tunable topological insulator in the spin helical Dirac transport regime," *Nature,* vol. 460, p. 1101, 2009.

[43] Z.-H. Pan, E. Vescovo, A. Fedorov, D. Gardner, Y. Lee, S. Chu, *et al.*, "Electronic structure of the topological insulator Bi 2 Se 3 using angle-resolved photoemission spectroscopy: evidence for a nearly full surface spin polarization," *Physical review letters,* vol. 106, p. 257004, 2011.

[44] Y. Zhang, K. He, C.-Z. Chang, C.-L. Song, L.-L. Wang, X. Chen, *et al.*, "Crossover of the three-dimensional topological insulator Bi 2 Se 3 to the two-dimensional limit," *Nature Physics,* vol. 6, p. 584, 2010.

[45] Y. Y. Li, G. Wang, X. G. Zhu, M. H. Liu, C. Ye, X. Chen, *et al.*, "Intrinsic topological insulator Bi2Te3 thin films on Si and their thickness limit," *Advanced materials,* vol. 22, pp. 4002-4007, 2010.

[46] G. Koren, T. Kirzhner, E. Lahoud, K. Chashka, and A. Kanigel, "Proximity-induced superconductivity in topological Bi 2 Te 2 Se and Bi 2 Se 3 films: Robust zero-energy bound state possibly due to Majorana fermions," *Physical Review B,* vol. 84, p. 224521, 2011.

[47] C.-K. Chiu, M. J. Gilbert, and T. L. Hughes, "Vortex lines in topological insulator-superconductor heterostructures," *Physical Review B,* vol. 84, p. 144507, 2011.

[48] F. Yang, Y. Ding, F. Qu, J. Shen, J. Chen, Z. Wei, *et al.*, "Proximity effect at superconducting Sn-Bi 2 Se 3 interface," *Physical Review B,* vol. 85, p. 104508, 2012.

[49] F. Yang, F. Qu, J. Shen, Y. Ding, J. Chen, Z. Ji, *et al.*, "Proximity-effect-induced superconducting phase in the topological insulator Bi 2 Se 3," *Physical Review B,* vol. 86, p. 134504, 2012.

[50] G. Koren, T. Kirzhner, Y. Kalcheim, and O. Millo, "Signature of proximity-induced px+ ipy triplet pairing in the doped topological insulator Bi2Se3 by the s-wave superconductor NbN," *EPL (Europhysics Letters),* vol. 103, p. 67010, 2013.

[51] G. Koren, "Proximity effects at the interface of a superconductor and a topological insulator in NbN-Bi2Se3 thin film bilayers," *Superconductor Science and Technology,* vol. 28, p. 025003, 2014.

[52] C. Granstrom, I. Fridman, H.-C. Lei, C. Petrovic, and J. Wei, "Andreev reflection spectroscopy on Bi $ _ {2} $ X $ _ {3} $(X= Se, Te) topological insulators: Implications for the c-axis superconducting proximity effect," *arXiv preprint arXiv:1711.00144,* 2017.

[53] D. Flötotto, Y. Ota, Y. Bai, C. Zhang, K. Okazaki, A. Tsuzuki*, et al.*, "Superconducting pairing of topological surface states in bismuth selenide films on niobium," *Science advances,* vol. 4, p. eaar7214, 2018.
[54] X. L. Qi, T. L. Hughes, S. Raghu, and S. C. Zhang, "Time-reversal-invariant topological superconductors and superfluids in two and three dimensions," *Phys Rev Lett,* vol. 102, p. 187001, May 8 2009.
[55] A. P. Schnyder, S. Ryu, A. Furusaki, and A. W. Ludwig, "Classification of topological insulators and superconductors in three spatial dimensions," *Physical Review B,* vol. 78, p. 195125, 2008.
[56] C. Kallin and J. Berlinsky, "Chiral superconductors," *Reports on Progress in Physics,* vol. 79, p. 054502, 2016.
[57] N. Read and D. Green, "Paired states of fermions in two dimensions with breaking of parity and time-reversal symmetries and the fractional quantum Hall effect," *Physical Review B,* vol. 61, p. 10267, 2000.
[58] A. Y. Kitaev, "Unpaired Majorana fermions in quantum wires," *Physics-Uspekhi,* vol. 44, p. 131, 2001.
[59] J. Alicea, "New directions in the pursuit of Majorana fermions in solid state systems," *Reports on progress in physics,* vol. 75, p. 076501, 2012.
[60] B. A. Bernevig and T. L. Hughes, *Topological insulators and topological superconductors*: Princeton university press, 2013.
[61] G. Volovik, "Fermion zero modes on vortices in chiral superconductors," *Journal of Experimental and Theoretical Physics Letters,* vol. 70, pp. 609-614, 1999.
[62] D. A. Ivanov, "Non-Abelian statistics of half-quantum vortices in p-wave superconductors," *Physical review letters,* vol. 86, p. 268, 2001.
[63] G. Volovik, "An analog of the quantum Hall effect in a superfluid 3 He film," *Soviet Physics-JETP (English Translation),* vol. 67, pp. 1804-1811, 1988.
[64] J. Alicea, Y. Oreg, G. Refael, F. Von Oppen, and M. P. Fisher, "Non-Abelian statistics and topological quantum information processing in 1D wire networks," *Nature Physics,* vol. 7, p. 412, 2011.
[65] T. Rice and M. Sigrist, "Sr2RuO4: an electronic analogue of 3He?," *Journal of Physics: Condensed Matter,* vol. 7, p. L643, 1995.
[66] T. Nomura and K. Yamada, "Detailed investigation of gap structure and specific heat in the p-wave superconductor Sr2RuO4," *Journal of the Physical Society of Japan,* vol. 71, pp. 404-407, 2002.
[67] K. Nelson, Z. Mao, Y. Maeno, and Y. Liu, "Odd-parity superconductivity in Sr2RuO4," *Science,* vol. 306, pp. 1151-1154, 2004.
[68] C. Kallin, "Chiral p-wave order in Sr2RuO4," *Reports on Progress in Physics,* vol. 75, p. 042501, 2012.
[69] S. Sasaki, M. Kriener, K. Segawa, K. Yada, Y. Tanaka, M. Sato*, et al.*, "Topological Superconductivity in ${\mathrm{Cu}}_{x}{\mathrm{Bi}}_{2}{\mathrm{Se}}_{3}$," *Physical Review Letters,* vol. 107, p. 217001, 11/14/ 2011.
[70] L. Fu and E. Berg, "Odd-Parity Topological Superconductors: Theory and Application to ${\mathrm{Cu}}_{x}{\mathrm{Bi}}_{2}{\mathrm{Se}}_{3}$," *Physical Review Letters,* vol. 105, p. 097001, 08/23/ 2010.

[71] Y. S. Hor, A. J. Williams, J. G. Checkelsky, P. Roushan, J. Seo, Q. Xu, *et al.*, "Superconductivity in Cu x Bi 2 Se 3 and its implications for pairing in the undoped topological insulator," *Physical review letters,* vol. 104, p. 057001, 2010.

[72] L. Fu, "Odd-parity topological superconductor with nematic order: Application to ${\mathrm{Cu}}_{x}{\mathrm{Bi}}_{2}{\mathrm{Se}}_{3}$," *Physical Review B,* vol. 90, p. 100509, 09/26/ 2014.

[73] R. Fisher, S. Kim, B. Woodfield, N. Phillips, L. Taillefer, K. Hasselbach, *et al.*, "Specific heat of UPt 3: Evidence for unconventional superconductivity," in *Ten Years of Superconductivity: 1980–1990*, ed: Springer, 1989, pp. 189-192.

[74] H. Tou, Y. Kitaoka, K. Asayama, N. Kimura, Y. Ōnuki, E. Yamamoto, *et al.*, "Odd-parity superconductivity with parallel spin pairing in UPt 3: evidence from 195 Pt Knight shift study," *Physical review letters,* vol. 77, p. 1374, 1996.

[75] H. Tou, Y. Kitaoka, K. Ishida, K. Asayama, N. Kimura, E. Yamamoto, *et al.*, "Nonunitary Spin-Triplet Superconductivity in UPt 3: Evidence from P 195 t Knight Shift Study," *Physical review letters,* vol. 80, p. 3129, 1998.

[76] Y. Machida, A. Itoh, Y. So, K. Izawa, Y. Haga, E. Yamamoto, *et al.*, "Twofold spontaneous symmetry breaking in the heavy-fermion superconductor UPt 3," *Physical review letters,* vol. 108, p. 157002, 2012.

[77] E. Schemm, W. Gannon, C. Wishne, W. P. Halperin, and A. Kapitulnik, "Observation of broken time-reversal symmetry in the heavy-fermion superconductor UPt3," *Science,* vol. 345, pp. 190-193, 2014.

[78] L. Fu and C. L. Kane, "Superconducting proximity effect and Majorana fermions at the surface of a topological insulator," *Physical review letters,* vol. 100, p. 096407, 2008.

[79] Q. L. He, L. Pan, A. L. Stern, E. C. Burks, X. Che, G. Yin, *et al.*, "Chiral Majorana fermion modes in a quantum anomalous Hall insulator-superconductor structure," *Science,* vol. 357, pp. 294-299, Jul 21 2017.

[80] M.-X. Wang, C. Liu, J.-P. Xu, F. Yang, L. Miao, M.-Y. Yao, *et al.*, "The coexistence of superconductivity and topological order in the Bi2Se3 thin films," *Science,* vol. 336, pp. 52-55, 2012.

[81] H. Li, T. Zhou, J. He, H.-W. Wang, H. Zhang, H.-C. Liu, *et al.*, "Origin of bias-independent conductance plateaus and zero-bias conductance peaks in Bi 2 Se 3/NbSe 2 hybrid structures," *Physical Review B,* vol. 96, p. 075107, 2017.

[82] D. Zhang, J. Wang, A. M. DaSilva, J. S. Lee, H. R. Gutierrez, M. H. Chan, *et al.*, "Superconducting proximity effect and possible evidence for Pearl vortices in a candidate topological insulator," *Physical Review B,* vol. 84, p. 165120, 2011.

[83] P. Zareapour, A. Hayat, S. Y. F. Zhao, M. Kreshchuk, A. Jain, D. C. Kwok, *et al.*, "Proximity-induced high-temperature superconductivity in the topological insulators Bi 2 Se 3 and Bi 2 Te 3," *Nature communications,* vol. 3, p. 1056, 2012.

[84] E. Wang, H. Ding, A. V. Fedorov, W. Yao, Z. Li, Y.-F. Lv, *et al.*, "Fully gapped topological surface states in Bi 2 Se 3 films induced by a d-wave high-temperature superconductor," *Nature physics,* vol. 9, p. 621, 2013.

[85] J. Klein, "Epitaktische Heterostrukturen aus dotierten Manganaten," Universität zu Köln, 2001.

[86] A. C. Ichimiya, Philip I., *Reflection High-Energy Electron Diffraction*. Cambridge, UK: Cambridge University Press, 2004.

[87] J. Zhang, C.-Z. Chang, Z. Zhang, J. Wen, X. Feng, K. Li, *et al.*, "Band structure engineering in (Bi 1− x Sb x) 2 Te 3 ternary topological insulators," *Nature communications,* vol. 2, p. 574, 2011.
[88] B. Y. Yavorsky, N. Hinsche, I. Mertig, and P. Zahn, "Electronic structure and transport anisotropy of Bi 2 Te 3 and Sb 2 Te 3," *Physical Review B,* vol. 84, p. 165208, 2011.
[89] D. Kong, Y. Chen, J. J. Cha, Q. Zhang, J. G. Analytis, K. Lai, *et al.*, "Ambipolar field effect in the ternary topological insulator (Bi(x)Sb(1-x))2Te3 by composition tuning," *Nat Nanotechnol,* vol. 6, pp. 705-9, Oct 2 2011.
[90] X. He, T. Guan, X. Wang, B. Feng, P. Cheng, L. Chen, *et al.*, "Highly tunable electron transport in epitaxial topological insulator (Bi1-xSbx)2Te3 thin films," *Applied Physics Letters,* vol. 101, p. 123111, 2012.
[91] H. Peng, K. Lai, D. Kong, S. Meister, Y. Chen, X.-L. Qi, *et al.*, "Aharonov–Bohm interference in topological insulator nanoribbons," *Nature materials,* vol. 9, p. 225, 2010.
[92] Z. Wang, L. Yang, X. Li, X. Zhao, H. Wang, Z. Zhang, *et al.*, "Granularity controlled nonsaturating linear magnetoresistance in topological insulator Bi2Te3 films," *Nano letters,* vol. 14, pp. 6510-6514, 2014.
[93] J. G. Checkelsky, Y. S. Hor, R. J. Cava, and N. P. Ong, "Bulk Band Gap and Surface State Conduction Observed in Voltage-Tuned Crystals of the Topological Insulator ${\mathrm{Bi}}_{2}{\mathrm{Se}}_{3}$," *Physical Review Letters,* vol. 106, p. 196801, 05/10/ 2011.
[94] F. Xiu, L. He, Y. Wang, L. Cheng, L.-T. Chang, M. Lang, *et al.*, "Manipulating surface states in topological insulator nanoribbons," *Nature Nanotechnology,* vol. 6, p. 216, 02/13/online 2011.
[95] Y. Wang, F. Xiu, L. Cheng, L. He, M. Lang, J. Tang, *et al.*, "Gate-controlled surface conduction in Na-doped Bi2Te3 topological insulator nanoplates," *Nano letters,* vol. 12, pp. 1170-1175, 2012.
[96] X. Chen, X. C. Ma, K. He, J. F. Jia, and Q. K. Xue, "Molecular beam epitaxial growth of topological insulators," *Advanced Materials,* vol. 23, pp. 1162-1165, 2011.
[97] A. Taskin, S. Sasaki, K. Segawa, and Y. Ando, "Manifestation of topological protection in transport properties of epitaxial Bi 2 Se 3 thin films," *Physical review letters,* vol. 109, p. 066803, 2012.
[98] A. Taskin, S. Sasaki, K. Segawa, and Y. Ando, "Achieving surface quantum oscillations in topological insulator thin films of Bi2Se3," *Advanced Materials,* vol. 24, pp. 5581-5585, 2012.
[99] L. He, X. Kou, and K. L. Wang, "Review of 3D topological insulator thin-film growth by molecular beam epitaxy and potential applications," *physica status solidi (RRL) – Rapid Research Letters,* vol. 7, pp. 50-63, 2013.
[100] Y. Y. Li, G. Wang, X. G. Zhu, M. H. Liu, C. Ye, X. Chen, *et al.*, "Intrinsic topological insulator Bi2Te3 thin films on Si and their thickness limit," *Adv Mater,* vol. 22, pp. 4002-7, Sep 22 2010.
[101] Y. S. Kim, M. Brahlek, N. Bansal, E. Edrey, G. A. Kapilevich, K. Iida, *et al.*, "Thickness-dependent bulk properties and weak antilocalization effect in topological insulator Bi 2 Se 3," *Physical Review B,* vol. 84, p. 073109, 2011.
[102] L. He, F. Xiu, X. Yu, M. Teague, W. Jiang, Y. Fan, *et al.*, "Surface-dominated conduction in a 6 nm thick Bi2Se3 thin film," *Nano letters,* vol. 12, pp. 1486-1490, 2012.

[103] G. Zhang, H. Qin, J. Teng, J. Guo, Q. Guo, X. Dai, *et al.*, "Quintuple-layer epitaxy of thin films of topological insulator Bi 2 Se 3," *Applied Physics Letters,* vol. 95, p. 053114, 2009.
[104] T. Hirahara, Y. Sakamoto, Y. Takeichi, H. Miyazaki, S.-i. Kimura, I. Matsuda, *et al.*, "Anomalous transport in an n-type topological insulator ultrathin Bi 2 Se 3 film," *Physical Review B,* vol. 82, p. 155309, 2010.
[105] L. He, F. Xiu, Y. Wang, A. V. Fedorov, G. Huang, X. Kou, *et al.*, "Epitaxial growth of Bi2Se3 topological insulator thin films on Si (111)," *Journal of Applied Physics,* vol. 109, p. 103702, 2011.
[106] X. Kou, L. He, F. Xiu, M. Lang, Z. Liao, Y. Wang, *et al.*, "Epitaxial growth of high mobility Bi 2 Se 3 thin films on CdS," *Applied Physics Letters,* vol. 98, p. 242102, 2011.
[107] X. Yu, L. He, M. Lang, W. Jiang, F. Xiu, Z. Liao, *et al.*, "Separation of top and bottom surface conduction in Bi2Te3 thin films," *Nanotechnology,* vol. 24, p. 015705, 2012.
[108] Z. Wang, H. Li, X. Guo, W. Ho, and M. Xie, "Growth characteristics of topological insulator Bi2Se3 films on different substrates," *Journal of Crystal Growth,* vol. 334, pp. 96-102, 2011.
[109] T. Talebi, R. Ghomashchi, P. Talemi, and S. Aminorroaya Yamini, "Preparation of n-type Bi2Te3 films by electrophoretic deposition," *International Journal of Chemical, Molecular, Nuclear, Materials and Metallurgical Engineering,* vol. 11, 2017.
[110] S. Cheng, P. Cebe, L. M. Hanssen, D. M. Riffe, and A. Sievers, "Hemispherical emissivity of V, Nb, Ta, Mo, and W from 300 to 1000 K," *JOSA B,* vol. 4, pp. 351-356, 1987.
[111] H. Zhang, X. Ma, L. Li, D. Langenberg, C. G. Zeng, and G. X. Miao, "Two-step growth of high-quality Nb/(Bi 0.5 Sb 0.5) 2 Te 3/Nb heterostructures for topological Josephson junctions," *Journal of Materials Research,* vol. 33, pp. 2423-2433, 2018.
[112] C.-Z. Chang, W. Zhao, J. Li, J. K. Jain, C. Liu, J. S. Moodera, *et al.*, "Observation of the Quantum Anomalous Hall Insulator to Anderson Insulator Quantum Phase Transition and its Scaling Behavior," *Physical Review Letters,* vol. 117, p. 126802, 09/14/ 2016.
[113] J. Moodera, X. Hao, G. Gibson, and R. Meservey, "Electron-spin polarization in tunnel junctions in zero applied field with ferromagnetic EuS barriers," *Physical review letters,* vol. 61, p. 637, 1988.
[114] A. Mauger and C. Godart, "The magnetic, optical, and transport properties of representatives of a class of magnetic semiconductors: The europium chalcogenides," *Physics Reports,* vol. 141, pp. 51-176, 1986.
[115] J. S. Moodera, X. Hao, G. A. Gibson, and R. Meservey, "Electron-Spin Polarization in Tunnel Junctions in Zero Applied Field with Ferromagnetic EuS Barriers," *Physical Review Letters,* vol. 61, pp. 637-640, 08/01/ 1988.
[116] T. Nagahama, T. S. Santos, and J. S. Moodera, "Enhanced Magnetotransport at High Bias in Quasimagnetic Tunnel Junctions with EuS Spin-Filter Barriers," *Physical Review Letters,* vol. 99, p. 016602, 07/06/ 2007.
[117] G.-X. Miao and J. S. Moodera, "Controlling magnetic switching properties of EuS for constructing double spin filter magnetic tunnel junctions," *Applied Physics Letters,* vol. 94, p. 182504, 2009.
[118] P. Wei, F. Katmis, B. A. Assaf, H. Steinberg, P. Jarillo-Herrero, D. Heiman, *et al.*, "Exchange-coupling-induced symmetry breaking in topological insulators," *Physical review letters,* vol. 110, p. 186807, 2013.

[119] M. Li, W. Cui, J. Yu, Z. Dai, Z. Wang, F. Katmis, *et al.*, "Magnetic proximity effect and interlayer exchange coupling of ferromagnetic/topological insulator/ferromagnetic trilayer," *Physical Review B,* vol. 91, p. 014427, 2015.
[120] C. Lee, F. Katmis, P. Jarillo-Herrero, J. S. Moodera, and N. Gedik, "Direct measurement of proximity-induced magnetism at the interface between a topological insulator and a ferromagnet," *Nature Communications,* vol. 7, p. 12014, 06/27/online 2016.
[121] F. Katmis, V. Lauter, F. S. Nogueira, B. A. Assaf, M. E. Jamer, P. Wei, *et al.*, "A high-temperature ferromagnetic topological insulating phase by proximity coupling," *Nature,* vol. 533, p. 513, 05/09/online 2016.
[122] C. L. Richardson, J. M. Devine-Stoneman, G. Divitini, M. E. Vickers, C. Z. Chang, M. Amado, *et al.*, "Structural properties of thin-film ferromagnetic topological insulators," *Scientific Reports,* vol. 7, p. 12061, 2017/09/21 2017.
[123] M. Li, Q. Song, W. Zhao, J. A. Garlow, T.-H. Liu, L. Wu, *et al.*, "Dirac-electron-mediated magnetic proximity effect in topological insulator/magnetic insulator heterostructures," *Physical Review B,* vol. 96, p. 201301, 11/01/ 2017.
[124] C. Tang, C.-Z. Chang, G. Zhao, Y. Liu, Z. Jiang, C.-X. Liu, *et al.*, "Above 400-K robust perpendicular ferromagnetic phase in a topological insulator," *Science Advances,* vol. 3, p. e1700307, 2017.
[125] J. Williams, A. Bestwick, P. Gallagher, S. S. Hong, Y. Cui, A. S. Bleich, *et al.*, "Unconventional Josephson effect in hybrid superconductor-topological insulator devices," *Physical review letters,* vol. 109, p. 056803, 2012.
[126] M. Snelder, M. Veldhorst, A. A. Golubov, and A. Brinkman, "Andreev bound states and current-phase relations in three-dimensional topological insulators," *Physical Review B,* vol. 87, p. 104507, 2013.
[127] G. Blonder, M. Tinkham, and T. Klapwijk, "Transition from metallic to tunneling regimes in superconducting microconstrictions: Excess current, charge imbalance, and supercurrent conversion," *Physical Review B,* vol. 25, p. 4515, 1982.
[128] A. Furusaki, "Josephson current carried by Andreev levels in superconducting quantum point contacts," *Superlattices and microstructures,* vol. 25, pp. 809-818, 1999.
[129] J. Nilsson, A. Akhmerov, and C. Beenakker, "Splitting of a Cooper pair by a pair of Majorana bound states," *Physical review letters,* vol. 101, p. 120403, 2008.
[130] L. Fu and C. L. Kane, "Josephson current and noise at a superconductor/quantum-spin-Hall-insulator/superconductor junction," *Physical Review B,* vol. 79, p. 161408, 2009.
[131] L. Fu and C. L. Kane, "Probing neutral Majorana fermion edge modes with charge transport," *Physical review letters,* vol. 102, p. 216403, 2009.
[132] B. Sacépé, J. B. Oostinga, J. Li, A. Ubaldini, N. J. G. Couto, E. Giannini, *et al.*, "Gate-tuned normal and superconducting transport at the surface of a topological insulator," *Nature Communications,* vol. 2, p. 575, 12/06/online 2011.
[133] H.-S. Chang, M.-H. Bae, and H.-J. Lee, "McMillan–Rowell oscillations observed in c-axis Au/Bi2Sr2CaCu2O8+ δ junctions," *Physica C: Superconductivity,* vol. 408, pp. 618-619, 2004.
[134] O. Shvetsov, V. Kostarev, A. Kononov, V. Golyashov, K. Kokh, O. Tereshchenko, *et al.*, "Conductance oscillations and zero-bias anomaly in a single superconducting junction to a three-dimensional Bi2Te3 topological insulator," *EPL,* vol. 119, p. 57009, 2017.

[135] F. Qu, F. Yang, J. Shen, Y. Ding, J. Chen, Z. Ji, *et al.*, "Strong superconducting proximity effect in Pb-Bi 2 Te 3 hybrid structures," *Scientific reports,* vol. 2, p. 339, 2012.
[136] E. P. Harris and D. Mapother, "Critical field of superconducting aluminum as a function of pressure and temperature above 0.3 K," *Physical Review,* vol. 165, p. 522, 1968.
[137] M. P. Stehno, N. W. Hendrickx, M. Snelder, T. Scholten, Y. Huang, M. S. Golden, *et al.*, "Conduction spectroscopy of a proximity induced superconducting topological insulator," *Semiconductor science and technology,* vol. 32, p. 094001, 2017.
[138] W. N. Kang, H.-J. Kim, E.-M. Choi, C. U. Jung, and S.-I. Lee, "MgB₂ Superconducting Thin Films with a Transition Temperature of 39 Kelvin," *Science,* vol. 292, p. 1521, 2001.
[139] A. Y. Liu, I. Mazin, and J. Kortus, "Beyond Eliashberg superconductivity in MgB 2: anharmonicity, two-phonon scattering, and multiple gaps," *Physical Review Letters,* vol. 87, p. 087005, 2001.
[140] P. Szabó, P. Samuely, J. Kačmarčík, T. Klein, J. Marcus, D. Fruchart, *et al.*, "Evidence for two superconducting energy gaps in MgB 2 by point-contact spectroscopy," *Physical Review Letters,* vol. 87, p. 137005, 2001.
[141] S. Tsuda, T. Yokoya, T. Kiss, Y. Takano, K. Togano, H. Kito, *et al.*, "Evidence for a multiple superconducting gap in MgB 2 from high-resolution photoemission spectroscopy," *Physical review letters,* vol. 87, p. 177006, 2001.
[142] Y. Bugoslavsky, Y. Miyoshi, G. Perkins, A. Berenov, Z. Lockman, J. MacManus-Driscoll, *et al.*, "Structure of the superconducting gap in MgB2 from point-contact spectroscopy," *Superconductor Science and Technology,* vol. 15, p. 526, 2002.
[143] T. Heitmann, S. Bu, D. Kim, J. Choi, J. Giencke, C. Eom, *et al.*, "MgB2 energy gap determination by scanning tunnelling spectroscopy," *Superconductor Science and Technology,* vol. 17, p. 237, 2003.
[144] S. Souma, Y. Machida, T. Sato, T. Takahashi, H. Matsui, S.-C. Wang, *et al.*, "The origin of multiple superconducting gaps in MgB 2," *Nature,* vol. 423, p. 65, 2003.
[145] F. Bouquet, R. Fisher, N. Phillips, D. Hinks, and J. Jorgensen, "Specific heat of Mg 11 B 2: evidence for a second energy gap," *Physical review letters,* vol. 87, p. 047001, 2001.
[146] G. Rubio-Bollinger, H. Suderow, and S. Vieira, "Tunneling Spectroscopy in Small Grains of Superconducting ${\mathrm{MgB}}_{2}$," *Physical Review Letters,* vol. 86, pp. 5582-5584, 06/11/ 2001.
[147] H. J. Choi, D. Roundy, H. Sun, M. L. Cohen, and S. G. Louie, "The origin of the anomalous superconducting properties of MgB 2," *Nature,* vol. 418, p. 758, 2002.
[148] F. Giubileo, D. Roditchev, W. Sacks, R. Lamy, D. Thanh, J. Klein, *et al.*, "Two-gap state density in MgB 2: a true bulk property or a proximity effect?," *Physical review letters,* vol. 87, p. 177008, 2001.
[149] M. Iavarone, G. Karapetrov, A. E. Koshelev, W. K. Kwok, G. W. Crabtree, D. G. Hinks, *et al.*, "Two-Band Superconductivity in ${\mathrm{M}\mathrm{g}\mathrm{B}}_{2}$," *Physical Review Letters,* vol. 89, p. 187002, 10/11/ 2002.
[150] K. Ueda, S. Saito, K. Semba, T. Makimoto, and M. Naito, "All-MgB_2 Josephson tunnel junctions," *Applied Physics Letters,* vol. 86, p. 172502, 2005.
[151] M. V. Costache and J. S. Moodera, "All magnesium diboride Josephson junctions with MgO and native oxide barriers," *Applied Physics Letters,* vol. 96, p. 082508, 2010.

[152] T. Melbourne, D. Cunnane, E. Galan, X. Xi, and K. Chen, "Study of MgB_2 Josephson Junction Arrays and Sub- um Junctions," *IEEE Transactions on Applied Superconductivity,* vol. 25, 2015 2015.
[153] A. Brinkman, D. Veldhuis, D. Mijatovic, G. Rijnders, D. H. A. Blank, H. Hilgenkamp*, et al.*, "Superconducting quantum interference device based on MgB_2 nanobridges," *Applied Physics Letters,* vol. 79, p. 2420, 2001.
[154] C. B. Eom, M. K. Lee, J. H. Choi, L. J. Belenky, X. Song, L. D. Cooley*, et al.*, "High critical current density and enhanced irreversibility field in superconducting MgB_2 thin films," *Nature,* vol. 411, pp. 558-560, 05/31/print 2001.
[155] X. Zeng, A. V. Pogrebnyakov, A. Kotcharov, J. E. Jones, X. X. Xi, E. M. Lysczek*, et al.*, "In situ epitaxial MgB_2 thin films for superconducting electronics," *Nat Mater,* vol. 1, pp. 35-38, 09//print 2002.
[156] S.-D. Bu, D. M. Kim, J. Choi, J. Giencke, S. Patnaik, L. Cooley*, et al.*, "Synthesis and properties of c-axis oriented epitaxial MgB_2 thin films," *arXiv preprint cond-mat/0204004,* 2002.
[157] W. N. Kang, H.-J. Kim, E.-M. Choi, C. U. Jung, and S.-I. Lee, "MgB_2 Superconducting Thin Films with a Transition Temperature of 39 Kelvin," *Science,* vol. 292, pp. 1521-1523, 2001-05-25 00:00:00 2001.
[158] A. Van Erven, T. Kim, M. Muenzenberg, and J. Moodera, "Highly crystallized as-grown smooth and superconducting MgB_2 films by molecular-beam epitaxy," *Applied physics letters,* vol. 81, pp. 4982-4984, 2002.
[159] W. Jo, J.-U. Huh, T. Ohnishi, A. F. Marshall, M. R. Beasley, and R. H. Hammond, "In situ growth of superconducting MgB_2 thin films with preferential orientation by molecular-beam epitaxy," *Applied Physics Letters,* vol. 80, pp. 3563-3565, 2002.
[160] J.-B. Laloë, T. Kim, and J. S. Moodera, "Molecular-Beam Epitaxially Grown MgB_2 Thin Films and Superconducting Tunnel Junctions," *Advances in Condensed Matter Physics,* vol. 2011, pp. 1-9, 2011.
[161] K. Ueda and M. Naito, "As-grown superconducting MgB_2 thin films prepared by molecular beam epitaxy," *Applied Physics Letters,* vol. 79, pp. 2046-2048, 2001.
[162] K. Ueda and M. Naito, "In situ growth of superconducting MgB_2 thin films by molecular-beam epitaxy," *Journal of Applied Physics,* vol. 93, p. 2113, 2003.
[163] S. Hiroaki, Y. Takuya, and I. Takekazu, "Ambient temperature epitaxial growth of MgB_2 thin films with a Mg buffer layer," *Applied Physics Express,* vol. 8, p. 113101, 2015.
[164] J.-J. Chang, "Fiske steps in Josephson junctions," *Physical Review B,* vol. 28, pp. 1276-1280, 08/01/ 1983.
[165] S. M. Kim, H. B. Wang, T. Hatano, S. Urayama, S. Kawakami, M. Nagao*, et al.*, "Fiske steps studied by flux-flow resistance oscillation in a narrow stack of $Bi_2Sr_2CaCu_2O_{8+d}$ junctions," *Physical Review B,* vol. 72, p. 140504, 10/26/ 2005.
[166] V. M. Krasnov, N. Mros, A. Yurgens, and D. Winkler, "Fiske steps in intrinsic $Bi_2Sr_2CaCu_2O_{8+x}$ stacked Josephson junctions," *Physical Review B,* vol. 59, pp. 8463-8466, 04/01/ 1999.
[167] A. Barone and G. Paternò, "Resonant Modes in Tunneling Structures," in *Physics and Applications of the Josephson Effect*, ed: Wiley-VCH Verlag GmbH & Co. KGaA, 2005, pp. 235-263.

[168] X. Zeng, A. V. Pogrebnyakov, A. Kotcharov, J. E. Jones, X. Xi, E. M. Lysczek*, et al.*, "In situ epitaxial MgB 2 thin films for superconducting electronics," *Nature materials,* vol. 1, p. 35, 2002.

[169] S. D. Bu, D. M. Kim, J. H. Choi, J. Giencke, E. E. Hellstrom, D. C. Larbalestier*, et al.*, "Synthesis and properties of c-axis oriented epitaxial MgB2 thin films," *Applied Physics Letters,* vol. 81, pp. 1851-1853, 2002/09/02 2002.

[170] A. J. M. van Erven, T. H. Kim, M. Muenzenberg, and J. S. Moodera, "Highly crystallized as-grown smooth and superconducting MgB2 films by molecular-beam epitaxy," *Applied Physics Letters,* vol. 81, pp. 4982-4984, 2002/12/23 2002.

[171] T. H. Kim and J. S. Moodera, "Magnesium diboride superconductor thin film tunnel junctions for superconductive electronics," *Journal of Applied Physics,* vol. 100, p. 113904, 2006/12/01 2006.

[172] Lalo, #235, J.-B. , T. H. Kim, and J. S. Moodera, "Molecular-Beam Epitaxially Grown MgB2 Thin Films and Superconducting Tunnel Junctions," *Advances in Condensed Matter Physics,* vol. 2011, 2011.

[173] K. Ueda and M. Naito, "In situ growth of superconducting MgB2 thin films by molecular-beam epitaxy," *Journal of Applied Physics,* vol. 93, pp. 2113-2120, 2003.

[174] W. P. Gilbreath, "The vapor pressure of magnesium between 223 and 385 C," Ames Research Center, National Aeronautics and Space Administration, Moffett …1965.

[175] S. Yuasa, T. Nagahama, A. Fukushima, Y. Suzuki, and K. Ando, "Giant room-temperature magnetoresistance in single-crystal Fe/MgO/Fe magnetic tunnel junctions," *Nature materials,* vol. 3, p. 868, 2004.

[176] D. D. Djayaprawira, K. Tsunekawa, M. Nagai, H. Maehara, S. Yamagata, N. Watanabe*, et al.*, "230% room-temperature magnetoresistance in CoFeB ／ MgO ／ CoFeB magnetic tunnel junctions," *Applied Physics Letters,* vol. 86, p. 092502, 2005.

[177] S. Ikeda, K. Miura, H. Yamamoto, K. Mizunuma, H. Gan, M. Endo*, et al.*, "A perpendicular-anisotropy CoFeB–MgO magnetic tunnel junction," *Nature materials,* vol. 9, p. 721, 2010.

[178] D. Mijatovic, A. Brinkman, I. Oomen, G. Rijnders, H. Hilgenkamp, H. Rogalla*, et al.*, "Magnesium-diboride ramp-type Josephson junctions," *Applied physics letters,* vol. 80, pp. 2141-2143, 2002.

[179] M. Costache and J. Moodera, "All magnesium diboride Josephson junctions with MgO and native oxide barriers," *Applied Physics Letters,* vol. 96, p. 082508, 2010.

[180] B. D. Josephson, "Possible new effects in superconductive tunnelling," *Physics letters,* vol. 1, pp. 251-253, 1962.

[181] W. Buckel and R. Kleiner, "Fundamental properties of superconductors," *Superconductivity: Fundamentals and Applications,* pp. 11-71, 2008.

[182] A. Brinkman, A. A. Golubov, H. Rogalla, O. Dolgov, J. Kortus, Y. Kong*, et al.*, "Multiband model for tunneling in MgB 2 junctions," *Physical Review B,* vol. 65, p. 180517, 2002.

[183] K. Ueda, S. Saito, K. Semba, T. Makimoto, and M. Naito, "All-MgB 2 josephson tunnel junctions," *Applied Physics Letters,* vol. 86, p. 172502, 2005.

[184] T. Melbourne, D. Cunnane, E. Galan, X. X. Xi, and K. Chen, "Study of$\hbox{MgB}_{2}$Josephson Junction Arrays and Sub-$\mu\hbox{m}$Junctions," *IEEE Transactions on Applied Superconductivity,* vol. 25, pp. 1-4, 2015.

[185] D. Cunnane, E. Galan, K. Chen, and X. Xi, "Planar-type MgB2 SQUIDs utilizing a multilayer process," *Applied Physics Letters,* vol. 103, p. 212603, 2013.

[186] A. A. Golubov, A. Brinkman, O. Dolgov, J. Kortus, and O. Jepsen, "Multiband model for penetration depth in MgB 2," *Physical Review B,* vol. 66, p. 054524, 2002.
[187] H. Shim, K. Yoon, J. Moodera, and J. Hong, "All Mg B 2 tunnel junctions with Al 2 O 3 or MgO tunnel barriers," *Applied physics letters,* vol. 90, p. 212509, 2007.
[188] D. Cunnane, C. Zhuang, K. Chen, X. Xi, J. Yong, and T. Lemberger, "Penetration depth of MgB2 measured using Josephson junctions and SQUIDs," *Applied Physics Letters,* vol. 102, p. 072603, 2013.
[189] A. Barone and G. Paterno, *Physics and applications of the Josephson effect*: Wiley, 1982.
[190] "Al2O3 Crystal Structure: Datasheet from "PAULING FILE Multinaries Edition – 2012" in SpringerMaterials (https://materials.springer.com/isp/crystallographic/docs/sd_0541335)," P. Villars and K. Cenzual, Eds., ed: Springer-Verlag Berlin Heidelberg & Material Phases Data System (MPDS), Switzerland & National Institute for Materials Science (NIMS), Japan.
[191] "Si Crystal Structure: Datasheet from "PAULING FILE Multinaries Edition – 2012" in SpringerMaterials (https://materials.springer.com/isp/crystallographic/docs/sd_0530557)," P. Villars and K. Cenzual, Eds., ed: Springer-Verlag Berlin Heidelberg & Material Phases Data System (MPDS), Switzerland & National Institute for Materials Science (NIMS), Japan.
[192] "SrTiO3 Crystal Structure: Datasheet from "PAULING FILE Multinaries Edition – 2012" in SpringerMaterials (https://materials.springer.com/isp/crystallographic/docs/sd_0554610)," P. Villars and K. Cenzual, Eds., ed: Springer-Verlag Berlin Heidelberg & Material Phases Data System (MPDS), Switzerland & National Institute for Materials Science (NIMS), Japan.
[193] "Nb Crystal Structure: Datasheet from "PAULING FILE Multinaries Edition – 2012" in SpringerMaterials (https://materials.springer.com/isp/crystallographic/docs/sd_1215974)," P. Villars and K. Cenzual, Eds., ed: Springer-Verlag Berlin Heidelberg & Material Phases Data System (MPDS), Switzerland & National Institute for Materials Science (NIMS), Japan.
[194] "MgO Crystal Structure: Datasheet from "PAULING FILE Multinaries Edition – 2012" in SpringerMaterials (https://materials.springer.com/isp/crystallographic/docs/sd_0561181)," P. Villars and K. Cenzual, Eds., ed: Springer-Verlag Berlin Heidelberg & Material Phases Data System (MPDS), Switzerland & National Institute for Materials Science (NIMS), Japan.
[195] "EuS Crystal Structure: Datasheet from "PAULING FILE Multinaries Edition – 2012" in SpringerMaterials (https://materials.springer.com/isp/crystallographic/docs/sd_0548070)," P. Villars and K. Cenzual, Eds., ed: Springer-Verlag Berlin Heidelberg & Material Phases Data System (MPDS), Switzerland & National Institute for Materials Science (NIMS), Japan.